

UNIVERSITY OF HAMBURG,
INSTITUTE OF METEOROLOGY

MASTERTHESIS

**Trends in Upper Tropospheric
Humidity:
Expansion of the Subtropical
Dry Zones?**

Miriam Tivig

supervised by
Prof. Dr. S. A. BUEHLER
Dr. V. GRUETZUN

January 31, 2017

Title of the Master Thesis:
Trends in upper tropospheric humidity: expansion of the dry zones?

Abstract

Subtropical dry zones, located in the Hadley Cells' subsidence regions, where Earth's major deserts can be found, strongly influence regional precipitation as well as outgoing longwave radiation. Thus, any change in these dry zones could have significant impact on surface climate as well as on the atmospheric energy budget.

Present master thesis investigates trends in upper tropospheric dry zones, using the radiation variable Upper Tropospheric Humidity (UTH), calculated from climate model data output. Temperature and humidity profiles from a model simulation with gradually increasing CO₂ (1pctCO₂) of the Coupled Model Intercomparison Project phase 5 (CMIP5) and the Max Planck Institute (MPI) has been used, to generate UTH via satellite simulation software and the brightness temperature transformation method.

Analysis of global UTH distribution shows that dry zones form a belt in the subtropical winter hemispheres, while in the summer hemispheres, they concentrate in the eastern ocean basins, where the descent regions of Subtropical Anticyclones are located. In the course of the model experiment, dry zones generally increase in winter and decrease in summer.

Recent studies have found tendencies of increasing dryness at the poleward edges of the subtropical subsidence zones. UTH from MPI model data confirms these trends, as the winter hemispheric dry zones expand poleward by 2° to 3° in the course of the 150 model years. In the summer hemispheres, dry zones corresponding to the subtropical anticyclones descent regions are moistening, especially in the eastern North Pacific. Finally, in the Pacific Ocean basin, UTH increases around the intertropical convergence zone (ITCZ), while the features of Walker circulation show a tendency to shift eastward.

UTH calculated from recent observation data taken from satellite-based microwave measurements (AMSU-B), reveal a poleward shift of the dry zones edge only in the winter hemisphere. The trends found in the subtropical anticyclones dry zones could not be confirmed. In the future, longer observation periods with microwave measurements will be helpful to find more significant trends in upper tropospheric dry zones, where even small changes can have considerable impact on water vapour feedback.

Contents

1	Introduction	11
2	Physical and Meteorological Background	13
2.1	The General Atmospheric Circulation	13
2.2	The Subsidence Regions: Dry Zones in the Upper Troposphere	15
2.3	Water Vapour and UTH	17
2.3.1	Definition of UTH	18
2.3.2	Water Vapour and Climate Sensitivity	18
2.3.3	Measurements of Upper Tropospheric Moisture	21
2.3.4	Simulation of Upper Tropospheric Water Vapour in Global Circulation Models	23
3	Data, Tools and Methods	25
3.1	The Coupled Model Intercomparison Project Phase 5 (CMIP5)	25
3.1.1	The Idealized Experiments of CMIP5	26
3.1.2	Presentation of the CMIP5 Model Selection	27
3.2	Forward Operators COSP and RTTOV	30
3.2.1	The CFMIP Observation Simulator Package (COSP)	30
3.2.2	The Fast Radiative Transfer Model RTTOV	31
3.2.3	Procedure Followed to Run COSP/RTTOV	31
3.3	Satellite Data	33
3.4	The Brightness Temperature Transformation Method	36
3.5	Definition of the Dry Zones	38
4	Current State of Research	39
4.1	The Seasonal Cycle of UTH	39
4.2	Trends from Model Data	40
4.3	Trends in Observations	40
5	Evolution of Dry Zones in the Upper Troposphere	42
5.1	General Distribution of the Dry Zones	42

5.2	Evolution of UTH and the Dry Zones with Progressively Increasing CO ₂ Concentration	44
5.2.1	Global View in MPI-ESM-MR Model and 1pctCO2 Run	44
5.2.2	The Dry Belt in the MPI-ESM-MR 1pctCO2 Run	51
5.2.3	Moistening Trend in the Descent Zones of the Subtropical An- ticyclones	58
5.2.4	The Pacific Dry Zones: the Hadley and Walker Circulations	65
5.3	Evolution of UTH and the Dry Zones in the abrupt4xCO2 Experiment	68
5.4	Comparison with other CMIP5 Models	75
5.5	Comparison with Satellite Observations	79
6	Conclusion	89
	Appendices	94
A	CMIP5 Models	95
B	COSP Namelists	97
B.1	COSP Input Namelist	97
B.2	COSP Output Namelist	100
B.3	COSP cmor Namelist	102
C	First Decade of abrupt4xCO2 and 1pctCO2	104
	Bibliography	105
	Acknowledgements	117
	Eidesstattliche Erklärung	118

List of Figures

2.1	Earth's Annual Radiation Budget	14
2.2	Three-Cell Structure of the Mean Meridional Circulation.	14
2.3	Tropical Circulation	16
2.4	Dependence between Relative Humidity in the Upper Troposphere and OLR	19
3.1	AMSU-B Jacobians	34
3.2	Equator Crossing Time for NOAA	35
3.3	Dry Zones in the Yearly Mean	38
5.1	Overview of UTH in DJF and JJA	43
5.2	UTH in DJF in MPI 1pctCO2 for 15 Decades	45
5.3	UTH in JJA in MPI 1pctCO2 for 15 Decades	46
5.4	Histograms of First and Last Decade	47
5.5	Timeseries and Trend of UTHp30 in NH and SH for DJF and JJA . .	49
5.6	UTH difference in 1pctCO2 between 1850-1859 and 1990-1999	50
5.7	Poleward edge of the Drybelt	52
5.8	Poleward expansion of the Drybelt	53
5.9	Decadal Mean of UTH in the Caribbean	55
5.10	Decadal Means of UTHp30 in the Caribbean	56
5.11	Decadal Means of vertical velocity in the Caribbean	57
5.12	Timeseries of UTH in Subtropical North Atlantic in JJA	59
5.13	Timeseries of UTH in Subtropical South Indian Ocean in DJF	60
5.14	15 decades of UTH in eastern North Pacific summer	60
5.15	Dry Zone in Eastern North Pacific in JJA	61
5.16	Timeseries of Vertical Velocity and UTH in Subtropical Anticyclones in Summer	64
5.17	Decadal Mean of Vertical Velocity and Difference	67
5.18	Correlation between Vertical Velocity and UTH	68
5.19	Temperature in the First 10 years of abrupt4xCO2	69
5.20	Fast Response of UTH to abrupt4xCO2 1850	70
5.21	Seasonal Mean of Fast Response of Vertical Velocity to abrupt4xCO2	72

5.22	Fast Response of UTHp30 to abrupt4xCO2 1850	74
5.23	Timeseries of UTH from 1pctCO2 for Different Models	76
5.24	Decadal Mean of UTH from CNRM for the First and the Last Decade of 1pctCO2	77
5.25	Decadal Mean of UTH from BCC-csm1 for the First and the Last Decade of 1pctCO2	78
5.26	UTH from Microwave Data	79
5.27	Poleward Edge of Drybelt in NOAA15 AMSU-B	81
5.28	Drybelt Shift of the Poleward Edge of Drybelt in NOAA15 AMSU-B	81
5.29	UTH from 1pctCO2 Model Run for 1970-1979 Compared to 1990-1999	83
5.30	Timeseries of UTH from Satellite data NH	84
5.31	Timeseries of UTH from Satellite data SH	84
5.32	Timeseries of Dry Zones from Satellite Data NH	87
5.33	Timeseries of Dry Zones from Satellite Data SH	87
C.1	Fast response of UTH to abrupt4xCO2 1850-1859	104

List of Tables

3.1	Configuration and resolution of the main MPI-ESM models	28
3.2	Variables needed as input for COSP/RTTOV	32
3.3	Channel Characteristics of the AMSU-B Instrument	33
3.4	Transformation Parameters for the calculation of UTH	37
5.1	Poleward shift of the edge of the subtropical dry zones between the first and the last decade of 1pctCO2 model run.	54
5.2	Trends in UTH calculated from satellite based measurements	85
5.3	Trends in dry zones calculated from satellite based measurements . . .	88

Blank page

Blank page

Chapter 1

Introduction

Anthropogenic change of Earth's climate has ceased to be a scientific fantasy, gradually becoming reality in the collective consciousness. The United Nations Secretary General named it to be the defining challenge of our era, with impacts on all sectors relevant for human life ([Ban, 2008](#)). Understanding the repercussions of climate change and how it will impact our way of life is still a major challenge, resulting from the climate system's complexity regarding its responses to the increasing atmospheric greenhouse gases.

In the progressing climate change, certain geographic regions are particularly relevant. They show high sensitivity to even small changes of atmospheric composition and play an important role in regulating the planet's energy budget. Tropical dry zones, situated in the subtropical subsidence regions between the tropics and extratropics, are such regions, housing Earth's most important deserts. Their expansion could have a significant impact on the neighbouring regions' climate; additionally, these regions' very dry atmosphere plays an important role in Earth's energy budget, cooling the planet by emitting such radiation back to space, which is not trapped by water vapour or clouds.

An increase of upper tropospheric moisture in subtropical dry zones could therefore lead to a strong water vapour feedback loop: Water vapour being the principal greenhouse gas in the atmosphere, changes in water vapour concentration due to global warming impact absorption of radiation and thus radiative forcing, creating the so-called water vapour feedback ([Held and Soden, 2000](#)). This process is particularly active in the upper troposphere, where water vapour concentration is very low, but strongly influences radiation through cloud formation and direct radiation absorption. Changes in humidity of the upper troposphere are particularly crucial regarding the outgoing longwave radiation budget.

As the upper troposphere lies broadly six to eight kilometres above ground, local measurements of humidity are difficult and satellite data has only recently made it possible to analyse the atmospheric composition in these heights on a global scale.

Still, many open questions remain, such as the evolution of upper tropospheric humidity (UTH) in a changing climate. And while UTH has been given more attention during the past 15 years, the behaviour of dry zones in the upper troposphere has hardly been examined. Only the dry zones directly related to the Hadley Cell's subsidence zones have been the object of recent studies, as the Hadley circulation has been found to expand poleward and with it the subtropical dry regions in the descending branch.

The present study will focus on the upper tropospheric dry zone's evolution in climate warming and attempt to answer the question, how these highly climate-sensitive regions have reacted or how they will react to increasing greenhouse gases. Will they continue expanding (poleward) or shrink? Are they stationary or moving? Are they intensifying or weakening?

Soden and Bretherton (1996) derived a relation between UTH and outgoing radiation in terms of brightness temperature, which can be measured by satellite channels sensitive to water vapour concentration in layers between 500 and 200 hPa. Unfortunately, timescales of satellite measurements are still too short when compared to climate processes. Numerical models are therefore required for understanding dry zone's reaction to climate changes. However, variables predicted by traditional climate models do not comprise UTH or brightness temperature. By making use of satellite simulation software, it is possible to artificially transform model data into radiation variables, from which UTH can be computed.

Model data from the Coupled Model Intercomparison Project Phase 5 (CMIP5, Taylor et al. (2012)) is transformed into brightness temperature using the CFMIP Observation Simulator Package (COSP, Bodas-Salcedo et al. (2011)) and the Radiative Transfer model RTTOV (Saunders et al., 2010). With algorithms developed by Soden and Bretherton (1996) and further enhanced by Buehler and John (2005), UTH is then calculated from simulated brightness temperature. It is thus possible to study the distribution of humidity in the tropical and subtropical upper troposphere, and especially the evolution of dry zones in the global warming scenarios of the CMIP5 models.

The present thesis thus starts with an overview of relevant physical and meteorological background, focussing on UTH (Chapter 2). In the following Chapter 3, data from models and satellite-based measurements is presented and technical tools (COSP and RTTOV) are discussed in detail, leading to the algorithm for computation of UTH from brightness temperature. Chapter 4 briefly summarises the current state of research regarding dry zones in the upper troposphere and allows the transition to this study's results concerning the evolution of upper tropospheric dry zones (Chapter 5). Results are split into model data (5.1-5.4) and observation data (5.5). A conclusion and an outlook are presented in Chapter 6.

Chapter 2

Physical and Meteorological Background

2.1 The General Atmospheric Circulation

The general atmospheric circulation encompasses all large-scale movements of air, which are driven by the sun's incoming energy and the Earth's rotation (Kraus, 2000). Even though this circulation varies from day to day, climate's large scale structure remains fairly constant. The motor of these movements is the differential heating of the system Earth and Atmosphere. The extraterrestrial radiation balance shows a maximum around the Equator and minimums at the poles (Figure 2.1), implying a compensation movement of heat from the Equator towards the poles (Kraus, 2000).

The circulation system is generally simplified as being constituted of three cells in each hemisphere transporting air masses between Equator and poles (Figure 2.2). They are called the Hadley, Ferrel and Rossby Cells.

The Hadley Cells are located in the Tropics, north and south of the belt in which the convergence of the trade winds takes place, named the Intertropical Convergence Zone (ITCZ) (Wallace and Hobbs, 2006). The Hadley Cells are characterised by rising of warm air and release of latent heat near the ITCZ and sinking of colder, denser air around the latitude of 30° north and south (Kraus, 2000; Wallace and Hobbs, 2006). In between, air masses are transported polewards in the upper troposphere (UT) and equatorwards near the surface, from higher towards lower pressure, by transforming potential energy to kinetic energy of the horizontal flow (Wallace and Hobbs, 2006). Because of the conservation of angular momentum, air masses' spin velocity increases while flowing towards the poles, which yields an eastward deviation. The lower air branch flows back to the Equator and is deviated to the west, resulting in the trade winds (e.g. Von Storch et al., 1999).

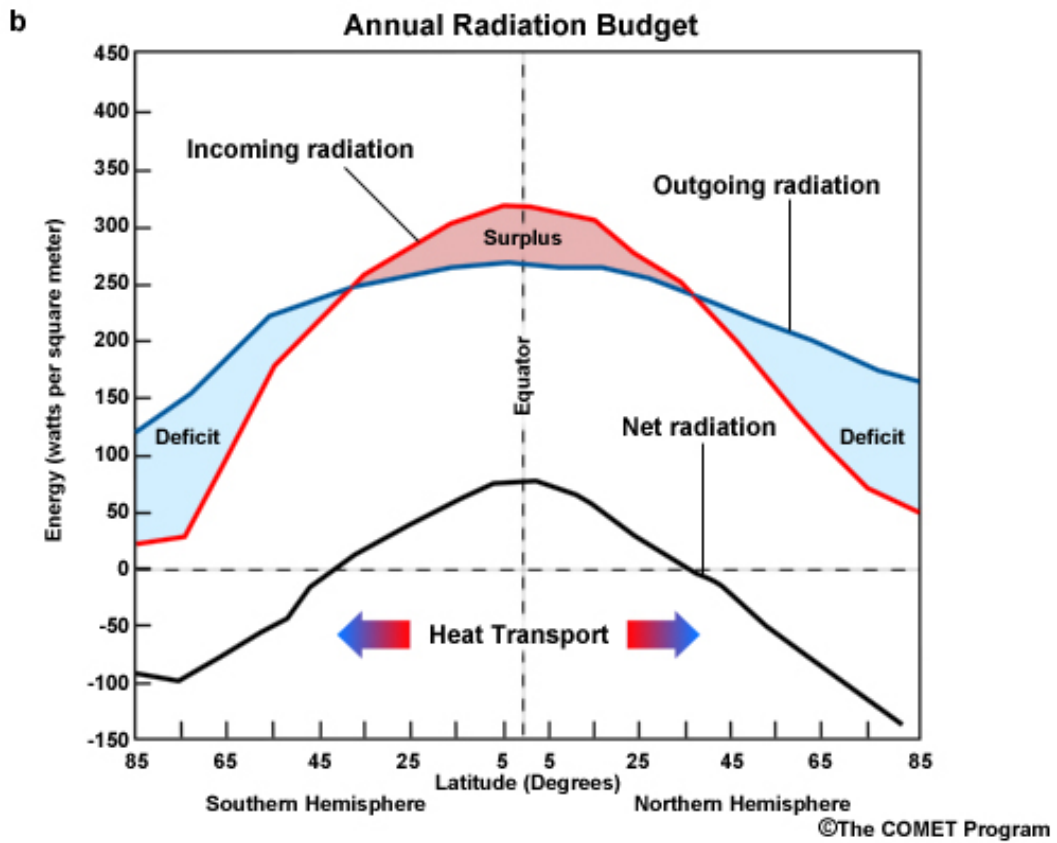


Figure 2.1: Annual Radiation Budget over all latitudes in W/m^2 . (With kind courtesy of [The Comet Program \(2016\)](#), see Copyright Notices.)

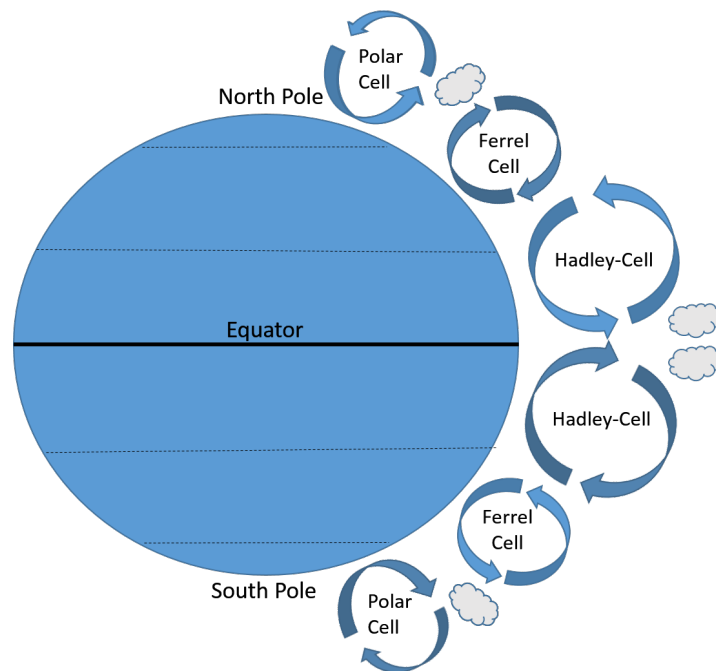


Figure 2.2: Three-Cell Structure of the Mean Meridional Circulation.

The mid-latitudes are controlled by the Ferrel Cells, with ascending air masses in the sub-polar low pressure belt, flowing to the south in the troposphere's upper layers and descending in the subtropics, leading, in the troposphere's lower part, to a compensation flow from the subtropics back to the polar low pressure regions (Malberg, 2007). In contrast to the Hadley Cells, the Ferrel Cells are characterised by rising in cold regions and subsidence in warmer regions, a thermally indirect circulation, sustained by dynamical processes rather than thermal ones (Malberg, 2007; Kraus, 2000).

The weakest circulation structures are the Polar Cells in the highest latitudes, with cold and denser air masses sinking in the sub-polar high pressure zones and warmer air masses rising in the sub-polar low pressure belts (Malberg, 2007).

These three cells in each hemisphere play a major role in the distribution of heat over the Earth and prevent the tropics from becoming too warm and the polar regions from becoming too cold. Therefore, the general circulation is responsible for climate's stability.

It is then not surprising, that the behaviour of the general circulation in climate change is studied thoroughly by climate scientist (e.g. He and Soden, 2015; Hu et al., 2010; Lau and Kim, 2015; Lu et al., 2007). The Hadley circulation is indeed complex and so is its response to global warming. As for now, the results of studies of long term behaviour of the Hadley Cell remain inconclusive (Lu et al., 2007), but a consistent weakening and poleward expansion of the circulation is diagnosed in the AR4 climate change simulations (AR4, IPCC, 2007; Lu et al., 2007; Hu et al., 2010). The present study will be focussed on the Hadley Cell's subsidence zones and their reactions to climate change.

2.2 The Subsidence Regions: Dry Zones in the Upper Troposphere

In the circulation cells' subsidence zones, air masses coming from the Equator are cooling and drying, having lost most of their moisture through precipitation in the cell's upward branch. As these regions have low water vapour content and therefore no clouds in the upper levels, radiative cooling is efficient, leading to subsidence of air masses (Wallace and Hobbs, 2006). As a consequence, convection is suppressed in the subsidence zones and the areas underneath are dry and warm (Wallace and Hobbs, 2006). The most important and large-scale dry zones are located in the subtropics, between the tropics and the extratropics, where the descending branch of the Hadley Cell lies. Learning about the evolution of these zones under global warming is therefore very important concerning the climatological rainfall patterns

in the subtropics (Cai et al., 2012) (Figure 2.3).

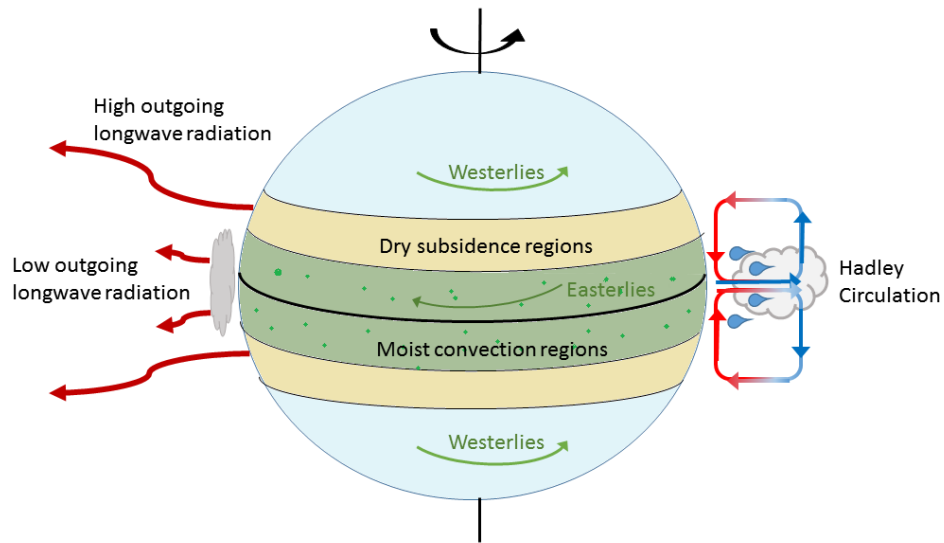


Figure 2.3: Schematic showing the tropical circulation with the moist regions, the dry subsidence zones, the main wind systems and the outgoing longwave radiation structure.

Because the atmosphere’s lower, and therefore warmer parts, have much higher saturation vapour pressure and are closer to the surface water reservoirs, they tend to be relatively saturated (Pierrehumbert et al., 2007). But above the boundary layer, and especially in the upper troposphere, the air is often unsaturated.

The dependence between outgoing radiation and water vapour concentration is approximately logarithmic. Therefore, sensitivity of outgoing long-wave radiation to upper tropospheric relative humidity change is higher at very low than at high humidity (Spencer and Braswell, 1996) and the small amounts of water vapour in the upper troposphere can thus have a significant influence on the radiation budget (Pierrehumbert et al., 2007). This applies all the more to the dry regions within the upper troposphere, which have become of major interest when studying the evolution of climate under global warming.

As it is difficult to measure the humidity in the upper troposphere directly, different methods have been used to analyse dry regions, e.g. by using surface parameters. Lu et al. (2007) identified the edge of the subtropical dry zone in each hemisphere as “the latitude where the zonal mean precipitation minus evaporation (P-E) field crosses zero poleward of the subtropical minimum”. The difference between precipitation and evaporation is at its maximum in the raising branch of the Hadley Cell near the Equator. In the subtropics, where subsidence dominates, the difference is

negative and becomes positive again in the mid-latitudes (Johanson and Fu, 2009). Using this definition, Lu et al. (2007) studied simulated data from models of AR4 (IPCC, 2007) and found that the subtropical dry zones showed a general tendency for poleward expansion under global warming. Observations and model simulations show that the the subtropical dry zone expanded by 1° to 2.5° poleward over the period 1979-2005 (Cai et al., 2012; Johanson and Fu, 2009).

Lau and Kim (2015) define the dry zones as the regions where relative humidity is smaller than 40 % for 500 hPa and smaller than 50 % for 850 hPa. In their study of 33 Coupled Model Intercomparison Project Phase 5 (CMIP5) experiments with prescribed 1 % per year CO_2 emission increase they found a widening of the subtropical subsidence zone, which increases the relative humidity deficit in the tropical upper troposphere. In addition and similar to the study of Lu et al. (2007), strong signals of reduced relative humidity are found at the poleward flank of the climatological subtropical dry zones.

The common patterns that have emerged from studying the dry zones' evolution in the upper troposphere under global warming in climate models are hence a poleward shift of the subtropical dry regions (e.g. Cai et al., 2012) and an increase in the dry regions' width (Lau and Kim, 2015; Sherwood et al., 2010) together with a slight increase in the frequency of occurrence of dry air (Roca et al., 2011).

Considering the observations, one method to study the dry zones' evolution in the upper troposphere makes use of the concept of upper tropospheric humidity (UTH, for exact definition see 2.3.1) also named free tropospheric humidity (FTH). By the mean of UTH, it is possible to study dry zones with satellite based observations. The following Section will therefore give information about the concept of UTH, UTH's importance for the climate and measuring techniques.

2.3 Water Vapour and UTH

Water vapour is a fundamental component of the Earth's radiative budget and widely recognized as being a key climate variable (e.g. Held and Soden, 2000). While in the lower atmosphere it is generally known that water vapour plays a dominant role in weather, its role in the upper troposphere is much more controversial. In the troposphere, water vapour concentration decreases rapidly with height, being limited by saturation humidity, which strongly decreases with temperature, following the Clausius Clapeyron formula (e.g. Peixoto and Oort, 1992). In the following Sections, UTH will be defined and its role in climate sensitivity depicted, followed by an overview of existing measuring methods.

2.3.1 Definition of UTH

The upper troposphere is the region lying between the lower troposphere and the tropopause, roughly between the 500 hPa and the 200 hPa layer (Soden and Lanzante, 1996). There is no well-established precise definition of the upper troposphere (Van Malderen and De Backer, 2010) and there are numerous parameters describing humidity. One of them is UTH, but even for this concept there is more than one definition. Generally, UTH can be defined as a measure for humidity vertically averaged over a broad layer of the upper troposphere. Pierrehumbert et al. (2007) defines the concept of UTH as “the water content of the portion of the atmosphere where water vapour has a considerable effect on the radiation budget”. This wording emphasizes already UTH’s importance for the climate (Section 2.3.2).

UTH can be calculated with regard to relative humidity with respect to water (or ice) (e.g. Brogniez et al., 2015; Gierens and Eleftheratos, 2015) or specific humidity (e.g. Van Malderen and De Backer, 2010). The calculation of UTH used in the present study will be presented in Section 3.4. In the following, the abbreviation UTH will be used only for this radiation variable.

In upper troposphere, the humidity distribution is regulated by other factors than in the boundary layer. The detrainment of vapour and condensed water from convective systems as well as from the global circulation plays a major role in the upper troposphere (IPCC, 2007). As the troposphere’s humid parts are subject of many actual studies, present work will focus on the drier zones within the upper troposphere, which, as mentioned before, are crucial concerning tropical cooling through long-wave radiation. Changes in these areas could therefore have significant impact on the water vapour feedback strength (e.g. Pierrehumbert, 1995; Lindzen et al., 2001; IPCC, 2007; Roca et al., 2011).

Although the role of moisture in the upper troposphere seems to be so important, it is still not fully understood. The latest IPCC Report (IPCC, 2013) tries to explain this lack of knowledge with the large natural variability of the upper tropospheric water vapour and the still short observation records (Section 2.3.3).

2.3.2 Water Vapour and Climate Sensitivity

Upper-tropospheric water vapour concentration is small in comparison with the concentration in the lower troposphere. But because the radiative effect of absorption by water vapour is approximately proportional to the logarithm of its concentration, small additional quantities of water vapour in the upper troposphere suffice to have a strong impact on the radiative budget (Pierrehumbert et al., 2007; Held and Soden, 2000; Spencer and Braswell, 1996) (Figure 2.4). It is the fractional change in

water vapour concentration and not the absolute change that governs its strength as a feedback mechanism (IPCC, 2007) and thus UTH contributes disproportionately to the greenhouse effect.

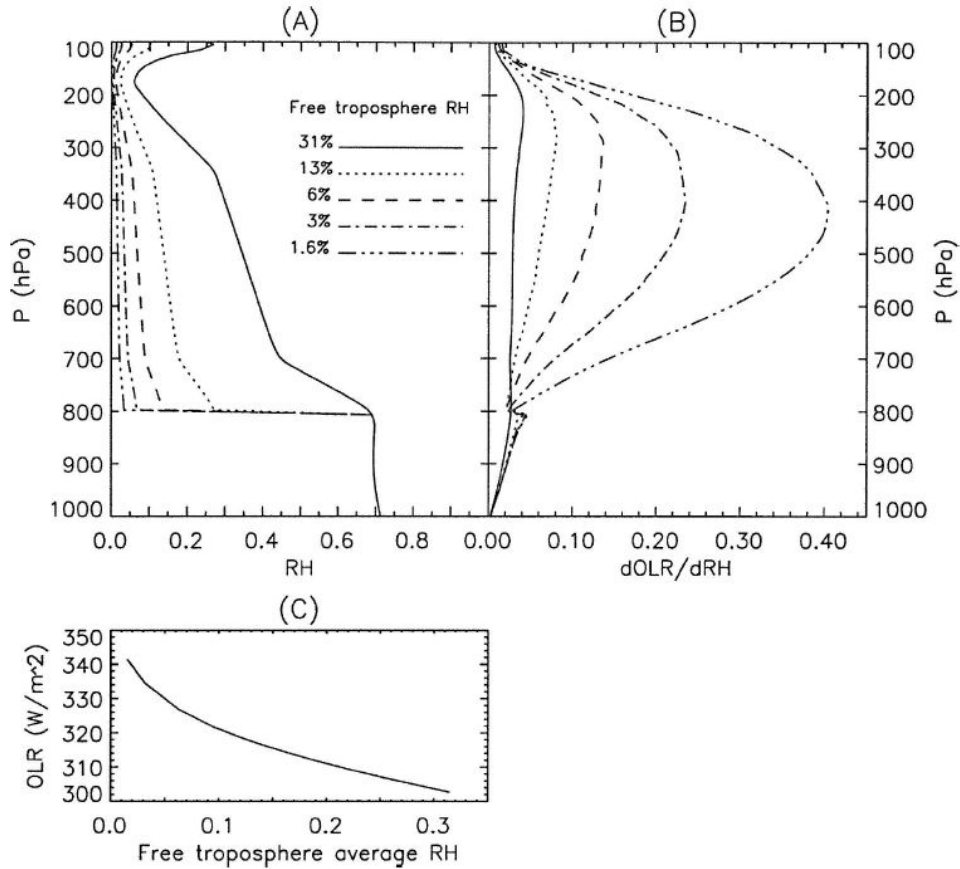


Figure 2.4: (a) Progressive humidity profiles computed by reducing the free-tropospheric specific humidity of the Air Force Geophysical Laboratory profile between 800 and 100 hPa by multiplicative factor of 1.0, 0.4, 0.2, 0.1 and 0.05. This results in height-weighted average relative humidities in the free troposphere of 31 %, 13 %, 6 %, 3 % and 1.6 %, respectively. (b) Sensitivity of outgoing long-wave radiation to additive changes of relative humidity of 3 % in 10-hPa-thick layers as a function of the humidity profiles shown in (a). (c) The non-linear dependence of clear-sky outgoing long-wave radiation over this range of free-tropospheric relative humidity (from Spencer and Braswell, 1996). ©American Meteorological Society. Used with permission (see Copyright Notices).

Due to the strong absorption capacity of water vapour across much of the long-wave spectrum and the quasi exponential increase in the equilibrium water-vapour-pressure with rising temperature (cf. Clausius Clapeyron relationship (Peixoto and Oort, 1992)), scientists have soon predicted a strong positive water vapour feedback in warming climate, assuming that relative humidity would stay approximately constant (e.g. Manabe and Wetherald, 1967, cited after Bony et al., 2006). Möller (1963) first suggested, that the increase of water vapour amount in the atmosphere

following the increasing temperature given a constant relative humidity, could cause a self-amplification effect and create a positive feedback loop ([Gierens and Eleftheratos, 2015](#)).

[Manabe and Wetherald \(1967\)](#) assumed that relative humidity was constant in their radiation-convection model and found that CO₂-doubling led to a higher surface temperature increase, than in the model with fixed absolute humidity ([Manabe and Strickler, 1964](#), cited by [Gierens and Eleftheratos \(2015\)](#)).

But while today it is widely recognized, that water vapour provides a positive climate feedback in the lower troposphere, its role in the upper troposphere is more uncertain. This is due to the fact, that the moisture distribution in the upper troposphere is not alone governed by thermodynamics but also by dynamics.

The question of the role of water vapour in the upper troposphere in a changing climate, or in other words, if water vapour feedback in the upper troposphere can be considered as a positive or a negative feedback, encompasses two aspects: first, what is the effect of water vapour in the UT? Second, how will upper tropospheric water vapour change with global warming?

The first part of this question was answered more or less consistently by several studies. Just as water vapour in general contributes to about 2/3 of the natural greenhouse effect, upper tropospheric water also influences surface radiative forcing. Radiative transfer model estimations show that a 10 % increase in upper tropospheric moisture could contribute nearly 1.4 W/m² of direct radiative forcing ([Udelhofen and Hartmann, 1995](#)). It has been also demonstrated, that the upper tropospheric water vapour contribution to radiative cooling of the atmosphere is disproportionately large ([Held and Soden, 2000](#); [Colman, 2001](#)).

Part of the problem is also the fact, that moisture is controlled through different mechanisms in the tropics and in the extratropics ([Colman, 2001](#)). In particular, the debate persists on the relationship between deep convection and upper tropospheric moisture in a warmer climate and how much a change would contribute to climate feedback in these two regions ([Lindzen, 1990](#); [Soden and Fu, 1995](#); [Sun and Held, 1996](#)).

Through this debate the question of the climate sensitivity contribution of water vapour in the upper troposphere became then more focussed on the question, how the amount of upper tropospheric moisture would change under global warming. This would be the key element for deciding on the character of the upper tropospheric water vapour feedback.

[Lindzen \(1990\)](#) initially claimed, that global warming in relation with water vapour would lead to a negative feedback in the upper troposphere. He argued that, particularly in the tropics, a warmer atmosphere would produce more deep convection and increased subsidence, which would lead to a drying of the upper

troposphere. Convection would short-circuit the greenhouse absorption and hence create a negative feedback.

Later studies disagreed with this hypothesis by showing, that increased convection in fact leads to increased water vapour above 500 hPa (Rind et al., 1991) and that the specific humidity increases at all levels of the atmosphere in response to global warming (Sun and Held, 1996; Minschwaner and Dessler, 2004).

After several studies assumed relative humidity to stay approximately constant under global warming, later research with global circulation models showed an increase in relative humidity in the global upper troposphere above 200 hPa and around the Equator up to 500 hPa, a decrease in the subtropics between 500 and 200 hPa and no significant change of relative humidity elsewhere (e.g. Sherwood et al., 2010; Gierens and Eleftheratos, 2015, and references cited therein).

Finally the question about how exactly UTH will feedback in a changing climate is not fully answered, but depends strongly on the evolution of the amount of water vapour in the upper troposphere (Soden et al., 2005).

Globally climate model simulations predict that the concentration of water vapour in the upper troposphere will increase in the future, which would also be the consequence of a constant relative humidity in a warming climate (Soden et al., 2005). But given the difficulties in accurately simulating clouds and convection, many uncertainties remain and some simulations also predict a decrease in UTH (Minschwaner and Dessler, 2004).

Given , that global warming has already started decades ago, another way to evaluate possible feedback of water vapour in the upper troposphere is the direct measurement of its evolution. As stated before, in situ measurements in UT's high and cold conditions are a technological challenge, but nevertheless, several measuring methods exist and have evolved during the last decades.

2.3.3 Measurements of Upper Tropospheric Moisture

In Situ Measurements

Measuring water vapour at ground level is straightforward and associated observations exist since the 19th century, using multiple variables (e.g. vapour pressure, dew point temperature, relative humidity). Since the 1950s, these measurements have been compiled to feed climate studies (IPCC, 2007). But in the upper troposphere, in situ measurements are more difficult.

The longest humidity measurement records in the troposphere are provided by radiosondes, dating back to the mid-1940s (IPCC, 2007) and delivering comprehen-

sive information about the thermal and humidity structure of the atmosphere (Gettelman et al., 2010). But early sensors suffered from significant biases, especially at higher altitudes, and according to Van Malderen and De Backer (2010), the first humidity sensors seem to have not been sensible enough at lower temperatures, which makes them unusable for measurements in the upper troposphere. That radiosonde humidity measurements tend to have problems under the dry and cold conditions in the upper troposphere, has also been stated by Elliot and Gaffen (1991), who came to the conclusion, that the data was not reliable above 500 hPa. Furthermore, changes in instruments, especially before 1973, lead to discontinuities in the data record (Soden and Lanzante, 1996). A major disadvantage of radiosonde measurement is also the limited spatial coverage, due to the sparse network, particularly over the oceans, making it difficult to draw conclusions on a global scale.

The other method to measure in situ has been used more rarely up to now and consists in observations via aircraft. The data collected by instruments on aircrafts provide mostly high accuracy and precision, as well as high resolution, also for the upper troposphere, but similar to the radiosonde data, it is restricted in time and space (Gettelman et al., 2010). Therefore, it is difficult to have a global view of upper tropospheric water vapour using aircraft measurements. Nevertheless, several campaigns exist since 1995, which provide data covering altitudes up to 22 km in near all latitudes for most of the four seasons (Tilmes et al., 2010; Smit et al., 2014). In particular, the MOZAIC observations (Smit et al., 2014), which include measurements via sensors installed on commercial airplanes, provide more data with every year and will be, in the future, a precious data sampling for further studying the humidity in the upper troposphere. However, current data covers mostly North America and Europe, leaving it of limited value to global analysis (Gettelman et al., 2010).

Satellite Measurements

The molecular line spectrum of the H₂O molecule presents strong spectral lines at wavelengths exceeding 16 μm and at 6.3 μm . These get optically thick in the upper troposphere and the stratosphere, so that satellite-based instruments observing Earth in these wavelengths are not able to look deeper in the atmosphere than into these emitting layers (Gierens and Eleftheratos, 2015). This enables measuring the humidity of this part of the atmosphere using satellite based instruments.

During the last decades, satellite-based instruments have become more and more reliable. Contrary to the in situ measurements, satellite data has global coverage. However, the observations are available only since 1979 for infrared sounders and only since 1994 for microwave sounders (Moradi et al., 2010).

Two frequency regions are generally used to measure water vapour: infrared region near $6.3 \mu\text{m}$ and microwave region around 183.31 GHz (Buehler et al., 2008). Infrared sensors are installed on geostationary and polar orbiting satellites, while microwave sensors are only available from polar orbiting satellites (Soden and Bretherton, 1993; Buehler et al., 2008).

Infrared sounders such as the High-resolution Infrared Radiation Sounder (HIRS) (Gierens et al., 2014) provide the longest time series of water vapour measurement. Unfortunately, the HIRS instruments have been changed over this time period. Therefore, to have a consistent time series of this data, measurements had to be intercalibrated.

This has been done in recent years (e.g. Shi et al., 2008) in order to have a data package of 30 years or more. But infrared radiation cannot penetrate clouds. Cloudy regions are associated with high humidity and without filtering, they can introduce a positive UTH bias (Soden and Lanzante, 1996). Therefore, cloud filters are used, which then in turn lead to a so called clear-sky or dry bias (John et al., 2011).

Microwave measurements are more recent but have the advantage, that they are less sensitive to clouds. Buehler et al. (2007) analysed a possible dry bias introduced by cloud filtering and discussed it in comparison with a wet bias without the cloud filter. They found, that both the cloud wet bias of microwave data and, if using a cloud filter, the then created dry bias were modest for microwave data. Various studies have been conducted to create a consistent humidity data set from satellite microwave data (Buehler and John, 2005; Buehler et al., 2008; John et al., 2013). This data set will be used in the present study to analyse the evolution of UTH since 1994.

2.3.4 Simulation of Upper Tropospheric Water Vapour in Global Circulation Models

Since the 1960s, climate model studies investigate the question about water vapour feedback and upper tropospheric moisture in climate change. The question arose, if the details of cloud and convective microphysics were critical for the simulation of the distribution of relative humidity and its change under global warming (Bony et al., 2006). But several studies showed, that models had the ability to simulate the tropospheric distribution of humidity without microphysics, as long as they simulate accurately and in a realistic way the advection by the three dimensional large scale wind fields (Dessler and Sherwood, 2000; Pierrehumbert and Roca, 1998).

Minschwaner and Dessler (2004) used a single column, radiative-convective model including coupling between moistening effects of convective detrainment, drying

effects from clear-sky subsidence and radiative heating as well as cooling from water vapour to investigate the question, if the strong positive water vapour feedback could be a product of model assumptions, such as fixed relative humidity above 250 hPa. But they concluded that even under extreme assumptions regarding cloud amount, lapse rate and condensate evaporation in changing climate, the model was unable to produce a negative feedback.

Another debate in modelling concerned the evolution of relative humidity. Most of the climate models predict a small variation in global mean relative humidity under climate change inducing a strongly positive water vapour feedback (Held and Soden, 2000). The question was raised, whether this was an artefact of all climate models or a robust feature of climate change. Different studies came to the conclusion that the nearly unchanged relative humidity has to be a robust feature of climate change (Gettelman and Fu, 2008).

Bony et al. (2006) also came to the conclusion, that most current atmospheric models reproduce fairly well the seasonal and interannual variations of the upper tropospheric relative humidity. But most models seem to overestimate upper tropospheric moisture in the subsidence regions (Brogniez et al., 2005; Chung et al., 2011). This last point has to be kept in mind for the later part of this work.

The aim of this study is to analyse dry zones using UTH calculated from brightness temperatures. These will firstly be computed on the basis of model data and then retrieved from the microwave data records. The aim of the next Chapter is therefore to give an overview of the techniques and tools used to calculate UTH.

Chapter 3

Data, Tools and Methods

The data used in present study was generated within the framework of CMIP5. As UTH is a radiation variable not provided directly by those models, the model output data has to be processed using satellite simulation software. This Chapter provides information about the CMIP5 frame as well as the models considered for present study (3.1). The next Section is dedicated to the simulation software used to compute the radiation variable needed to calculate UTH (3.2). Section 3.3 gives a brief overview of the satellite data simulated and used as such in Chapter 5.5. Finally, an explanation of the calculation of UTH (3.4) and the definition of dry zones (3.5) will be given.

3.1 The Coupled Model Intercomparison Project Phase 5 (CMIP5)

CMIP5 builds on the predecessor CMIP3 and was launched in 2008, with the aim to perform a suite of climate simulations that focus on the main open questions concerning past and future climate and climate change ([Taylor et al., 2012](#)). A broad and interconnected climate research community is involved in the project, while results of the research can directly be provided to major assessment organizations like the Intergovernmental Panel on Climate Change (IPCC).

More than 20 modelling groups are working on CMIP5 simulations and over 50 numerical models have been used. Experiments have been structured in two types: long-term simulations (more than a century) and near-term simulations (with simulation for 10 to 30 years). While long-term simulations are started from multi-century preindustrial control integrations, near-term experiments are initialized with observed ocean and sea ice conditions ([Taylor et al., 2012](#)). Both types of simulations use global and coupled atmosphere-ocean models.

For the purpose of present study, long-term experiments are the interesting ones.

The core long-term simulations consist in an atmospheric model run (AMIP), a coupled control run, a historical run forced by observed atmospheric composition changes, as well as different projection simulations, the so called representative concentration pathways (RCPs), which are based on different emission scenarios. In addition, there are idealized simulations with transient climate response to gradually increasing CO₂ emissions or abrupt CO₂ increases (Taylor et al., 2012). Two of the idealized simulations are used in present study, as they allow focusing on the reaction and feedbacks of the climate system, with a unique forcing. In the following, the idealized experiments 1pctCO2 and abrupt4xCO2 are presented in more detail.

3.1.1 The Idealized Experiments of CMIP5

The 1pctCO2 Experiment

1pctCO2 is an idealized experiments, developed to analyse the transient climate response to an increasing CO₂ concentration. The experiment is initialised from the preindustrial control simulation piControl, which has been run for 1000 years with a constant forcing including well-mixed greenhouse gas concentrations kept fixed at their values of the year 1850 (Giorgetta et al., 2013). 1pctCO2 then extends over 150 years with an annual 1 % increase in CO₂ concentration. This doubles the CO₂ concentration roughly every 70 years and quadruples it roughly after 140 years. All other forcings are the same as in the preindustrial simulation (Giorgetta et al., 2013). This experiment enables analysis of the climate system’s reaction to CO₂ increase under idealized forcing, without the complications of aerosols, land-use change or others. In present study, output of the 1pctCO2 experiment is used as input for the satellite simulator COSP and the forward operator RTTOV (Section 3.2.), by which means the brightness temperature can be computed, as core input for UTH calculation (Section 3.4).

The abrupt4xCO2 Experiment

The abrupt4xCO2 experiment starts from the preindustrial control simulation piControl, but with a CO₂ concentration which is multiplied by four compared to piControl. The concentration of CO₂ is kept constant over 150 years. Similar to the 1pctCO2 experiment, the other forcings are those of piControl (Giorgetta et al., 2013). This experiment permits to diagnose the fast response of the radiation process. It is possible to separate the direct effects of CO₂ on the climate system from the indirect effects, due to the warming of atmosphere and ocean following the increase of greenhouse gas. In the case of this thesis, it is possible to analyse the

direct effect of increased CO₂ on the dry zones measured via UTH, without considering the reaction of UTH to the progressive warming of the climate system.

3.1.2 Presentation of the CMIP5 Model Selection

One of the benefits of CMIP5 is having the possibility to consider a multi model ensemble, which represents a sort of consensus representation of the climate system, with each model making its own attempt to best represent reality. The spread of this multi-model ensemble gives an indication of the reliability of the results. Unfortunately, the used CMIP5 models are different enough in their structure to render data processing via satellite simulation software (Section 3.2) time-consuming. Therefore, this study will concentrate essentially on one model, namely the model of the Max-Planck-Institute, which will be introduced in the next Section. To evaluate the output of MPI-ESM-MR, a short comparison with two other CMIP5 models, CNRM-CM5.1 and BCC_CSM1.1, will be done.

The MPI-ESM Model

The Max-Planck-Institute Earth System Model (MPI-ESM) is employed in a large number of CMIP5 experiments, for either idealized CO₂-only forcing or forcings based on observations. Experiments exist for the past as well as for the future, with the Representative Concentration Pathway (RCP) scenarios (Giorgetta et al., 2013). MPI-ESM consists of the coupled general circulation models for the atmosphere (ECHAM6, Stevens et al. (2013)) and for the ocean (MPIOM, Jungclaus et al. (2013)), and of the subsystem models for land and vegetation JSBACH (Reick et al., 2013). The submodel for the marine biogeochemistry HAMOCC5 can be switched on and has been used to initialise the carbon cycle for the control simulation (Ilyina et al., 2013).

The coupling-program named OASIS connects the atmosphere, the ocean and the land and vegetation inside MPI-ESM through the exchange of energy, momentum, water and the most important trace gases like carbon dioxide (Giorgetta et al., 2013). The atmospheric circulation is simulated by the 6th generation ECHAM (ECHAM6), which was also developed by the Max Planck Institute for Meteorology (MPI-M) in Hamburg (Stevens et al., 2013). ECHAM6 couples diabatic processes and large-scale circulations, which are ultimately driven by radiative forcing (Stevens et al., 2013). The atmosphere's vertical resolution depends on the configuration of the MPI model (Table 3.1). Independently of the resolution, every version incorporates a model top at 0.01 hPa (or about 80 km) (Stevens et al., 2013).

Via the JSBACH land model, MPI-ESM also includes dynamic feedback of vege-

tation and land use on the climate development. Land cover change data is included from external files. Orbital parameters are calculated at every radiation time step (Giorgetta et al., 2013).

MPI-ESM has been developed for different configurations, differing in atmospheric and oceanic resolution (Table 3.1). The most commonly used version in CMIP5 experiments is the low resolution version (MPI-ESM-LR). The LR resolution uses 47 vertical levels for the atmosphere (L47) and 40 levels in the ocean (L40). In present study, the mixed resolution version (MPI-ESM-MR) has been used, which provides a higher vertical resolution in the atmosphere, doubling the number of levels to 95 (L95). This permits in particular a highly resolved middle atmosphere (Stevens et al., 2013). The horizontal resolution of the atmospheric model ECHAM6 is the same for the mixed resolution as for the low resolution configuration, with T63/1.9°, but the horizontal grid spacing in the ocean is decreased from 1.5° to 0.4° (Giorgetta et al., 2013). As the main focus of the work lies on processes within the atmosphere, the atmospheric component of MPI-ESM shall briefly be presented in the next Section.

Table 3.1: Configuration and resolution of the main MPI-ESM models¹

MPI-ESM Configuration	ECHAM6 Resolution	MPIOM Resolution
LR	T63 ² / 1.9° L47	L40
MR	T63 / 1.9° L95	L40

¹ Giorgetta et al. (2013)

² lat x lon = 96 x 192 with appr. 1.875° x 1.875°

The Atmospheric General Circulation Model ECHAM6

ECHAM6 focuses on the coupling between diabatic processes and large-scale circulation. The technical details of model structure combining a dry spectral-transform dynamical core, a transport model for scalar quantities as well as a suite of parametrizations and boundary data sets, are described by Stevens et al. (2013). Stevens et al. (2013) mention the good representation of tropical variability at different timescales as one of the advantages of ECHAM6, which is due to the fact, that the improved deep convection scheme has been made more sensible to free tropospheric humidity. As examples of good representation of tropical variability, Stevens et al. (2013) names the Madden-Julian-Oscillation (MJO) and the El-Niño-Southern-Oscillation (ENSO), even though the amplitude of the spatial precipitation pattern is somewhat larger in the model than in observations. Unfortunately, some of the improvements of representation of the tropical circulation in ECHAM6 compared to the previous

models are mitigated when the model is coupled to the ocean model (MPIOM) (Stevens et al., 2013).

Considering the mean climate state, Stevens et al. (2013) mentions some persisting biases between the model output and observations. The tropical upper troposphere still presents a large cold bias of 3K in the low vertical resolution scheme, which vanishes with the high vertical resolutions in the upper troposphere (~ 200 km as in L95). In the tropics and mid-latitudes of the summer hemisphere, the atmosphere is less stable than in the reanalysis data. For the MR resolution, the zonally averaged circulation as well as the thermal structure of the atmosphere are biased compared to reanalysis data, but the amplitude of these biases is weaker than in the predecessor model versions. Stevens et al. (2013) claims a slightly shifted position of the westerlies to be at the origin of these biases. Finally, in comparison to the other global circulation models of CMIP5, the model response to increasing atmospheric CO₂ concentrations is within the mid-range of estimates. The results of present study should therefore not be influenced by a too extreme response of the atmospheric model component.

The CNRM-CM5.1 Model

CNRM-CM5.1 is a general circulation model developed jointly by the CNRM-GAME (Centre National de Recherches Météorologiques – Groupe d’études de l’Atmosphère Météorologique) and Cerfacs (Centre Européen de Recherche et de Formation Avancée) as contribution to CMIP5. CNRM-CM5.1 is composed of an atmospheric component, including a land scheme and an oceanic component as well as an ice component and river routing model (Voldoire et al., 2011). The horizontal resolution of CNRM-CM5.1 is higher than for MPI-ESM-MR, operating on a T127 triangular truncation, equivalent to a spatial resolution of about 1.4° in both longitude and latitude. But the vertical resolution is lower than for the MPI model with only 31 vertical levels (Voldoire et al., 2011).

Voldoire et al. (2011) evaluated the model results in comparison with the predecessor CNRM-CM3. Concerning the present day mean climate, they found that CNRM-CM5.1 has made clear improvements, but major errors are still present in seasonal precipitation in many regions and cloud radiative forcings, such as a double-ITCZ, a critical underestimation of low clouds on the eastern side of the tropical ocean basins, or a lack of cloud coverage over the Northern Hemisphere continents. Nevertheless global mean temperature changes over the 20th century are adequately simulated by the model, and the outcomes of CNRM-CM5.1 lie in the average of the CMIP5 models for most of the experiments.

The BCC_CSM1.1 Model

The climate model of the Beijing Climate Center (BCC_CSM1.1) is one of the two models from the BCC used to carry out CMIP5 experiments. It is a fully coupled global climate-carbon model, including interactive vegetation and the global carbon cycle. The model includes four components, for the atmosphere, the ocean, land and sea ice (Wu et al., 2014). The ocean model and sea ice model are both from the Geophysical Fluid Dynamics Laboratory (GFDL). The Atmospheric General Circulation Model (AGCM2.1) has a horizontal resolution of approximately $2.8125^\circ \times 2.8125^\circ$ (T42) (Wu et al., 2014). The estimation of the transient climate response with the BCC_CSM1.1 model through the 1pctCO2 experiment is 1.85° and falls well within the multi-model range of the CMIP5 (approximately 2°), even though the other model of BCC, BCC_CSM1.1-M is closer to the CMIP5 multiple models mean results (Xin et al., 2013). Nevertheless it is interesting to compare the results of MPI and CNRM to another model with lower resolution. That is why the BCC_CSM1.1 was chosen.

The output of the CMIP5 models does not comprise directly UTH, but with the satellite simulator COSP and its additional module RTTOV, it is possible to process the model data in order to obtain the brightness-temperature, as presented in the next Section.

3.2 Forward Operators COSP and RTTOV

3.2.1 The CFMIP Observation Simulator Package (COSP)

The variable needed to compute UTH is brightness-temperature, which is not an output variable of global circulation models, but a radiance coming from the top of the atmosphere and usually measured by satellite-based instruments. It is expressed in units of the temperature of an equivalent black body (see also Section 3.4). In order to obtain the brightness-temperature, the model data has to be transformed into synthetic satellite measurements. To achieve this, it is possible to make use of a simulator that mimics the observational process, like the one developed by the Cloud Feedback Model Intercomparison Project (CFMIP) community: the CFMIP Observation Simulator Package (COSP) (Bodas-Salcedo et al., 2011).

COSP is a software tool that enables simulation of several satellite-borne active and passive sensors, using the model data as input. It is written in Fortran 90 and operates in three steps, which are described by Bodas-Salcedo et al. (2011). First, the gridbox mean profiles of the model data are broken into subcolumns, to overcome the mismatch in scale between the model gridsize and that of a satellite pixel.

Then the vertical profiles of individual subcolumns are passed to the instrument simulators. Finally, the statistical module collects the instruments' outputs and constructs statistics comparable to observations.

3.2.2 The Fast Radiative Transfer Model RTTOV

COSP includes a large set of simulators for different instruments. For the purpose of the present study, COSP was linked to the fast radiative transfer model RTTOV, which stands for Radiative Transfer model for TIROS Operational Vertical Sounder, where TIROS is the Television Infra-Red Observing Satellite ([DWD, Glossar](#)). RTTOV is developed by several European meteorological services within the European Organisation for the Exploitation of Meteorological Satellites's Numerical Weather Prediction Satellite Application Facility (EUMETSAT NWPSAF). RTTOV simulates passive visible, infrared and microwave downward-viewing satellite radiometers, spectrometers and interferometers ([Saunders et al., 2010](#)).

As input, RTTOV needs at least mean vertical profiles of temperature and water vapour as well as surface parameters (temperature, skin temperature, pressure and wind). Optional are trace gases, aerosols and hydrometeors. RTTOV computes the top of atmosphere radiances in each of the channels of the sensor being simulated. Linked to COSP, RTTOV produces clear-sky-brightness temperature for different channels of past and current radiometers ([Bodas-Salcedo et al., 2011](#)). The sea-surface emissivity can be prescribed by the user or computed by RTTOV for each channel via the internal Fast Microwave Ocean Emissivity Model (FASTEM, [English and Hewison \(1998\)](#)).

3.2.3 Procedure Followed to Run COSP/RTTOV

In order to obtain the brightness-temperature with COSP and RTTOV, the model data output has first to be brought in the right format. Input data has to be in netCDF format. The following steps have to be taken:

- Select the needed variables from the model data output: vertical profiles of temperature, water vapour, pressure, height and the surface parameters temperature, skin temperature, pressure, wind (zonal and meridional).
- If necessary create new variables for the height (in meter), the height on half levels, the pressure and pressure on half levels.
- All variables have to be named consistently (Table 3.2 for naming of variables in present study) with *cdo cname* ([Schulzweida, 2014](#)).

- Split the input files in order to have only one timestep per file (with *cdo split time* (Schulzweida, 2014)).
- Delete the time dimension of each file, for example with *ncwa -a time* (Zender, 2017).
- Copy the files into the input folder of the COSP directory.

Table 3.2: Variables needed as input for COSP/RTTOV

Variable description	Variable code and name in ECHAM6	Variable name for COSP/RTTOV
Vertical temperature profile [K]	130 STP	T_abs
Vertical Specific humidity profile [kg/kg]	133 Q	qv
Height in full levels [m]	156 geopot. Height [gpm]	height
Height in half levels [m]	n.e. ¹	height_half
Pressure in full levels [Pa]	n.e.	pfull
Pressure in half levels [Pa]	n.e.	phalf
Surface Pressure [Pa]	134 APS	p
Skin Temperature [K] ²	169 Tsurf	tskin
10m eastward wind velocity [m/s]	165 U10	u
10m northward wind velocity [m/s]	166 V10	v

¹ does not exist explicitly as variable in ECHAM6

² temperature of the Earth's surface layer

The user interacts with COSP by means of three namelists: the COSP INPUT namelist (Appendix B.1), the OUTPUT namelist (Appendix B.2) and the cmor namelist (Appendix B.3) (Bodas-Salcedo, 2010). These have to be set before launching the simulator.

The COSP input namelist is written in the file *cosp_input.nl.txt* and contains the input arguments for COSP and all simulators. The file has to be filled with general configuration variables like the number of gridpoints to be processed, the number of levels, as well as the name of the input NetCDF files, where the input variables are located. For RTTOV, there are a number of related inputs to provide, like the platform, the satellite, the instrument, the channels and also the surface emissivity for each channel. If the latter is set equal to zero, COSP/RTTOV will start the FASTEM model to calculate the emissivity by its own.

The Climate Model Output Rewriter (CMOR) namelist encompasses the metadata, which is written to the output files. The CMOR namelist includes the path to

the directory, where the table of information of the specific Model Intercomparison Project is located, as well as to the directory, where the output files will be written.

In the `COSP_OUTPUT` namelist, the user controls the instrument simulators that are run and the list of variables written to the output file. It is possible to switch the instruments ‘on’ or ‘off’ by setting flags. To obtain the brightness-temperature, the flag for *Lrttov sim* has to be set on ‘true’ as well as for the RTTOV instrument (*Ltbrttov*).

In present study, the instrument simulated by COSP and RTTOV to calculate the brightness-temperature is the Advanced Microwave Sounding Unit-B (AMSU-B), which is a scanning microwave radiometer on board National Oceanic and Atmospheric Administration (NOAA) satellites (Saunders et al., 1995). Section 5.5 will provide a short insight into the evolution of UTH calculated directly from real observation data. The following Section shall give a short overview of the technical aspects of AMSU-B as well as an assessment of the quality and reliability of the data.

3.3 Satellite Data

The UTH data set used at the end of the present work to compare model data with observations, was derived from AMSU-B measurements from the NOAA satellites 15 and 16 (hereafter named as NOAA15 and NOAA16) by Buehler et al. (2008). AMSU-B is a cross-track scanning and total power microwave sensor with five higher frequency channels at 89.0, 150.0, 183.31 ± 1.00 , 183.31 ± 3.00 and 183.31 ± 7.00 GHz (Table 3.3), primarily used for humidity sounding from the surface up to 200 hPa (Saunders et al., 1995).

Table 3.3: Channel Characteristics of the AMSU-B Instrument ¹

Channel	Central Frequency, GHz
16	89.0
17	150
18	183.31 ± 1.0
19	183.31 ± 3.0
20	183.31 ± 7.0

¹ from the WMO Observing Systems Capability Analysis and Review Tool (OSCAR) (WMO, 2016)

The swath width from AMSU-B, which is the linear ground distance over which the scanner is tracking (at right angles to the line of flight), is of approximately 2300 km, with 90 individual measurement pixels along the swath. The Earth viewing angles range from -48.95° to $+48.95^\circ$ with the innermost scan position laying at 0.55° from either side of nadir (Saunders et al., 1995).

Data for this study was taken from channel 18 at 183.31 ± 1.00 GHz, because the sensitivity of brightness temperature for this frequency to relative change in the humidity is highest in the upper troposphere. This can be visualised through the Jacobians, which are defined as the first partial derivative of the brightness temperature with respect to the water vapour volume mixing ration (Section 3.4). For the frequency of 183.31 ± 1.00 GHz the Jacobian peaks in the upper troposphere (Figure 3.1).

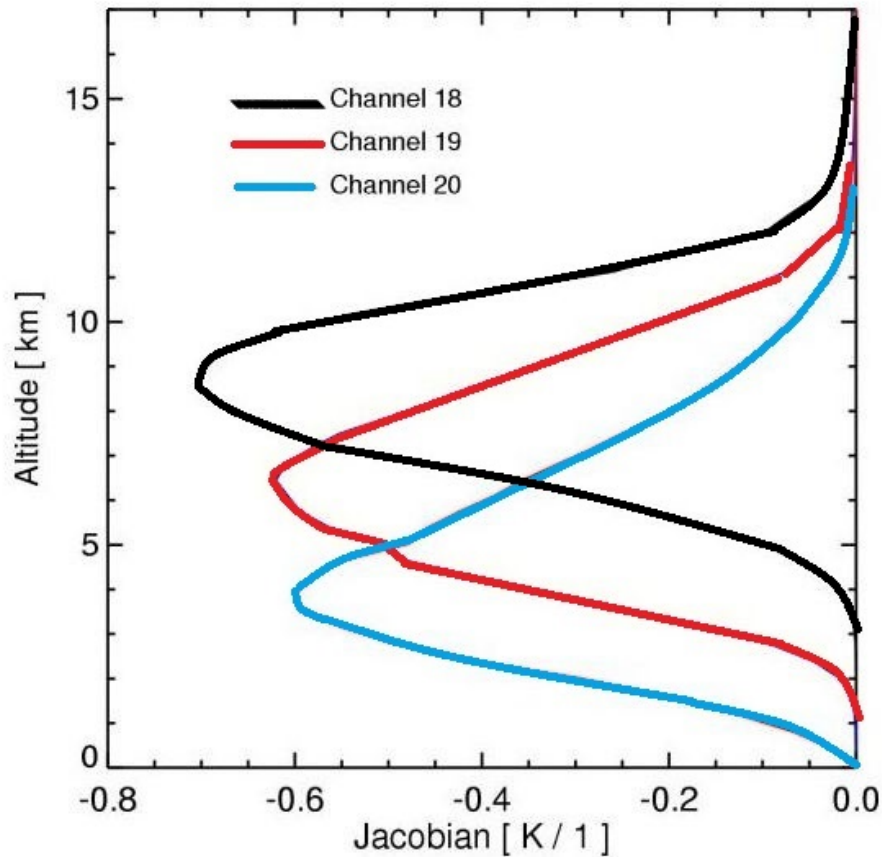


Figure 3.1: Jacobians of the AMSU-B channels 18, 19 and 20 for a midlatitude summer atmosphere, from simulations made with the Atmospheric Radiative Transfer Simulator (ARTS). Figure used with courtesy of Viju O. John (see Copyright Notices).

Only the data from NOAA15 and NOAA16 was used, because this data had been tested already by [Buehler et al. \(2008\)](#) and was at hand. NOAA17 could have been used, but the operation time of this sensor was shorter and [Buehler et al. \(2008\)](#) also noticed that the bias between NOAA16 and NOAA17 was not stable during the operation time, but drifted from approximately -1 % to +2 % for an unidentified reason. NOAA15 was launched in 1998 and AMSU-B was turned off on 28 March 2011 ([WMO, 2016](#)). NOAA16 was operational from 2001 to 2014 ([WMO, 2016](#)). The dataset is structured in time periods of one month and in 1.5° x 1.5° latitude-longitude grid cells.

Because of the important impact of convection on the humidity budget, it is preferable to have daytime humidity measurements. Therefore, only daytime flights, so called ascending flights, have been taken into account. But [Buehler et al. \(2008\)](#) detected, that UTH calculated from NOAA15 was systematically drier than UTH from NOAA16. For both instruments, the ascending measurement had been chosen to compute UTH, but the exact observation time was different between NOAA15 and NOAA16, as for the ascending flight branch both satellites cross the Equator at different times during the afternoon, especially during the first five years of operation (Figure 3.2). This could be one reason for the bias between the two sensors.

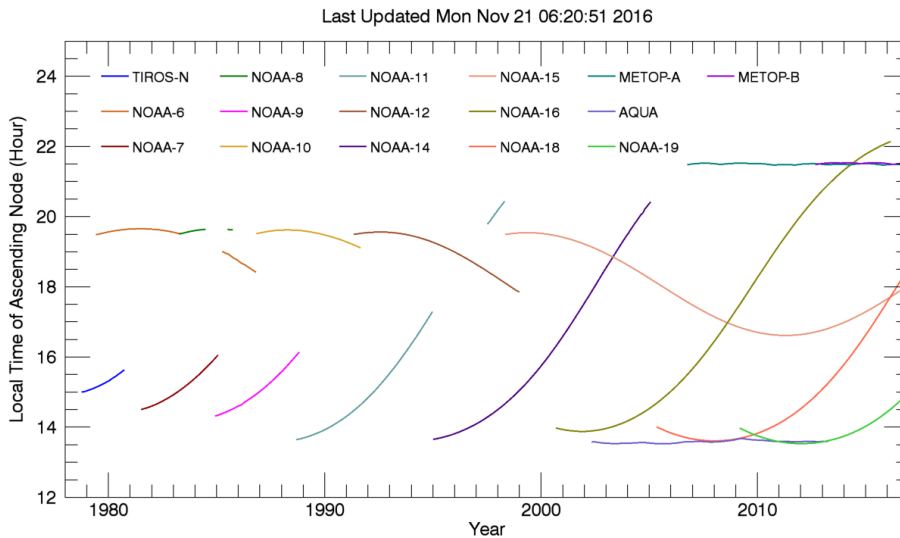


Figure 3.2: Local ascending node crossing time for microwave sounding instruments MSU/AMSU on NOAA, EUMETSAT, and NASA platforms.¹

¹Permission granted by Remote Sensing Systems, see Copyright Notices

3.4 The Brightness Temperature Transformation Method

To retrieve UTH from microwave measurements with the AMSU-B instrument, [Buehler and John \(2005\)](#) developed a method based on fractional water vapour volume mixing ratio (VMR) Jacobian. UTH is defined as the relative humidity with respect to liquid water, weighted by the AMSU-B Channel 18 Jacobian:

$$\text{UTH}(\theta) = \frac{\sum_j K_j^{18}(\theta) \text{RH}_j}{\sum_j K_j^{18}(\theta)}. \quad (3.1)$$

RH_j is the relative humidity at altitude level j with respect to liquid water. $K_j^{18}(\theta)$ is the fractional water vapour VMR Jacobian defined by

$$K_j^{18}(\theta) = \frac{\partial T_b^{18}(\theta)}{\partial x_j}. \quad (3.2)$$

Here j is the vertical grid index, ∂ stands for the partial derivative and T_b^{18} is the brightness temperature measured with the AMSU-B channel 18. x_j is the water vapour volume mixing ratio in fractional units defined by

$$x_j = \frac{\text{VMR}_j^{\text{H}_2\text{O}}}{\text{VMR}_j^{\text{Ref}}}, \quad (3.3)$$

which depends on the reference profile of VMR. Because water vapour distribution in the atmosphere varies largely with climate zone and season, the Jacobians depend on atmospheric conditions. In Figure 3.1 only the Jacobians for midlatitude summer climate are shown. Channel 18, with its frequency of 183.13 ± 1.00 GHz, peaks in the upper troposphere and permits UTH retrieval from a broad layer centred roughly between 6 and 8 km height in the tropics. Note that this height is lower in the midlatitude winter or in the polar regions ([Buehler and John, 2005](#)).

The base for the UTH calculation from radiances is the relation between infrared radiances and UTH derived by [Soden and Bretherton \(1993\)](#):

$$\ln(\text{UTH}) = a + bT_j, \quad (3.4)$$

where $\ln()$ is the natural logarithm, T_b is radiance expressed in brightness temperature, and a and b are constants. Based on this relation, [Buehler and John \(2005\)](#) developed a method to retrieve UTH from microwave radiances. This was done by determining the constant coefficients a and b via a linear regression between the UTH values calculated by equations 3.1 to 3.3 and simulated radiances from microwave sensors. These coefficients were calculated for UTH with respect to liq-

uid water and with respect to ice, and depend on the viewing angle of the sensor (Buehler and John, 2005). For the purpose of present study, only the parameters corresponding to UTH with respect to liquid water and for the nadir looking sensor (smallest viewing angle) have been used:

Table 3.4: Transformation Parameters for the calculation of UTH

θ [°]	$a(\text{water})^1$	$b(\text{water}) [K^{-1}]$
0.55	16.474	-0.0702169

¹ dimensionless

The UTH dataset compiled by Buehler et al. (2008) includes measurements from all viewing angles with their corresponding scaling coefficients. At higher latitudes, the surface is visible in the radiance data because water vapour content is low. Thus, only the area between 60°S and 60°N is covered. To further prevent that microwave humidity data are affected by clouds and surface influence, a filter has been used, which can screen out both contaminations (Buehler et al., 2007). Clouds affect microwave measurements significantly less than infrared measurements, but can still impact the measurement, if they are high enough to be seen by the channel and if they contain a minimum of ice. Not filtering these clouds could lead to a wet bias, if the clouds were interpreted as water vapour. On the other hand, a cloud filter can introduce a dry bias, if too much moisture is filtered. Buehler et al. (2007, 2008) analysed both biases, the dry bias due to the filter and the wet bias without cloud filter, and came to the conclusion, that they both were modest and that the real all-sky UTH would be found somewhere between the filtered and the unfiltered microwave UTH values.

But the main part of present study is consecrated to UTH calculated from model data. Section 3.2 described the way to obtain brightness temperature from the model data. For the calculation of UTH, the same method was used as for the satellite data. To be consistent, the forward operator COSP has been set to simulate the AMSU-B sensor. It was therefore possible to select the output of Channel 18 and to calculate UTH with the same method as for the real satellite data. For the parameters a and b the nadir viewing angle was chosen (Table 3.4). UTH can be calculated by

$$\text{UTH} = \exp(a_w + b_w T_b), \quad (3.5)$$

where a_w and b_w are the coefficients for UTH with respect to liquid water.

3.5 Definition of the Dry Zones

Once UTH is computed, dry zones can be identified in the UTH distribution. Generally, if scientists speak of ‘dry zones’ or ‘dry regions’ in the subtropical atmosphere, they mean the subsidence zones at the edge of the Hadley circulation (e.g. [Lu et al., 2007](#); [Scheff and Frierson, 2012](#)). In present thesis, the expression dry zones refers to all regions in the tropics and subtropics where UTH is smaller than a determined threshold. For UTH calculated from model data, this threshold has been set to 40 % RH (Figure 3.3). Smaller thresholds (30 % RH and 20 % RH) have been set to study the intensity or the deepening of dry zones.

In analogy to [Roca et al. \(2011\)](#) and [Schröder et al. \(2014\)](#), new variables will be introduced, to study the behaviour of the dry parts of the distribution: the frequency of occurrence of UTH below 40 % (UTHp40) and below 30 % (UTHp30). Regions where UTHp40 or UTHp30 are high, correspond to regions, where the seasonal average of UTH is low.

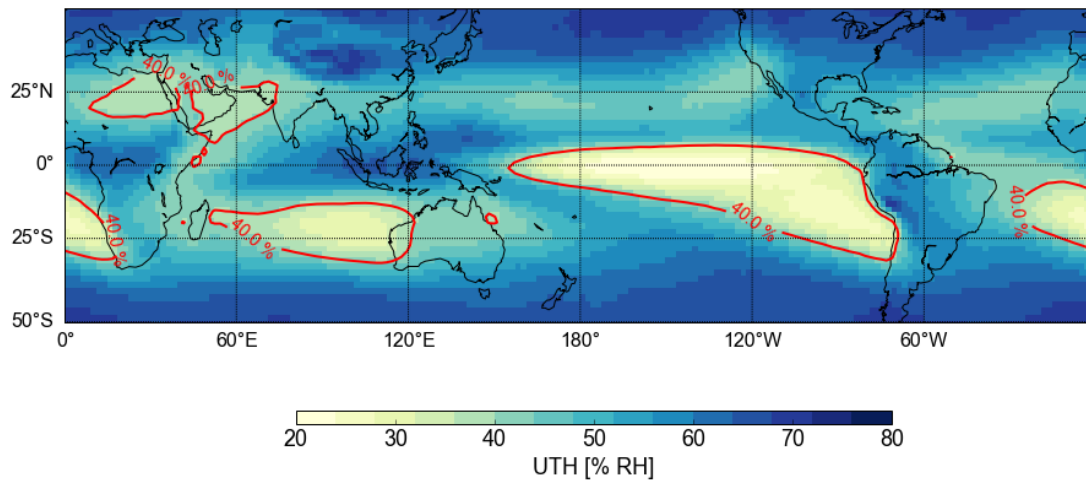


Figure 3.3: Yearly mean UTH for first decade of MPI-ESM-MR 1pctCO2. The red contour lines indicate the limits of regions with UTH smaller than 40 %.

Chapter 4

Current State of Research

4.1 The Seasonal Cycle of UTH

In order to distinguish between natural variability and climate change, it is necessary to know the natural seasonal variation of humidity in the upper troposphere. Since the 1990s, scientists study the distribution and evolution of the upper troposphere with satellite observations and simulations with global circulation models (GCMs). It is known since then, that water vapour concentrations are larger in summer hemisphere in all latitudes, influenced by the seasonal shift of the Hadley Cell (DelGenio et al., 1994). With the evolution of satellite-based measurements, it became possible to develop a more detailed view of the distribution and seasonal evolution of upper tropospheric moisture. High relative humidities are measured in the tropical upper troposphere in convection regions, while the peak in relative humidity migrates from South of the Equator in December to February to North of the Equator in July to August (Gettelman et al., 2006). Lower relative humidities are found in subtropical winter hemisphere, following the pattern of the Hadley circulation. The equatorial Eastern Pacific was revealed to be the driest region of the tropics throughout the year, while Asian and North American monsoons dominate the moisture budget in boreal summer (June to August) (Gettelman et al., 2006). Very low relative humidities are also found in the North-Central Pacific from December to February and over central Asia and the Middle East from July to August, where even in the upper troposphere air is still warm, but isolated from the moisture of the Asian monsoon complex (Gettelman et al., 2006).

DelGenio et al. (1994) investigated the reasons for the larger water vapour concentrations in the summer hemisphere in GCM simulations and found four mechanism playing a role in the moistening budget: First of all the mean meridional circulation with its rising and sinking branches, secondly the moist convection which moistens the upper troposphere through detrainment, thirdly the eddies, which

moisten/dry the atmosphere in regions of convergence/divergence and finally the stratiform cloud condensation and evaporation mechanism. [DelGenio et al. \(1994\)](#) concludes, that the most important moistening source for the upper troposphere are the large-scale eddies, which transport moisture upward and poleward, while cloud formation represents the major vapour sink. As these mechanisms are revealed to be the relevant regulators of UTH, it would be expected that a change in these mechanisms in global warming must also impact the UTH distribution.

4.2 Trends from Model Data

The first studies concerning future evolution of upper tropospheric moisture were conducted with climate models. It has been predicted, that eddies weaken in a warmer climate because smaller meridional temperature gradients reduce the available potential energy driving baroclinic instability ([DelGenio et al., 1994](#)). But as the vertical gradient of specific humidity is stronger in a warmer climate, the eddies could also transport more moisture upward and so the first expected consequence would be that moistening occurs in all latitudes, which would lead to a decrease in upper tropospheric dry zones ([DelGenio et al., 1994](#)).

However, recent research reveals a widening of the tropical belt, implying a poleward expansion of the dry regions situated at the latitudes of the subtropical subsidence zones (e.g. [Birner et al., 2014](#); [Seidel et al., 2008](#); [Lu et al., 2007](#); [Hu and Fu, 2007](#)). [Lu et al. \(2007\)](#) reported a consistent weakening and poleward expansion of the Hadley circulation analysing the models of the AR4 project, and associated these circulation changes with a poleward expansion of the subtropical dry zones. They stated, that the expansion of the Hadley Cell is probably caused by an increase in the subtropical static stability, which pushes poleward the outer boundary of the Hadley Cell. Following this study, regions poleward of the tropical subsidence zones would become drier. Different metrics have been used to measure the tropical widening, including the subtropical jet stream, the tropopause height, and the field of precipitation minus evaporation (P-E). However, most of these parameters are connected to UTH via the Hadley circulation ([Lu et al., 2007](#); [Seidel et al., 2008](#)).

4.3 Trends in Observations

In the past 30 years, satellite radiance observations sensitive to water vapour and temperature of the upper troposphere have become more and more reliable and the time series of observations longer, so that it is possible to make the first studies of trends in UTH. [Bates and Jackson \(2001\)](#) use 20 years of measurements of the High-resolution Infrared Radiation Sounder (HIRS) to study UTH and found decadal

trends, which are strongly positive in the deep tropics, negative in the Southern Hemisphere subtropics and midlatitudes, and of mixed sign in the Northern Hemisphere subtropics and midlatitudes. These measured trends have been found to be in phase with the seasonal cycle. Positive trends of UTH were identified over the monsoon regions in summer season and negative trends over subtropical subsidence regions during winter season. Furthermore, [Bates and Jackson \(2001\)](#) identified an evolution of UTH consistent with the increased frequency of El Niño-Southern-Oscillation (ENSO) warm events in the 1990s. This evolution comprised an increase of UTH in the central and eastern equatorial Pacific and a decrease of UTH in the subtropics as well as over the Indonesian region. Similar to the findings in the models, HIRS data showed negative trends in UTH poleward of the deep tropics, which could be related to the large-scale circulation changes especially of the Hadley Cell. Subtropical locations with decreasing UTH were identified by [Bates and Jackson \(2001\)](#) as regions of preferred equatorial propagation of extratropical Rossby waves. The Rossby waves diminish transient eddy activity and thus create very dry conditions. In general [Bates et al. \(2001\)](#) hypothesized that the variation in the Rossby wave activity modulates the vertical water vapour flux and is therefore responsible for the variation in tropical UTH.

Ten years later, [Shi et al. \(2011\)](#) intercalibrated the now 30 years of HIRS clear-sky measurements and studied again the trends in UTH. They found an increase of UTH in the equatorial tropics between 30°N and 30°S of about 0.0052 % per year. This increasing trend of UTH is especially visible over the Equator, while in the same time humidity is decreasing slightly in the subtropics between 20° and 30° on both hemispheres. [Shi et al. \(2011\)](#) also analysed the areal coverage of high and low humidity values, which both show positive trends over this period. Their results suggest the possibility of enhanced convective activity in the tropics during the three decades from 1979 to 2009. To achieve a higher level of statistical confidence, the authors indicate that longer time series would be required.

[Schröder et al. \(2014\)](#) used the concept of frequency of occurrence of UTH smaller than 10 % to analyse UTH (which they called free tropospheric humidity (FTH)) calculated from infrared data from the Meteosat clear-sky radiance archive (CSR) covering the period of July 1983 to June 2005. They found that the strongest trends for the frequency of occurrence of FTH smaller than 10 % (FTHp10) were observed in areas, where there is a strong gradient between dry and wet regions, and in dry areas. These results have not proved to be significant, but they are consistent with theoretical considerations in both the sign and small magnitude of the change over the analysed 25 years ([Schröder et al., 2014](#)).

Chapter 5

Evolution of Dry Zones in the Upper Troposphere

This Chapter encompasses the results of the study of UTH and the upper tropospheric dry zones calculated from model data via the simulation software COSP. The first Section (5.1) gives an overview of the general distribution of dry zones from the MPI-ESM-MR model at the beginning of the 1pctCO₂ run (without the influence of additional CO₂). Section 5.2 presents the evolution of the dry zones with progressively increasing CO₂ concentration in the model run 1pctCO₂ and tries to give some explanations of the so found changes in UTH and dryness. The third Section of this Chapter (Section 5.3) analyses the change in upper tropospheric dry zones in the abrupt4xCO₂ model run. Finally the results will be discussed in comparison with other CMIP5 models (Section 5.4) and real observation data (Section 5.5).

5.1 General Distribution of the Dry Zones

Figure 5.1 shows the mean UTH distribution in the first decade of the 1pctCO₂ run of the MPI-ESM-MR model for the months December to February (top) and June to August (bottom). The contour lines indicate the limits of UTH lower than 40 % RH (red line) and 20 % RH (yellow line). For the interpretation of the results it is helpful to remember that UTH is a measure of relative and not of absolute humidity. This can be directly observed in regions with subsidence, which appear drier, as sinking air masses warm adiabatically leading to a decrease in relative humidity, while uprising air masses cool and show increased relative humidity.

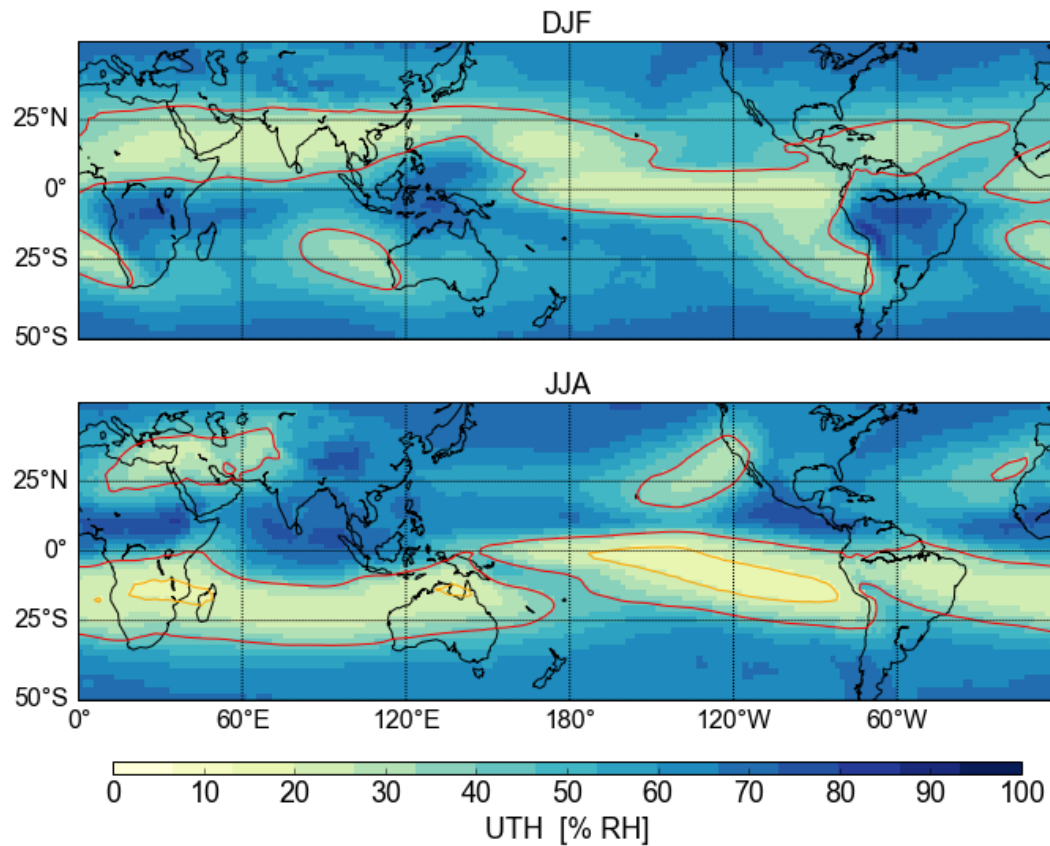


Figure 5.1: UTH in DJF (top) and JJA (bottom). The contour lines indicate the limits of regions with UTH smaller than 40 % (red) and smaller than 20 % (yellow)

The intertropical region, lying roughly between 30°S and 30°N, is characterised by a sharp contrast between the convective regions with high UTH values and the dry subsidence zones north and south from ITCZ. The tropical regions of high UTH values in Figure 5.1 correspond to the uprising branches of the Hadley and the Walker circulation, and can be compared for instance with maps of the seasonal mean relative humidity at 500 hPa from satellite measurements (e.g. [Roca et al., 2011](#), Figure 1).

During boreal winter (DJF), when the ITCZ, characterized by a maximum in UTH, is on his southernmost position, the main dry zones are located between the Equator and approximately 25°N. Only in the East Pacific the dry region is crossing the Equator to the South and reaches 25°S along the South-American coast. The lowest values of UTH can be found in two zonal bands: one is laying over the North-Pacific and extends from approximately 160°E to the west coast of the American continent. The second dry band crosses parts of Northern Africa, the Arabian Peninsula and India, and reaches East Asia. Beside the main dry zones on the Northern Hemisphere, there are also smaller regions with low UTH in front of the

western coasts of Africa, Australia and South America around the southern 25° latitude. Two smaller dry zones are also situated in the north-western oceans, in the North-West Pacific between Hawaii and Indonesia, and in the Caribbean Atlantic. The moistest regions are parts of the ITCZ located mainly over the continents south from the main dry belt, especially over southern Africa, the Maritim Continent and South America.

From June to August (JJA) the dry zones are located mainly on the Southern Hemisphere, and nearly form a belt from Brazil over the Atlantic Ocean to South Africa, across the Indian Ocean and over the north of Australia. Another marked dry region can again be found in the Pacific Ocean from the central Equator to the western coast of South-America up to 25°S. This dry zone is particularly dry in the centre, which reflects the fact, that this region is corresponding to the subsiding branch not only of the Hadley Cell but also of the Walker Cell, which is most prominent in the Pacific. The highest UTH values correspond again to regions in the ITCZ and to the settings of monsoon circulations over West Africa, Central America and South East Asia.

The distribution of UTH calculated from the MPI model data at the beginning of the 1pctCO2 run thus corresponds quite well to the distribution known from satellite measurements (e.g. [Roca et al., 2011](#); [Gettelman et al., 2006](#); [Milz et al., 2009](#); [Buehler et al., 2008](#)). Therefore, this can be used as a starting point to analyse the evolution of the dry zones with increasing CO₂ concentration and temperature.

5.2 Evolution of UTH and the Dry Zones with Progressively Increasing CO₂ Concentration

5.2.1 Global View in MPI-ESM-MR Model and 1pctCO2 Run

The first step of this study will be to analyse the evolution of the dry zones over the 150 years of the model run, where CO₂ concentration is gradually increasing by 1 % each year. As explained before, the distribution of dry and moist areas strongly depends on the seasons. This is why in the present study boreal winter (DJF) and boreal summer (JJA) are considered separately. The first part of this Section will consist in an overview of the global evolution of UTH for DJF and JJA during the model run. The aim of doing this is to show, that the changes in UTH structure are gradual, and prove that for the following analyses it will be sufficient to consider the first and the last decade of the model run. In the following Subsection, the behaviour of the dry zones will be analysed in both hemispheres. Finally, the spa-

tial distribution of the Dry zones and their changing in the course of the 1pctCO₂ experiment will be presented from a global point of view.

Decadal Evolution of UTH in DJF and JJA

In the 1pctCO₂ run of the MPI model (Figure 5.2), the winter dry zones in the Northern Hemisphere stay at the same positions between 0° and 25°N (Section 5.1), but their width changes. At the end of the simulation (1990-1999), the dry zones in the Pacific become moister, while the dry zone in the Caribbean has become significantly wider and drier. The dry zones over North-Africa, the Arabian Peninsula and India stretches to the North over Africa, almost reaching the Mediterranean Sea.

In the same time on the Southern Hemisphere, which then experiences summer, the drier regions over the oceans near the western coasts of Africa, Australia and South America show increasing UTH over the 150 years. Even though still drier as in the surroundings, the upper troposphere becomes moister in these regions during austral summer (DJF).

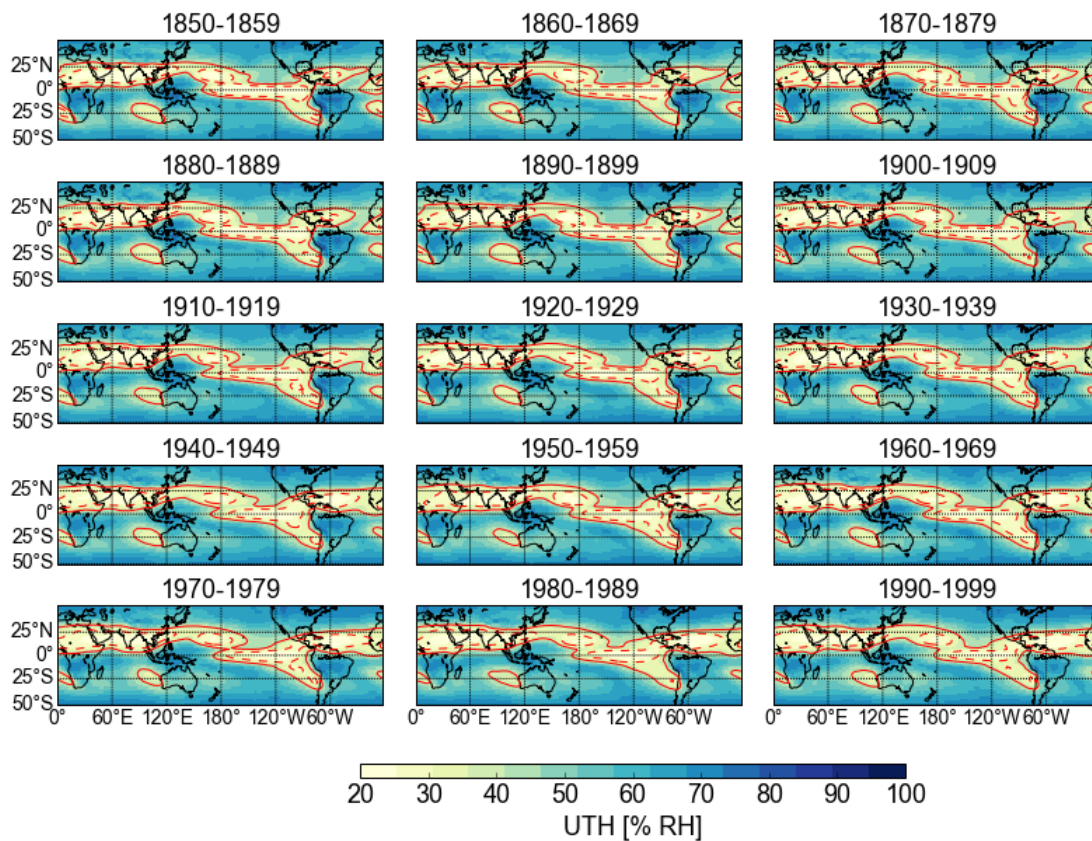


Figure 5.2: UTH in DJF for 150 years subdivided in 10 year mean periods. The contour lines indicate the regions with UTH smaller than 40 % (red line) and 30 % (red dotted line).

In boreal summer (JJA), when the main dry belt lies in the Southern Hemisphere, the structure of the dry zones remains the same over the 150 years of the model run (Figure 5.3). Similarly to the evolution in DJF, the Pacific dry zone between 0° and 25°S near the western coast of South America decreases in area and intensity. The rest of the dry belt at the same latitude, stretching from South America over Africa and Australia, which is then in winter season, becomes drier, especially in the Indian Ocean near the west coast of Australia.

In the Northern Hemisphere, two smaller dry zones are located over the eastern ocean basins west of the western borders of the continents, one near California above the Pacific Ocean and the other one near North Africa and Spain above the Atlantic Ocean. In these drier areas UTH is not as low as in the southern dry belt and UTH is slightly increasing here over the 150 years.

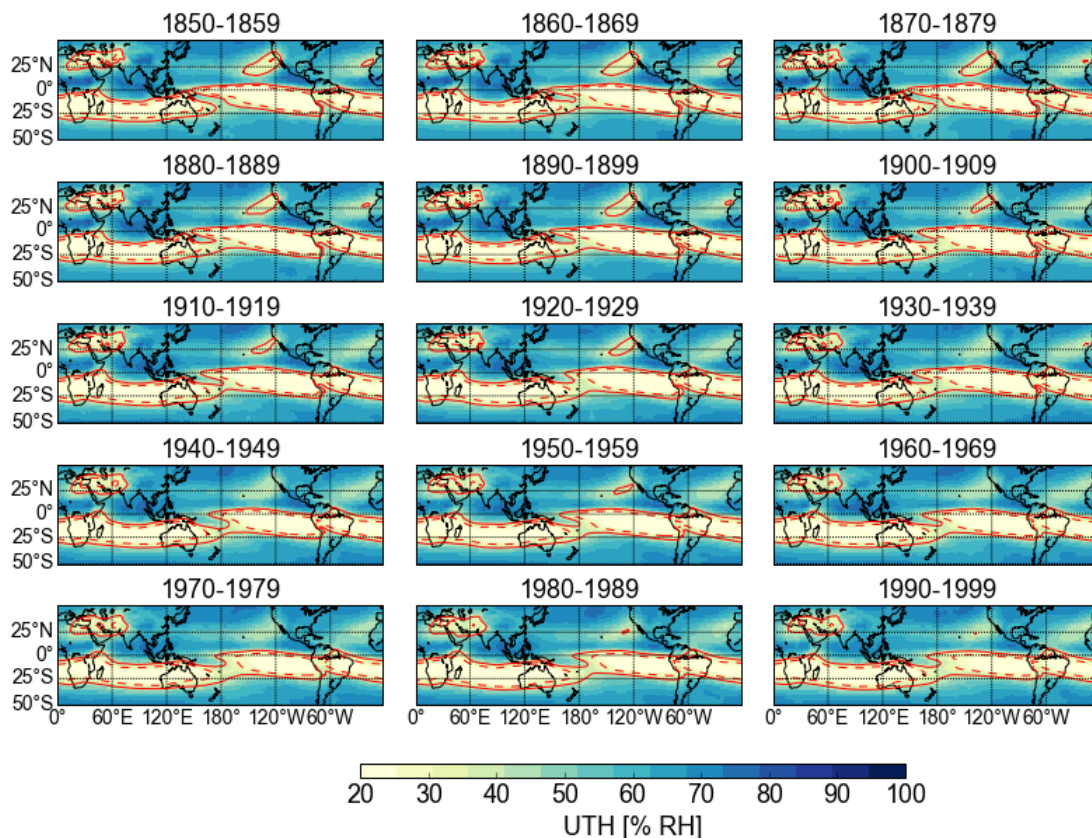


Figure 5.3: UTH in JJA for 150 years subdivided in 10 year mean periods. The contour lines indicate the regions with UTH smaller than 40 % (red line) and 30 % (red dotted line).

The evolution of the dry zones in the 15 decades of the 1pctCO₂ simulation shows, that while the gross structures of the dry zones stay the same, the dry zones in the winter hemisphere become wider and UTH decreases. In the summer hemispheric dry zones, UTH slightly increases. The South-Eastern Pacific represents

a special case, where the dry zones stretching from North-West in DJF to South-East in JJA decrease in both seasons. The changes are not abrupt, but progressive, and especially the last decade does not stick out of the global evolution. Therefore, it is not misleading to concentrate on the differences between the first and the last decade to analyse the changes in UTH over the 1pctCO₂ run of the model.

Seasonal Analysis of Dry Zones in Northern and Southern Hemisphere

The main subsidence regions are situated at the poleward edges of the Hadley Cells. Therefore, in the following Section, the Northern Hemisphere is delimited from the Equator (0°) to 45°N and the Southern Hemisphere has been delimited from 0° to 40°S . For a first approach, the histograms of UTH for both hemispheres for the first and the last decade of the 1pctCO₂ run of MPI-ESM-MR have been analysed (Figure 5.4).

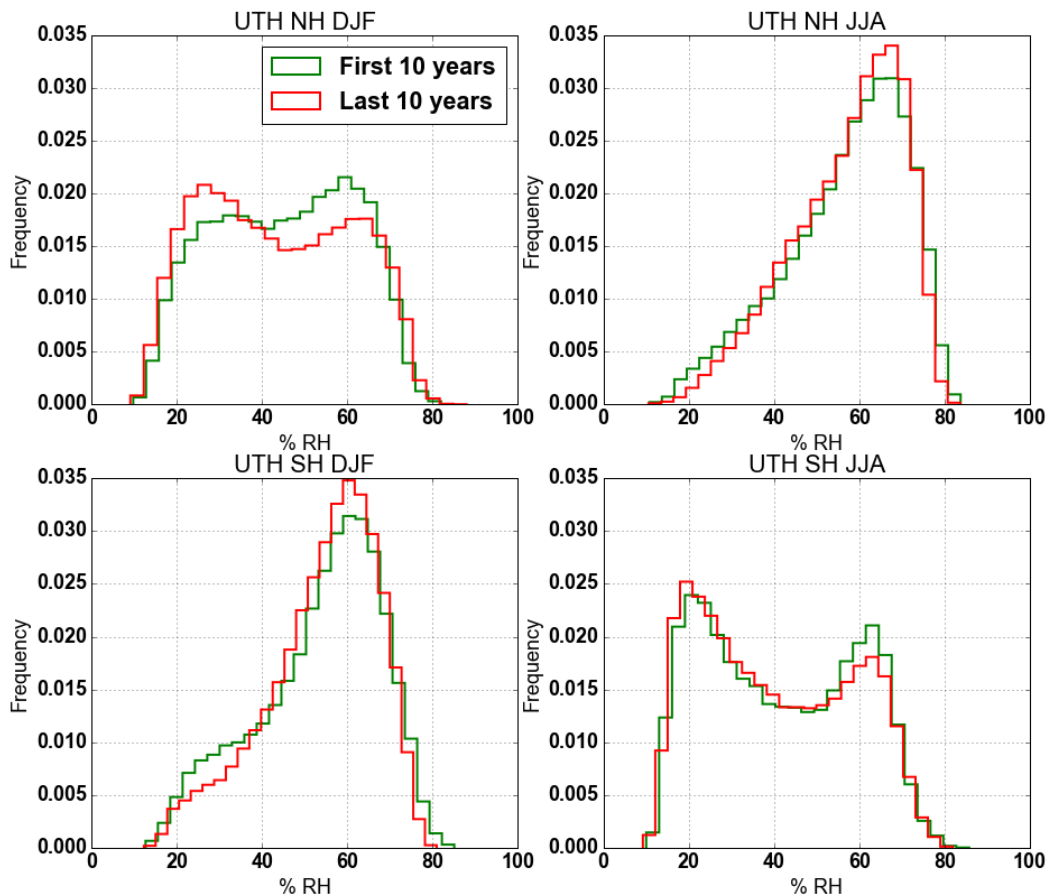


Figure 5.4: Histograms of first decade (green) and last decade (red) of UTH for the Northern Hemisphere (top) and the Southern Hemisphere (bottom), in DJF (left) and JJA (right).

Winter and summer distributions of UTH differs in both time periods and each hemisphere. In summer (JJA in NH, DJF in SH), the distribution of UTH only peaks once between 60 % RH and 70 % RH. The distribution is not Gaussian; While the values with higher UTH than the peak represent only a small part of the whole number of gridpoints, in the dry part values of UTH smaller than 50 % are more evenly distributed. The peak in the wet part probably represents the ITCZ. The general form of the distribution does not change much between the first and the last decade of the experiment. Nevertheless, the peak in the wet part increases in both hemispheres and the distribution becomes narrower, indicating a strengthening and concentration of the very moist regions.

In winter, the distribution of UTH manifests two maxima. There is still a peak near UTH of 60 %, due to the ITCZ crossing the Equator to the Winter Hemisphere. The secondary peak between 20 % and 40 % indicates the existence of important dry regions in the winter hemisphere. For the last decade of the run, the maximum in the dry part strengthens, while the maximum in the moister part is reduced. The portion of dry grid points increases. The slight shift in the dry peak towards the drier end of UTH is a sign of deepening of the dry zones.

The focus of the present study is on the dry part of the UTH distribution. Therefore, the time series of UTH smaller than 30 % RH (UTHp30) has been plotted in Figure 5.5. Over the 150 years of the 1pctCO₂ run, UTHp30 increases in winter (DJF) in the Northern Hemisphere by approximately 7.38 % over the whole period. In the first 30 to 40 years, the fraction of UTH smaller than 30 % RH is stagnating or even decreasing slightly, but afterwards UTH is clearly increasing.

This positive trend can also be observed in winter (from June to August) in the Southern Hemisphere (Figure 5.5). At the beginning of the model run, the frequency of occurrence of UTH smaller than 30 % is significantly higher in the Southern Hemisphere than in the Northern Hemisphere (around 40 % in SH against around 20 % in NH) and is only slightly decreasing in the first 30 years (-0.09 %). But the global trend is still positive with about 5 % increase for the whole period.

During summer, from June to August in the Northern Hemisphere and from December to February in the Southern Hemisphere, the fraction of UTHp30 is smaller (around 10 % in the Northern Hemisphere and around 6 % in the Southern Hemisphere) and decreasing in both hemispheres by around -2.3 % for the whole period, meaning that the dry regions become smaller in summer after the 150 years of increasing CO₂ concentration (Figure 5.5). But as the positive trends of the frequency of occurrence of dry UTH in winter are higher than the negative trends in summer, the overall trend points towards an increase in the dry zones.

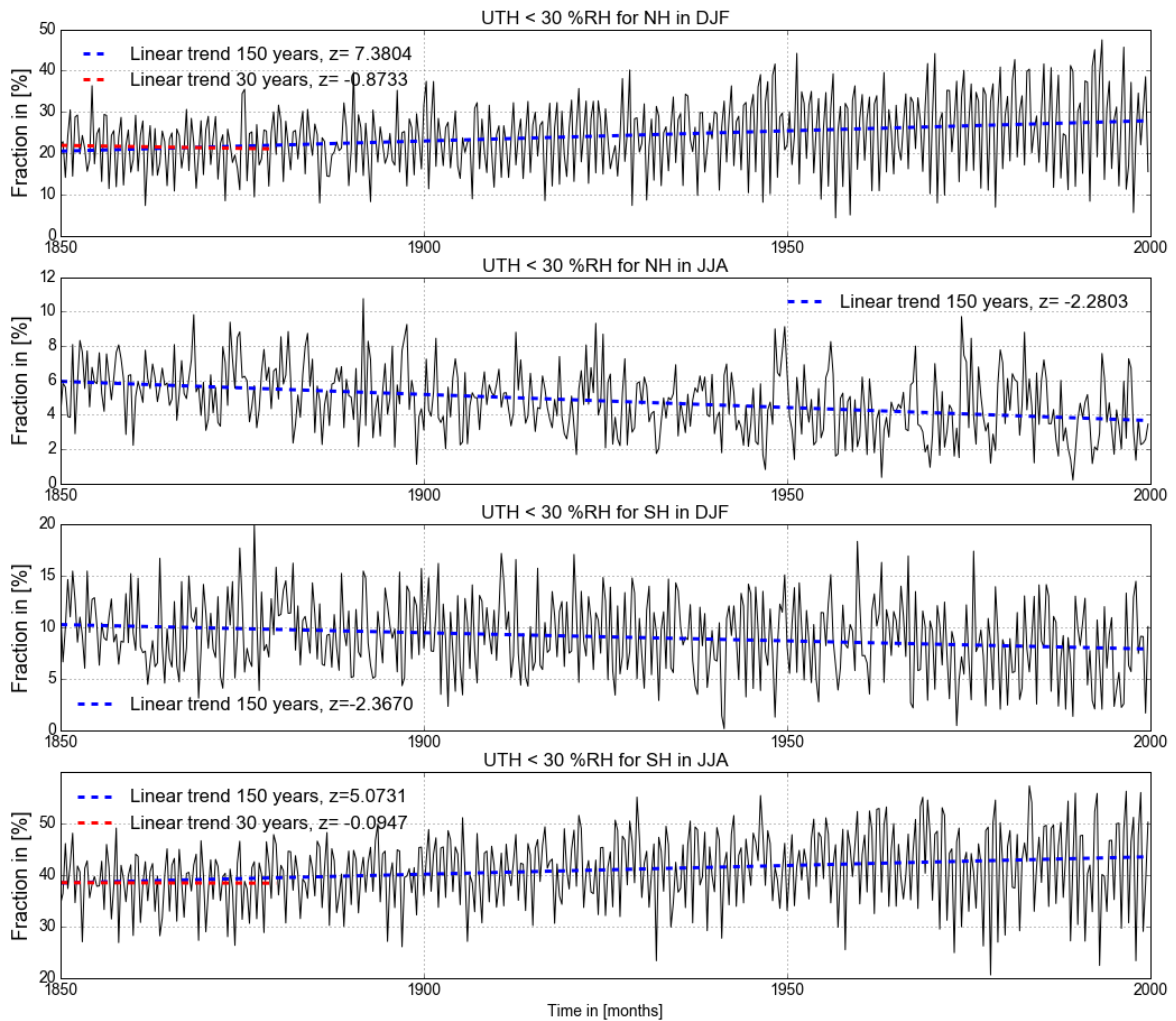


Figure 5.5: Timeseries of fraction of UTH smaller than 30 % in the Northern Hemisphere in winter (top), Northern Hemisphere summer (second from top), Southern Hemisphere in summer (second from bottom) and Southern Hemisphere in winter (bottom) for the 150 years of the 1pctCO₂ run of MPI-ESM-MR and their linear trends (blue dotted line). For NH in DJF and SH in JJA the linear trend of the first 30 years is shown (red dotted line).

Spatial Distribution of the Dry Zones

As seen in Figure 5.2 and 5.3, the evolution of UTH in the 150 years of the model run does not show any important jumps or breaks. Therefore, it is possible to compare the last and the first decade of the model run to have an idea of the evolution of the dry zones under the influence of constant increase of CO₂ concentration.

Figure 5.6 illustrates the fact, that the dry zones generally stay at the same positions during the 150 years of the model run. The most obvious changes occur around the tropics between 40°S and 40°N and in particular at the edges of the

original dry zones, where the gradients between dry and moist are the largest. This finding is conform to the predicted changes in atmospheric circulation, more precisely to the poleward shift of the edges of the Hadley Cell ((e.g. [Hu and Fu, 2007](#); [Lu et al., 2007](#); [Johanson and Fu, 2009](#))).

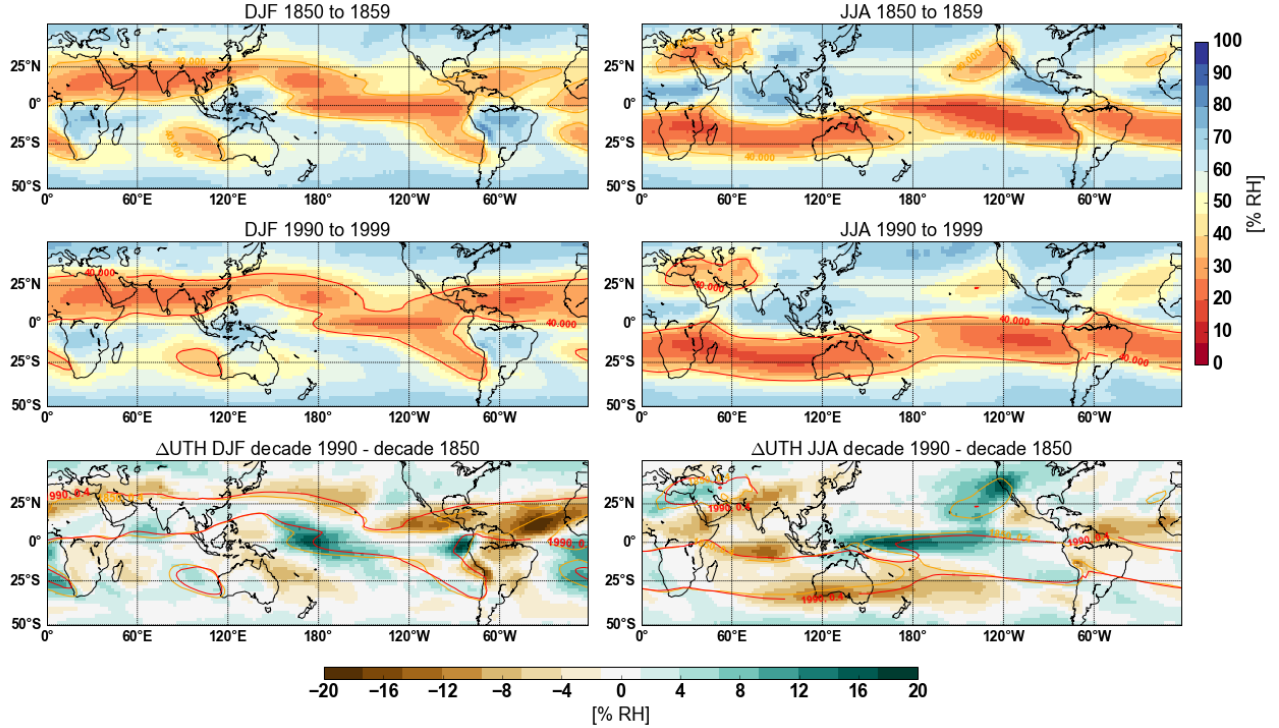


Figure 5.6: UTH in the first decade 1850-1859 (top) and the last decade 1990-1999 (middle) of the 1pctCO₂ run of MPI-ESM-MR model and the difference between both decades (bottom) for DJF and JJA. The contour lines in the bottom plot indicate the regions with UTH smaller than 0.4 in 1850-1859 (green) and in 1990-1999 (red).

UTH is decreasing especially on the poleward edges of the dry zones in the winter hemispheres, which is conform to the fact, that the main subsidence zones are situated in the winter hemisphere. In DJF, the regions with drying trends in the 150 years of the model run, lie over Northern Africa, the Arabian Peninsula, the North-West Pacific Ocean and over central America and the central Atlantic Ocean. Regarding the 30%-UTH-contour-line, these drier regions are all located at the edge of the primary dry zones, except for the Atlantic Ocean.

In JJA these structures are not as clear. The southern edges of the dry zones lying in the winter hemisphere feature decreasing UTH only in the South-Eastern Indian and the South-Western Pacific Oceans, including South-Australia. However, larger regions of decreasing UTH are located over central Africa, India, the Indian and the central Atlantic Ocean. For these regions there has to be other explanations for the drying trend than the poleward extension of the Hadley Cells.

In the summer hemispheres, well-defined dry zones are located over the oceans, west from the continents, in the South-East Indian, Atlantic and Pacific Ocean west from Australia, Southern Africa and Chile from December to January as well as in the North-Eastern Pacific and Atlantic west of the coasts of California and North-Africa from June to August. These regions are part of the Subtropical Anticyclones, which have their descent branches in the east, with air masses subsiding and flowing equatorwards from there. These dry zones are decreasing over the 150 years of the model run, as the UTH is increasing.

In the Pacific Ocean different structures appear in Figure 5.6. Beneath the drying on the edges of the primary dry zones (from the first decade) and the change in UTH of the Subtropical Anticyclones subsidence zones, regions with increase of UTH are located around the geographic Equator in both seasons. In boreal winter (DJF) the upper troposphere above the Pacific is drying around 25°N and around 25°S in the east. Another region with decreasing UTH in the Pacific in summer can be found around Central-America. From June to August the North-Western Pacific presents mostly a moistening trend, whereas the South-Eastern Pacific especially in the surroundings of South-Australia have decreasing UTH.

As these different patterns and magnitudes of UTH do apparently not have their origin in one and the same mechanism, the following Sections will analyse these different phenomena separately. The first Section (5.2.1) will focus on the subsidence zones from the Hadley Cell, following the assumption of recent research about the poleward expansion of the dry zones. The Subtropical Anticyclones will be analysed in the Section 5.2.3. Finally, Section 5.2.4 examines the different UTH structures in the Pacific regions.

5.2.2 The Dry Belt in the MPI-ESM-MR 1pctCO2 Run

In the seasonal and zonal mean, the meridional atmospheric circulation consists in uprising air masses in the ITCZ and subsiding air masses in the subtropics. The subsidence regions are discernible through the small UTH values as seen in Figure 5.1 and 5.6. But as the ITCZ is seasonally varying, the location of the ascent and descent regions is dependant on the seasons. In general from December to February and from June to August the ascent region lies in the outer tropics of the summer hemisphere and the descent region in the outer tropics of the winter hemisphere (Dima and Wallace, 2003). This explains why only one dry belt per season is visible in Figure 5.6, located on the Northern Hemisphere in boreal winter (DJF) and on the Southern Hemisphere in austral winter (JJA).

In Figure 5.6 for December to February UTH is decreasing in the 150 years of the model run at the northern edges of the dry zones averaged over the first decade.

This is visible over North Africa, the Arabian Peninsula as well as over most of the North Pacific Ocean. Over the Atlantic Ocean, the dry zone in the northern subtropics is visibly widening in the course of the model run.

From June to August the drying at the edge of the winter hemisphere is not as clear as in boreal winter, only around Australia and in the South-Eastern Pacific is the drying trend at the edge of the subsidence zones recognizable.

Drying on the Edge of the Subsidence Regions

The poleward expansion of the Hadley Cells due to global warming prognosticated by the climate models (Lu et al., 2007, e.g.) and already reported by first observation studies (Hu and Fu, 2007, e.g.) lead to a shifting of the edges of the subtropical subsidence zones and hence of the subtropical dry zones towards the poles. This shifting can be seen in the MPI-ESM-MR model run with gradually increasing CO₂ concentration (Figure 5.7).

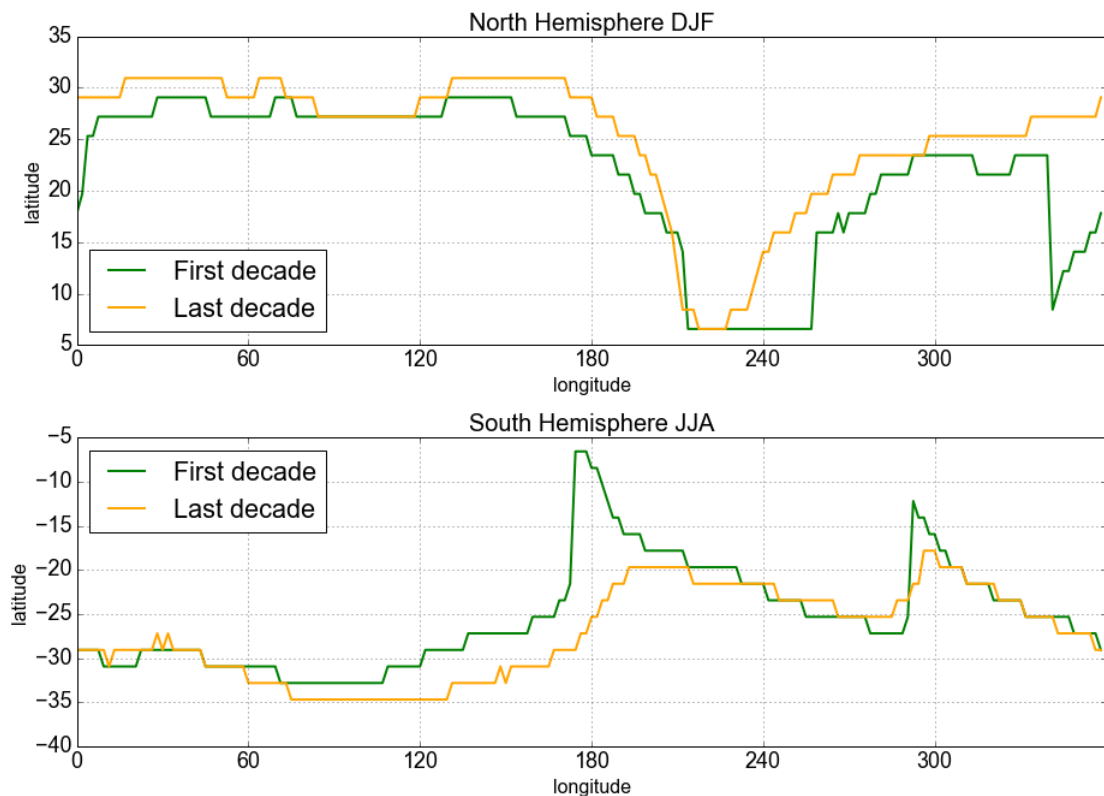


Figure 5.7: Northern (top) (Southern (bottom)) edge of drybelt for December, January and February (June, July and August) for the first (green) and the last decade (yellow) of the MPI-ESM-MR 1pctCO₂ model run.

In the upper graph of Figure 5.7 the blue line indicates the northernmost latitude of the region with UTH smaller than 40 % RH in average over the northern winter

in the first model decade. The red line of the same graph shows the same for the last decade of the model run. In the Northern Hemisphere the red line lies almost everywhere above the blue one, which indicates that the poleward edge of the dry belt shifts towards the poles. In the Southern Hemisphere, the red line, indicating this time the southernmost latitude with UTH smaller than 40 % RH, lies south of the blue line for the most part of the graph. But the poleward expansion is not as clear as in the Northern Hemisphere.

If we consider only the difference between the latitudes of the edges of the dry zones of the last decade and the first decade of the model run (Figure 5.8), this difference is mostly positive for all longitudes, except for the southern dry zone over South-East Africa and in the South-East Pacific. Here the difference shows a slightly northern shift of the dry zone edge. The peaks in Figure 5.8 should not be overweighted. They appear because of the chosen threshold of 40 % RH for the UTH of the dry zones. In the regions around those peaks, the upper troposphere was already dry in the first decade, without reaching the threshold. In the last decade, the mean UTH lies under 40 % RH and so the whole region now lies inside the drybelt and produces an abrupt shift in the so defined dry zone edge.

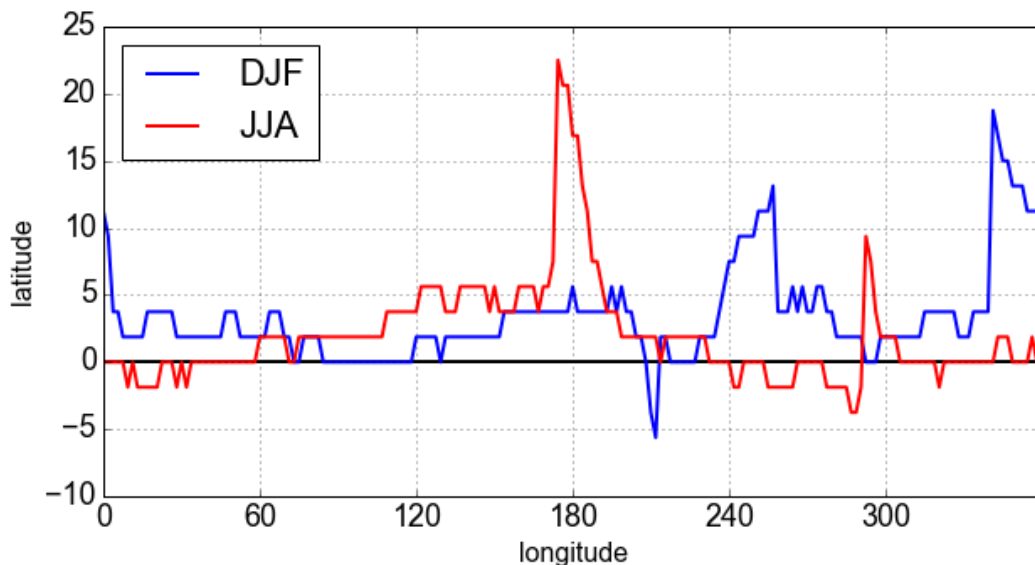


Figure 5.8: Difference of the latitudes of the Northern (DJF) (Southern (JJA)) edge of the drybelt between the last and the first decade of the MPI-ESM-MR 1pctCO2 model run.

In the Northern Hemisphere winter, the mean poleward shift of the dry zone between the first and the last decade of the model run amounts to 3.3° in latitudes. Again, the peaks already mentioned in Figure 5.8 might distort this calculation. By excluding the peak zones from the calculations, the mean northward shift of the dry belt represents 2.4° in latitude for longitudes between 0° and 206° , and 2.9° from

260° to 340° in longitude (Table 5.1). In the Southern Hemisphere the dry belt shifts in average by 2.0° to the South. Excluding the peak around 180°, the mean poleward shift represents 2.0° west of the peak from 0° to 168° and 0.4° east of the peak from 199° to 360°. These results are smaller than the spread of 2° to 5° of Hadley Cell widening found in observations since 1979 (Hu and Fu, 2007; Seidel et al., 2008; Johanson and Fu, 2009).

Table 5.1: Poleward shift of the edge of the subtropical dry zones between the first and the last decade of 1pctCO2 model run.

Hemisphere(season)	Mean shift [$^{\circ}Lat$]	Shift West [$^{\circ}Lat$] ¹	Shift East [$^{\circ}Lat$] ²
North (DJF)	3.3	2.4	2.9
South (JJA)	2.0	2.0	0.4

¹ Excluding peaks. For NH: 0-206° *Lon*, for SH: 0-168° *Lon*

² Excluding peaks. For NH: 260-340° *Lon*, for SH: 199-360° *Lon*

But even though the subsidence zones nearly form a dry belt in the winter hemisphere, this belt is not uniform over the planet. The drying trend due to increased CO₂ is varying depending on the dry region. Not everywhere do these dry zones expand polewards. The region encompassing Central America and the Caribbean are located in the subsidence zone. Here, UTH decreases consistently, but is this due to the poleward extension of the Hadley Cell?

Expanding Winter Dry Zone in the Caribbean and Central America

Central America and the Caribbean are situated in the subtropics and the climate of the region is regulated to a large extent by the subtropical high of the North Atlantic. During boreal winter subsidence dominates while the subtropical high from the North Atlantic is spreading to the North American landmass (Taylor and Alfaro, 2005). This fact associated with a strong trade inversion and a colder ocean reduce atmospheric humidity and contributes to the generally dry climate of the region. This is valid for the upper troposphere, as can be seen in Figure 5.6 for the first decade in DJF.

As such, the descent region over Central America and the Caribbean in boreal winter is also an example of a dry region in the winter hemisphere, which shows the expected tendency to expand poleward under global warming, but it also shows an interesting general drying trend (Figure 5.2). The Caribbean dry zone widens in all directions and deepens considerably over the 150 years of the run.

Figure 5.9 shows the decadal means of UTH in Central America and the Caribbean

for boreal winter. Between 20°W to 120°W and 5°N to 25°N the small regions with UTH smaller than 30 % RH at the beginning, grows and deepens with parts where UTH is even smaller than 20 % RH. The dry zone, which before was concentrated over the ocean, stretches also over parts of the American continent after the 150 years of the run.

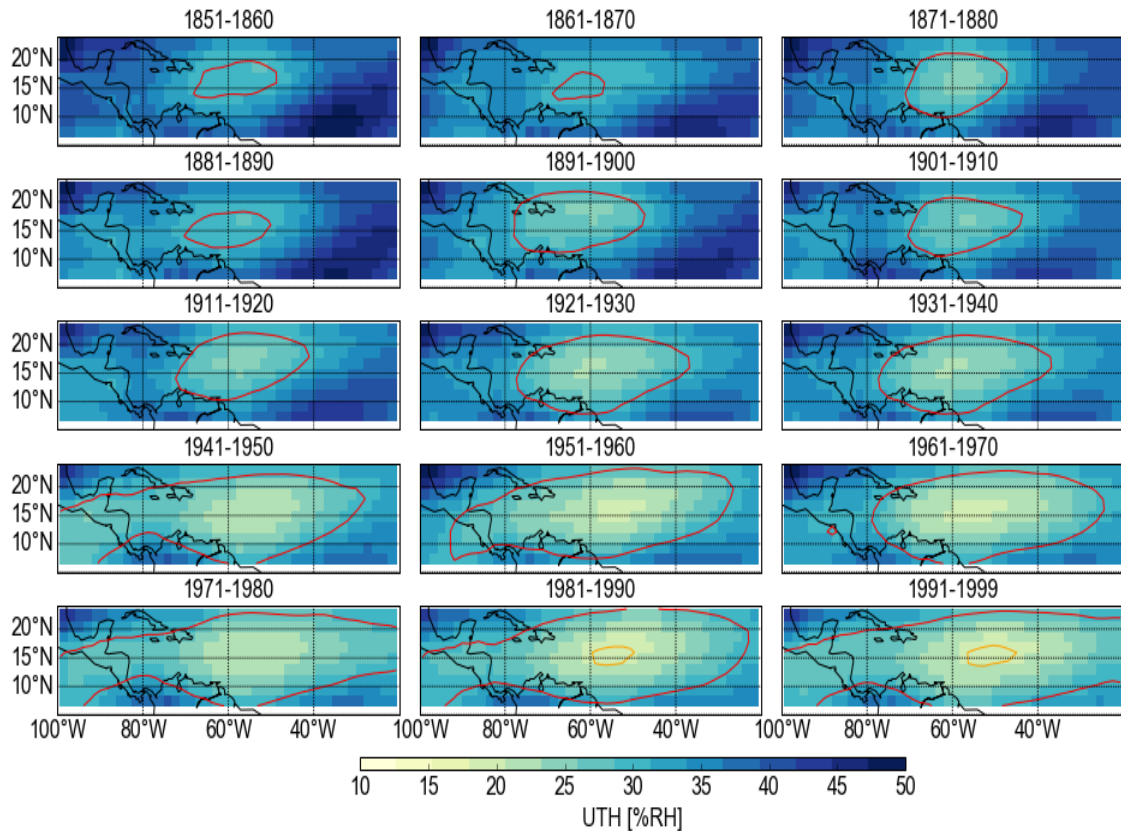


Figure 5.9: Decadal mean of UTH for the 15 decades of the 1pctCO2 run of MPI-ESM-MR model for the region of the Caribbean and Central America in winter (December to February).

We introduced before the frequency of occurrence of UTH smaller than 30 % RH (UTHp30). In this region the evolution of UTHp30 is particularly clear, with only a small occurrence of UTHp30 in the first decades and a gradually increase of dryness with an occurrence of UTHp30 of nearly 100 % RH in the last decades for important parts of the region (Figure 5.10). The driest part of the region is located over the ocean, but while in central America and on the coast of northern South America UTH rarely drops under 30 % RH in the first decade, the frequency of occurrence of very dry events increases during the model run and even parts of the upper troposphere over the continent show UTHp30 of over 60 % RH.

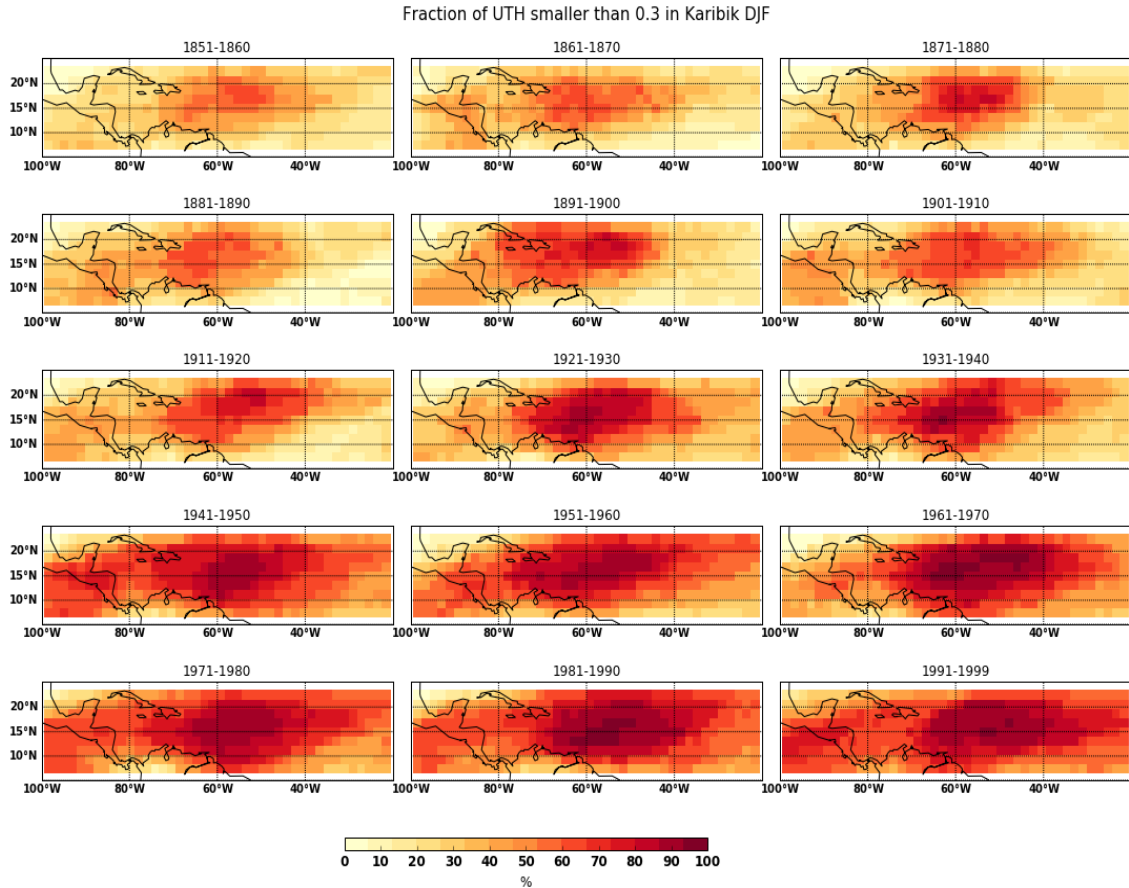


Figure 5.10: Decadal mean of the frequency of occurrence of UTH smaller than 30 % RH for the 15 decades of the 1pctCO₂ run of MPI-ESM-MR model for the region of the Caribbean and Central America in winter (December to February).

But against the hypothesis that the dry zones in the subsidence regions expand mainly poleward due to the expansion of the Hadley Cell, this region does show an overall drying trend with decreasing UTH in all directions around the primary dry region. The reasons for this particular drying can be manifold and this study has not the aim to explain this drying trend conclusively. But it is at least possible to link the drying trend to the dynamical circulation through the vertical velocity. Figure 5.11 shows, that the vertical velocity in this region is also changing during the 150 years of the model run. Especially the South-East of the region, where UTH is much higher at the beginning of the run, presents uprising motions in the first decades (negative vertical velocity) and shifts to mean descending motions (positive vertical velocity) in the last decades. Therefore, part of the decrease in UTH can be a consequence of enhanced subsidence in this region.

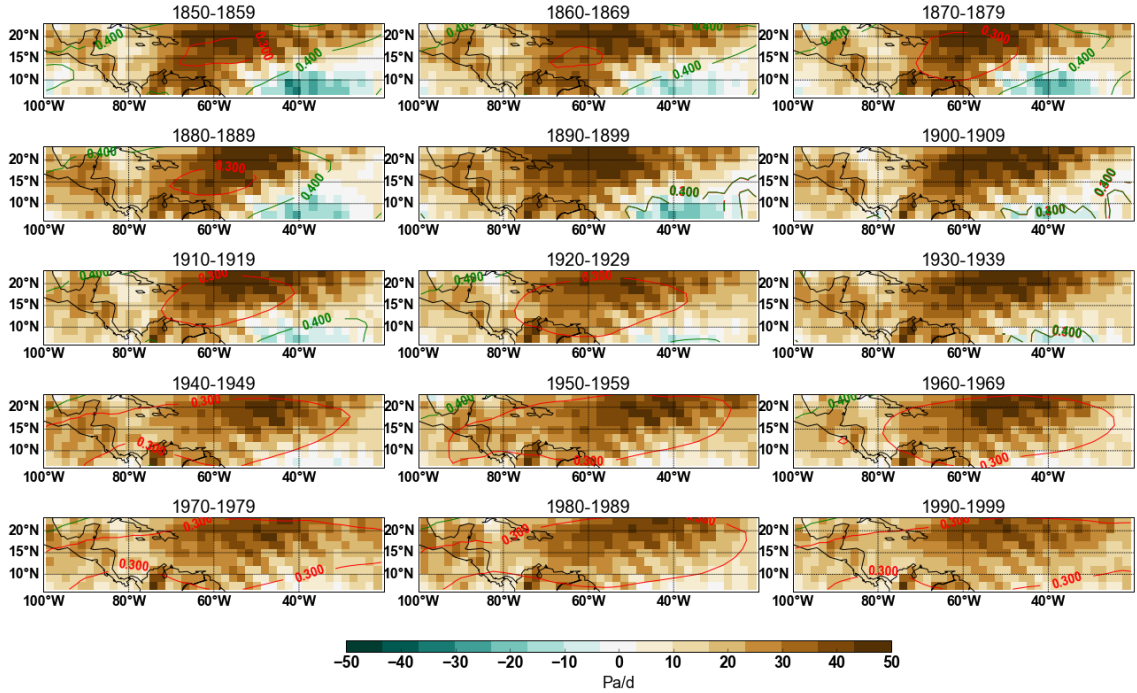


Figure 5.11: Decadal mean of the vertical velocity for the 15 decades of the 1pctCO2 run of MPI-ESM-MR model for the region of the Caribbean and Central America in winter (December to February). The contour lines show zones of UTH below 30 % RH (red) and 40 % RH (green).

Jury and Winter (2009) showed with observation data of the 20th century, that there is in fact a trend toward faster sinking motions over the Caribbean, which induces a fast rate of warming and drying especially in the trade wind inversion. Compression caused by sinking motion in the Hadley circulation has already driven up air temperatures over the Caribbean whereas the Amazon monsoon has become more vigorous (Jury and Winter, 2009).

It is unclear to what extent the drying trend can be linked to changes in vertical velocity. But before going further into the details of this question, it is preferable to have a look at other models, to see if this result is robust or specific to the MPI-ESM-MR model (Section 5.4).

In accordance with recent studies about poleward expansion of the Hadley Cells, the present thesis found a drying trend at the edges of the subtropical subsidence zones in the winter hemispheres. This was the part of the analysis which was expected. Another category of dry zone will be analysed in the next Section, which has not been found in many previous studies of upper tropospheric moisture yet: the regions of the Subtropical Anticyclones.

5.2.3 Moistening Trend in the Descent Zones of the Subtropical Anticyclones

Beside the dry belts in the subsidence zone of the winter-hemispheres, the global view of UTH in DJF and JJA manifests also some smaller but still prominent dry regions in the summer hemispheres. They are located in the East of each ocean basins around 25°N in JJA and 25°S in DJF and lie mostly over the ocean, only slightly crossing the continental coast (Figure 5.6).

The Subtropical Anticyclones

Until recently, meteorologists have thought the Hadley Circulation to be responsible for dry subsidence zones in the subtropics in all seasons. But the descent branch of the Hadley Cell is mostly concentrated in the winter hemisphere. The dry regions in the eastern ocean basins of the summer hemispheres (Figure 5.6) could however been related to the Subtropical Anticyclones. These atmospheric structures connect the tropical trade wind regime with the mid-latitude westerly belt in the near-surface flow and have been found to strongly influence moisture transport (Li et al., 2012). The mechanisms that underlay the development of Subtropical Anticyclones are still in dispute (Seager et al., 2003). But it is known, that in summer these structures of the general circulation extend over the summer-hemisphere oceans and feature strong meridional equatorward flow on their eastern flanks, accompanied by strong subsidence (Seager et al., 2003). On the western flank the flow is more diffuse and therefore presents only weak ascent, which would explain, why there is no clear region of high UTH in the western counterpart basins of the summer hemisphere oceans in Figure 5.6.

Rodwell and Hoskins (2001) demonstrated that the anticyclones and the descent as part of them are driven by the summer monsoons and influenced by the surrounding mountains. The subtropical descent is induced by the North American monsoon over the eastern North Pacific in summer, by the South American monsoon over the eastern South Pacific, and by the Asian monsoon over the eastern North Atlantic (Rodwell and Hoskins, 2001). Seager et al. (2003) also completed the study of Rodwell and Hoskins (2001) by arguing, that the Subtropical Anticyclones would be much weaker without taking into account the air-sea interaction. Once they have been forced by monsoon heating over land, subsidence of dry air over the eastern subtropical oceans lowers the sea-surface temperature (SST) and thus stabilizes the atmosphere, while higher SST in the western subtropical oceans destabilise the atmosphere. The descent in the east is hence further enhanced by radiative cooling and is associated with equatorward surface winds parallel to the western coasts, which induce oceanic upwelling of cold water and result in sea-surface cold pool, which

may feed back on the anticyclone by further suppressing convection and inducing descent (Rodwell and Hoskins, 2001).

The interesting question arising is then, if the evolution of UTH in these regions can be explained by a change in the Subtropical Anticyclones due to increasing greenhouse gases in the atmosphere? The following Section will try to answer this question by focussing on these specific subtropical dry zones.

Evidences of Weakened Dry Zones in the Subtropics

Five regions of low UTH located on the eastern flanks of Subtropical Anticyclones can be found in the summer hemispheres in Figure 5.6. From December to February, dry regions are situated in the eastern basins of the southern Indian Ocean west from Australia as well as of the South-East Atlantic and the South-East Pacific Ocean. From June to August the dry zones possibly related to the Subtropical Anticyclones are located in the North-Eastern Atlantic (around the Azores) and in the North-Eastern Pacific, west of the coast of California.

The five regions in concern do all have a positive trend in UTH in the 150 years of the model run. But the magnitude of change is different depending on the region. In the dry zones of the subtropical North Atlantic Ocean and in the South East Indian Ocean, UTH is only slightly increasing (Figure 5.12, 5.13). The dry zone in the subtropical South Pacific Ocean is hardly not changing at all (Figure 5.6). In the South Atlantic the summer dry region is clearly becoming moister (not shown here but visible in Figure 5.6). But most of all, it is the dry zone near the Northern Pacific Subtropical Anticyclone that is decreasing considerably (Figure 5.14 and Figure 5.15).

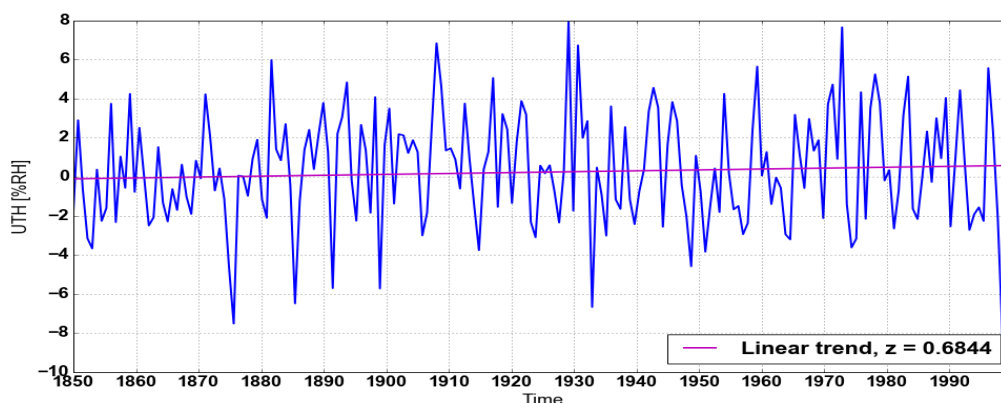


Figure 5.12: Trend of UTH for the 150 years of 1pctCO2 run of MPI-ESM-MR model for the region around the Azores in summer (June to August).

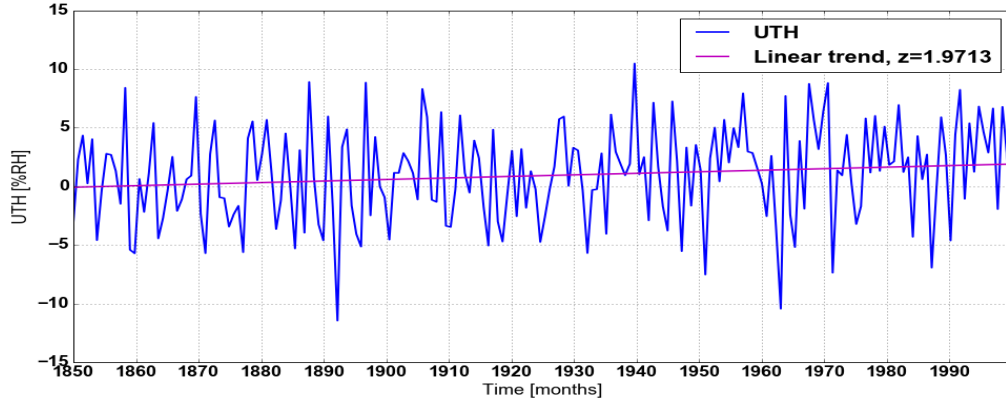


Figure 5.13: Timeseries of UTH for the 150 years of the 1pctCO2 run of MPI-ESM-MR model for the region of the South-East Indian Ocean west from Australia in summer (December to February).

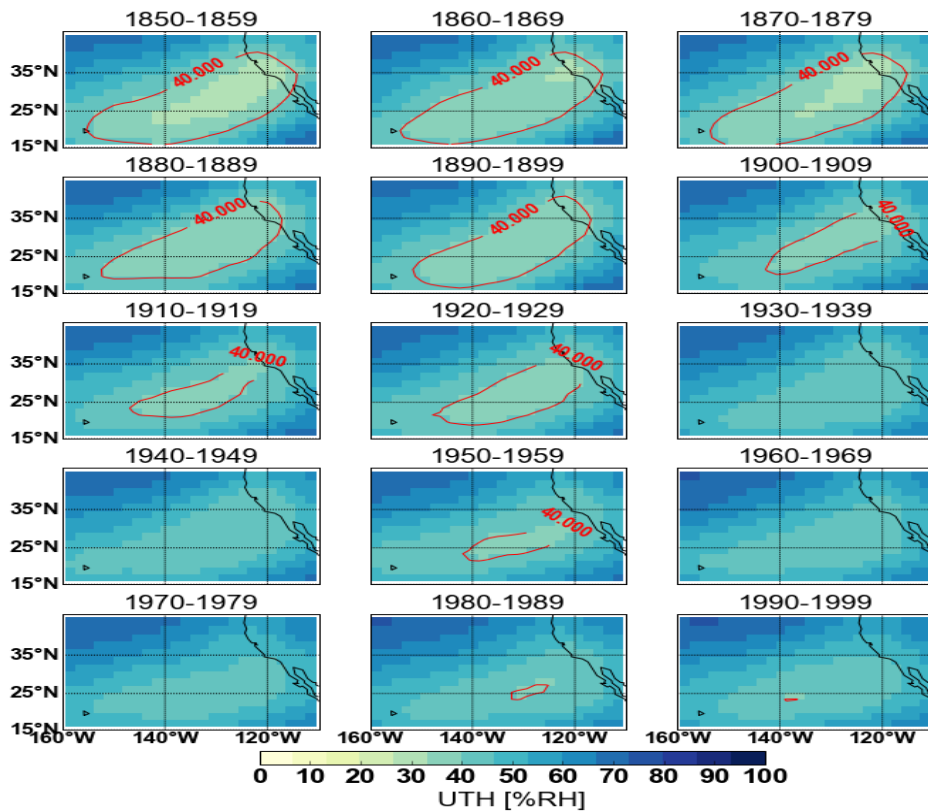


Figure 5.14: 15 decades of UTH of MPI-ESM-MR 1pctCO2 simulation for the North Pacific High in summer (June to August).

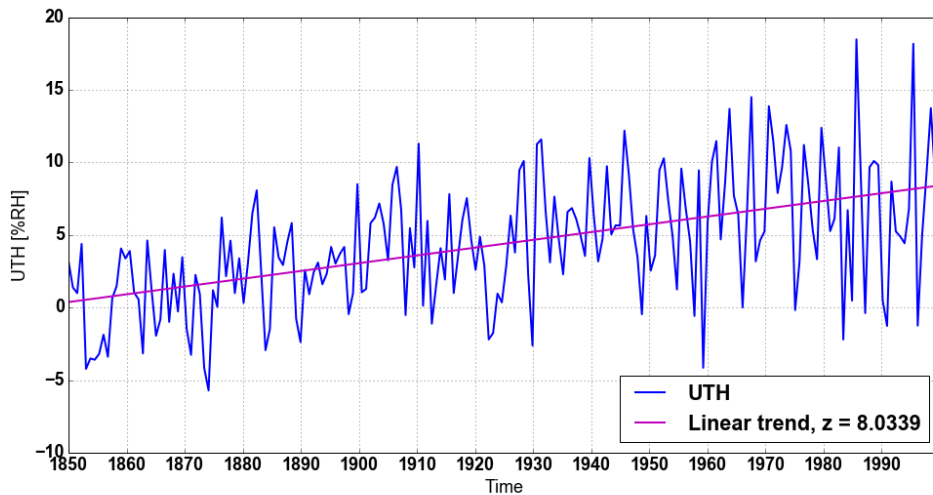


Figure 5.15: Timeseries of UTH in the North Pacific High during the 150 years of MPI-ESM-MR 1pctCO2 model simulation in summer (JJA).

There has been few studies about UTH in these regions and as the anticyclones have been (traditionally) measured with sea level pressure, most of the relevant studies are focussing on the lower troposphere (e.g. [Davis et al., 1996](#); [Li et al., 2012, 2013](#)). Besides, not all the five regions have been equally relevant for human society and so not all of the Subtropical Anticyclones have been studied with the same intensity. For historical reasons, the Subtropical Anticyclones which have been studied most are the one in the North Atlantic Ocean, also called the 'Azores High', and the North Pacific High.

Considering the dry region in the subtropical North Atlantic basin, [Davis et al. \(1996\)](#) employed gridded sea level pressure data from the National Center for Atmospheric Research (NCAR) from 1890 to 1990, in order to analyse seasonality and inter-annual evolution of the North Atlantic Subtropical Anticyclones, and localised it via the mean frequencies of high pressure (pressures higher or equal to 1020 hPa). The Azores High has its centre at 30°N, 40°W in July and hence lies just in the west of the dry zone found in the North Atlantic Ocean and it seems likely, that there is a correspondence between the two structures, even though the pressure was measured at sea level and not in the upper troposphere.

[Davis et al. \(1996\)](#) found that the frequency and intensity of the Azores High has declined significantly over the 20th century. This could be responsible for the decrease in subsidence in its eastern part. This change in turn could lead to less drying in the upper troposphere and would explain, why UTH increases in these regions in a climate with increasing greenhouse gases.

But more recently [Li et al. \(2012, 2013\)](#) found an intensification of the Northern and Southern Hemisphere subtropical highs in reanalysis data (ERA-40) from Eu-

ropean Centre for Medium-Range Weather Forecasts (ECMWF) and in the model data from the Coupled Model Intercomparison Project phase 3 (CMIP3). This would contradict the hypothesis, that the increase in UTH in the MPI-ESM-MR 1pctCO2 model run in these regions can be explained by a decline of the Subtropical Anticyclones.

The North Pacific High has been subject to more research than the other ones (e.g. [Nigam and Chan, 2008](#); [Shaffrey et al., 2002](#); [Rodwell and Hoskins, 2001](#)), especially because of its prominence in the North Pacific Ocean during summer. In Figure 5.14, the eastern flank of the location of the North Pacific High is characterised by decreasing dryness in the 150 years of the model run. The extent is not changing considerably but the intensity of the dry zone is decreasing. The time series of UTH in summer (Figure 5.15) shows an increasing trend of nearly 8 % RH over the 150 years. Comparing these results with the vertical velocity (Figure 5.17), UTH can at least partly be explained by a decrease in subsidence motions. In most of the region where UTH is increasing west of the North American coast, subsidence is also decreasing in the same time. But if the Subtropical Anticyclones are intensifying with climate warming ([Li et al., 2012](#)), what could explain this change in subsidence and hence in upper tropospheric moisture?

It is beyond the scope of this work to investigate in detail the possible explanations of the change in UTH in this region, but other scientist have studied the relationship between the Subtropical Anticyclones, the monsoons, the sea-surface temperature (SST) and the orography in the east ([Rodwell and Hoskins, 2001](#); [Shaffrey et al., 2002](#)). [Shaffrey et al. \(2002\)](#) used model data from HadAM3 and increased the albedo of North America in order to decrease the surface temperature and weaken the land/ocean contrast responsible for the North American Monsoon. The consequence is a weakened ascent over the North American monsoon region, while the descent in the eastern flank of the North Pacific High to the north-west of the monsoon region, also weakens to a similar extent. The same effect is demonstrated by the second part of the experiment by [Shaffrey et al. \(2002\)](#), which consists in decreasing the height of the Rocky Mountains, leading to less of the mid-latitude westerlies being deflected southwards and descending. This results in anomalous ascent in the eastern flank of the Subtropical Anticyclones. [Shaffrey et al. \(2002\)](#) concluded that the heating in the North American monsoon induce descent to the north-west of the monsoon in the descending eastern flank of the Subtropical Anticyclones and is therefore an important stimulus for this anticyclone.

In the study by [Rodwell and Hoskins \(2001\)](#), local cooling from the North Pacific also has important influence on the magnitude of the subtropical high. A SST increase could therefore also be at the origin of the weakening of subsidence. Finally, [Nigam and Chan \(2008\)](#) also found to a smaller extent the North-West Pacific

monsoon to be the origin of descending air in the eastern North Pacific.

Considering these results, the change in UTH with increasing CO₂ in MPI-ESM-MR could therefore be related more to a change in the monsoon circulations than to a direct influence of the Subtropical Anticyclones. A weakening of the monsoon from June to August, consistent with actual studies (Cook and Seager, 2013), implies a weakening of ascent and descent and therefore could be responsible for increased UTH in the eastern North Pacific Ocean.

Some years earlier, Rodwell and Hoskins (2001) already showed that the equatorward portion of the Subtropical Anticyclones may be viewed as the Kelvin wave response to the monsoon heating over the continent to the west, and that the Rossby wave response to the west of subtropical monsoon heating, interacting with the mid-latitude westerlies, produces a region of adiabatic descent. Rodwell and Hoskins (2001) see the monsoons as being generally the origin of air masses which are descending in these regions, and therefore of the dry troposphere on the eastern flanks of the Subtropical Anticyclones, not only in the North Pacific. A reason for the difference in magnitude of the change in UTH in these regions could then be a different magnitude in the change of the related monsoon circulations.

Shaffrey et al. (2002) also reveals the mountain ranges in the east to be partly responsible of the descent motion. The change in UTH with increasing greenhouse gases in these regions then also depends on the importance of the influence of the monsoons compared to the influence of the topography. The influence of the South American Andes on the subtropical subsidence is possibly greater than the influence of the South American monsoon, compared to for example the influence of the African or Australian topography on the North Atlantic and South East Indian anticyclone respectively. As the topography is not changed by the increase of greenhouse gases, the subsidence zone in the subtropical South Pacific changes less compared to the other regions of subtropical descent.

From June to August, besides the two dry zones on the eastern flanks of the subtropical summer anticyclones in the North Pacific and North Atlantic Oceans, Figure 5.6 shows a third dry region in the upper troposphere above the Eastern Mediterranean and the Middle East. Despite the fact that this dry zone is not located above the oceans, it presents the same weakening characteristics as the former two. Rodwell and Hoskins (1996) linked the Asian monsoon to these descent regions in the north-west. The so called monsoon-desert mechanism forces air masses of the summer divergent outflow from the Bay of Bengal to descend over western Afghanistan and eastern Iran as first descent region and over the eastern Mediterranean as second descent region. This corresponds well to the structures of vertical velocity and of UTH found in Figures 5.17 and 5.6, and it is likely that these structures of dry air in the upper troposphere are related to the same mechanism as those

near the Subtropical Anticyclones.

To summarize this Section, time series of mean UTH and vertical velocity have been analysed for the descent regions of the four main Subtropical Anticyclones in the North Pacific, the North Atlantic, the South Pacific and the South Indian Oceans in summer season (Figure 5.16). UTH is mostly increasing in these regions, except for the region in the South-East Pacific Ocean, where UTH shows a slightly decreasing trend. In the same time, vertical velocity (ω) is decreasing in all four regions. The trends are small for all regions except for the North Pacific High, where UTH is increasing clearly (+6.9 % RH) and ω is decreasing by -8.6 hPa/day. Finally, UTH and ω are anti-correlated in all of the four descent regions, but the anti-correlation is the highest in the Subtropical Anticyclones of the South Indian Ocean.

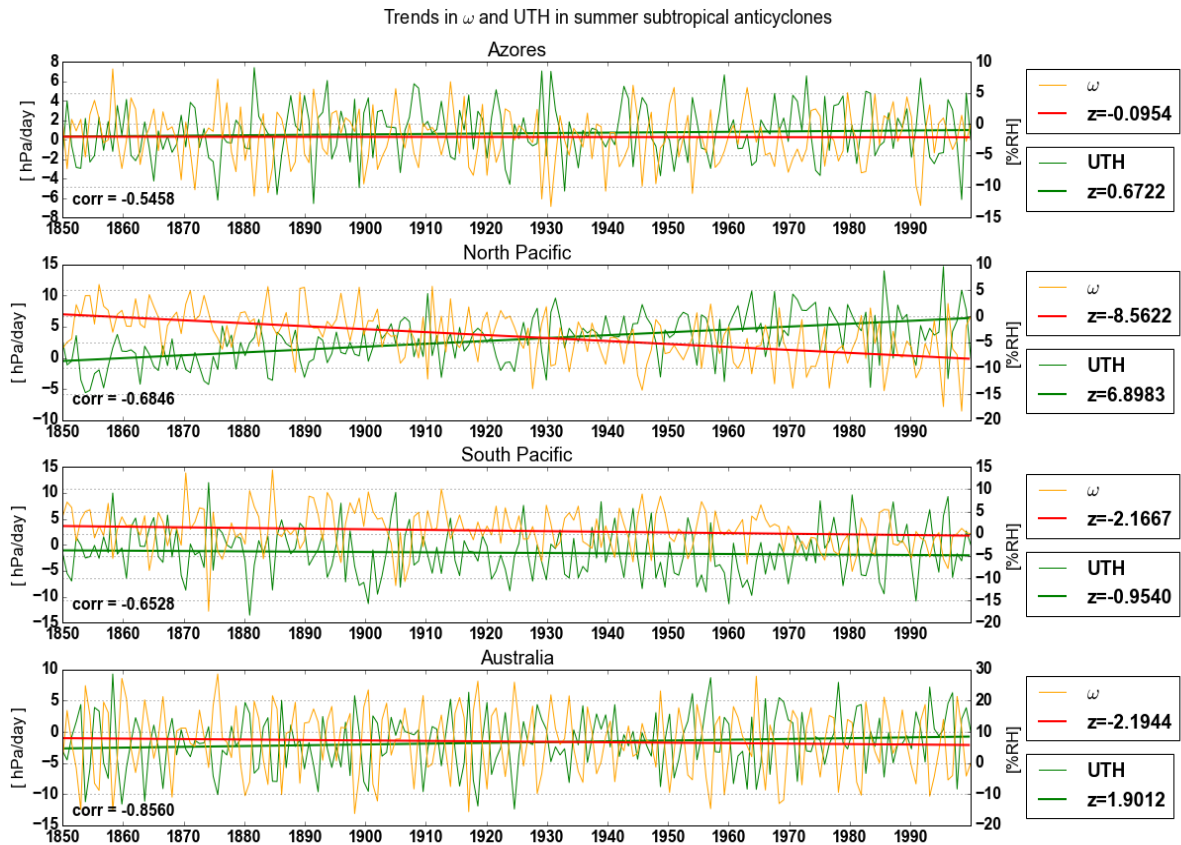


Figure 5.16: Timeseries of vertical velocity and UTH for the 150 years of the 1pctCO2 run of MPI-ESM-MR model for the descent regions of the Subtropical Anticyclones in the North Pacific and the North Atlantic from December to February, the South Pacific and the South Indian Oceans from June to August. In the legend, z indicates the linear trend. Each time series is completed by the correlation between UTH and the vertical velocity.

In this paragraph we have focused on the regions with lower UTH in the subtrop-

ical summer hemispheres. These are located in the upper troposphere above every ocean in summer as well as over the Eastern Mediterranean and the Middle East, and show a general tendency of getting moister in the 1pctCO₂ experiment. As the locations of these upper tropospheric dry zones correspond to the descent regions of the lower tropospheric Subtropical Anticyclones, it is likely, that both structures are related. The reasons for the upper tropospheric moistening may hence be found in the mechanisms influencing the Subtropical Anticyclones, like for instance the strength of the monsoon circulations. But this hypothesis still needs to be verified.

Even though the upper troposphere above the Pacific Ocean does include both of the structures seen afore, the subsidence zones in the winter hemisphere and the subtropical descent regions in the summer hemisphere, it is worth to focus at last on the evolution of all the upper tropospheric dry zones in the Pacific sector.

5.2.4 The Pacific Dry Zones: the Hadley and Walker Circulations

The large dry zones identified in Figure 5.1 could be assigned to two groups of structures and to two ways of evolution with increasing CO₂ concentration. For a major part of the world, upper tropospheric dry zones change due to the poleward expansion of the Hadley Cell and because of the change in descent motions on the eastern flanks of the summer Subtropical Anticyclones. But above the Pacific Ocean, these structures are more complex.

In boreal winter (DJF), UTH distribution above the Pacific Ocean as seen in Figure 5.1 presents dominant dry zones in the tropics over all the width of the ocean basin. In the western Pacific, between 120°E and 180°E, this dry zone is located mainly north of the Equator between the latitudes 5°N and 25°N. In the centre and in the west Pacific, the driest region can be found exactly around the Equator. A secondary region with small UTH values is the whole south-east tropical and subtropical Pacific between 120°W and the western coast of South America. This last region shows a centre with increased dryness in the south-east, just where the eastern flank of the Subtropical Anticyclones can be located in the South Pacific.

From June to August the main dry belt shifts to the Southern Hemisphere and lies between 5°N and 25°S, becoming narrower from east to west. The western part of the equatorial Pacific, between the Maritime continent and 160°E presents a gap in the dry belt with UTH being higher than in the rest of the belt. The secondary dry region in boreal summer in the eastern North Pacific has already been analysed in the Section before as part of the North Pacific High.

These structures of UTH reflect the circulation pattern, which consists in the meridional component, already introduced as the Hadley circulation, and in a zonal

component, the Walker circulation. The Walker circulation, named after Sir Gilbert Walker, refers to the totality of the east-west atmospheric circulation along the Equator and consists in six different cells, but the most prominent is the one originally referred to as the Walker circulation, in the Pacific ocean (Lau and Yang, 2002). This circulation consists in low-level winds blowing from east to west across the Pacific, rising motion over the warmer waters in the western tropical Pacific and a returning flow from west to east in the upper troposphere. The circulation is closed by sinking motion over the cold water of the Humboldt stream near the coast of South America (Bjerknes, 1969).

At the end of the MPI-ESM-MR model run with gradually increased CO₂ concentration (1pctCO2) UTH changes in the tropics. In both seasons, a moistening of the upper troposphere can be seen in a narrow band around the Equator. Previous studies (e.g. Vecchi and Soden, 2007; Su et al., 2014) demonstrated that the strength of the atmospheric overturning circulation decreases as the climate warms, while in the same time zonal mean large-scale rising motions strengthens within the ascending branch of the Hadley Cell near the Equator between 5°S and 5°N, suggesting a narrowing of the tropical ascending zone. This evolution of the meridional circulation could be the reason for the increase in UTH in the tropical Pacific in Figure 5.6.

But beside the moistening around the Equator it is also possible to see a shift in the convection region at the end of the 150 years, with higher UTH values shifting eastward and the former moist region of Indonesia becoming drier. This eastward drift of the convection is especially clear from December to February, but it is also visible in boreal summer and confirms previous studies for example of Vecchi and Soden (2007).

Following the approach of Vecchi and Soden (2007) we consider the change in upward pressure velocity to investigate the origin of the changes in the dry zones in the Pacific region. Figure 5.17 shows the decadal mean of vertical velocity in the first and in the last ten years of the MPI-ESM-MR 1pctCO2 model run for boreal winter (DJF) and summer (JJA). The green contour line indicates the edge of the region with UTH smaller than 40 % RH in the first decade (1850-1859). From December to February the most prominent feature is the region of upward motion in the west tropical Pacific Ocean, which corresponds well to the convection zone of the Walker circulation, where the UTH distribution presents also a maximum. An eastward shift of this convection region can be noted in the vertical velocity likewise to the UTH distribution between the first and the last decade of the model run. Vertical velocity decrease over the Maritime Continent in the tropical West Pacific and increases in the east of this primarily convection region. Vertical velocity also decreases in the core of the ITCZ, south of the Equator in DJF and north of the Equator in JJA,

accounting for a strengthening of the rising motion as part of the Hadley circulation.

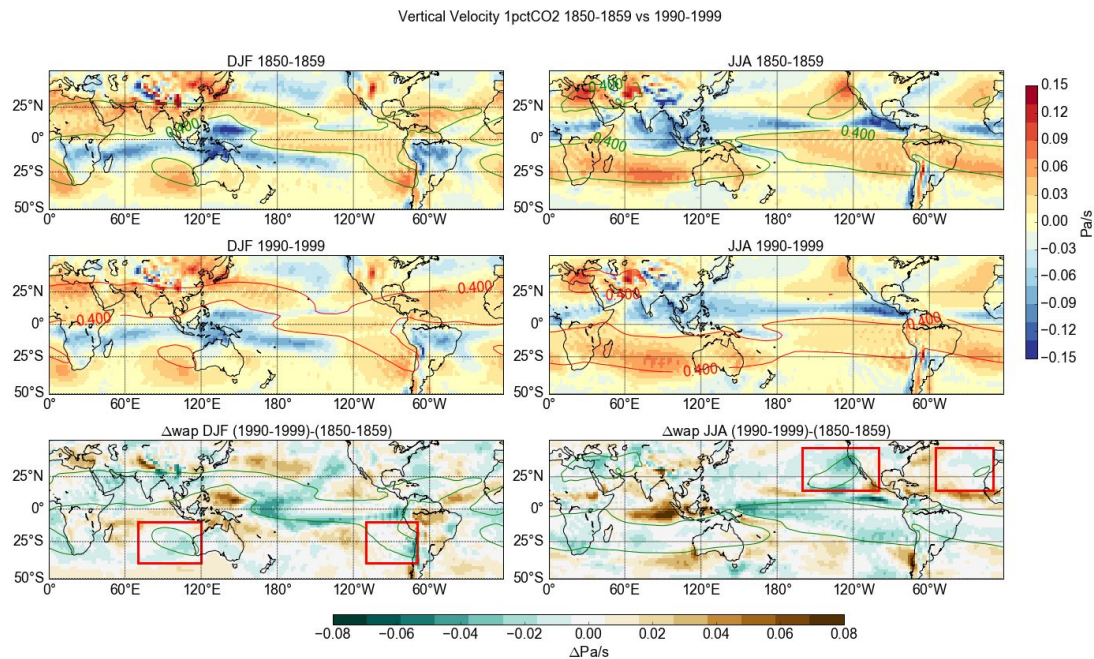


Figure 5.17: Decadal mean of vertical velocity for the first and the last decade of the MPI-ESM-MR 1pctCO₂ model run and their difference for DJF and JJA.

Figure 5.17 can be used to finally summarize all dry zones studied before and evaluate the influence of vertical velocity on UTH's evolution in the dry zones. Besides the afore mentioned Walker circulation, the subsidence regions of the Subtropical Anticyclones are visible and have been marked with red boxes. In these four regions, where UTH is increasing in the course of the 150 model years, vertical velocity is decreasing, possibly an indication for a weakening of the Subtropical Anticyclones in 1pctCO₂. As Figure 5.17 also shows a decrease in up-rise motion over the North-East Indian and the tropical Atlantic Oceans in JJA, the weakening of the Subtropical Anticyclones could be a consequence of monsoon circulation's weakening, but this needs to be further investigated. In general, the evolution of vertical velocity is positive, where UTH is decreasing and negative where UTH is increasing.

This is confirmed by the correlation between UTH and the vertical velocity on the level of 500 hPa represented in Figure 5.18 for the first and the last decade of the 1pctCO₂ run, separated for DJF and JJA. At the model run's beginning, upper tropospheric moisture and the vertical velocity are generally anti-correlated in the tropics, as negative values of vertical velocity (rising motion) lead to higher UTH values (convection regions), while descending motions lead to atmospheric drying. In the dry zones vertical velocity is therefore expected to be positive. In the dry

regions of central and eastern equatorial Pacific Ocean in DJF, as well as in the central and South-Eastern Pacific Oceans in JJA, UTH and vertical velocity are low anti-correlated or unexpectedly correlated. In the frame of the present study it has not been possible to find an explanation for this correlation in the dry zones, the more so as the plots of vertical velocity and UTH do not show this disparities (Figures 5.6 and 5.17). The regions with low anti-correlation or even correlation have all low significance (indicated by black crosses). Further investigations are needed to find a concluding explanation for this model data behaviour.

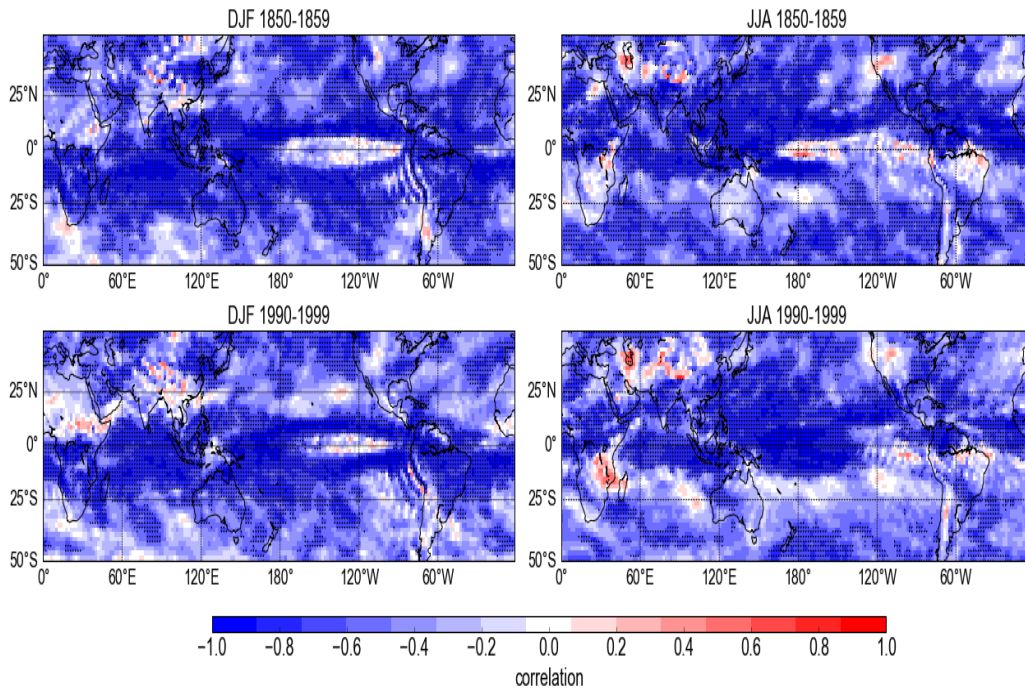


Figure 5.18: Correlation between the decadal mean of vertical velocity and of UTH for the first and the last decade of the MPI-ESM-MR 1pctCO2 model run for DJF and JJA.

5.3 Evolution of UTH and the Dry Zones in the abrupt4xCO2 Experiment

It is widely accepted, that increasing greenhouse gases lead to atmospheric warming, even though there remains uncertainty on the magnitude of this temperature response. An important number of climatic responses are then tightly coupled to the temperature response (Held and Soden, 2006). What is less well known is, that CO₂ also impacts the atmosphere directly, independently of surface temperature changes (Bony et al., 2013). Lu et al. (2009) found that the tropical belt's widening trend can be attributed entirely to direct radiative forcings, in particular those related to

greenhouse gases and stratospheric ozone depletion, while the sea surface temperature forcing causes no significant change in the tropics' width, aside a contraction in some seasons.

To analyse the direct influence of CO_2 on the UTH distribution, it is important to know, how CO_2 can impact atmospheric circulation. [He and Soden \(2015\)](#) found that CO_2 influences the circulation directly and indirectly. Firstly, CO_2 impacts the radiative equilibrium, with less infrared radiation leaving the atmosphere to the space, which weakens the net radiative cooling and thus warms and stabilizes the atmosphere (see also [Bony et al., 2013](#)). But CO_2 also influences the circulation indirectly, by warming the land more than the sea and thus creating a land-sea contrast. Only later do CO_2 lead to surface warming and global mean temperature increase through thermodynamic connections.

To isolate the direct effect of the greenhouse gas on UTH distribution, scientists use a model experiment where CO_2 is increased abruptly and thus impacts the climate system directly before the global mean temperature is changed. In the CMIP5 frame this experiment is called abrupt4xCO2.

[Bony et al. \(2013\)](#) found that the dynamic adjustment starts at the very first day after quadrupling of CO_2 and concluded that about half of the 30-year mean change from abrupt4xCO2 is achieved within five days. Following this result, it can be assumed that the fast adjustment of the climate system to the CO_2 change is effective and visible in the very first year of the model run, while temperature change in the same time is still small compared to the whole warming (< 1 K, Figure 5.19).

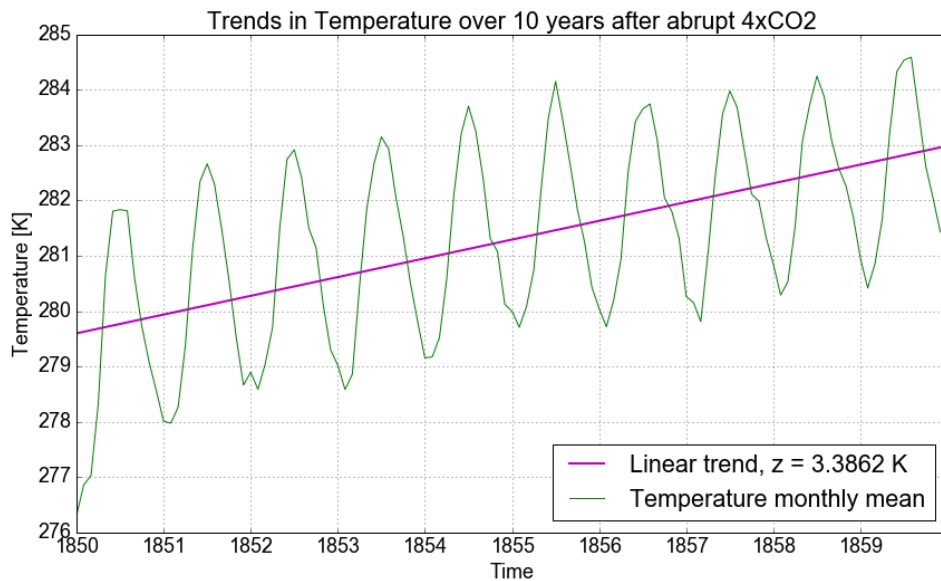


Figure 5.19: Global mean temperature in the first decade of abrupt4xCO2.

Likewise to [Bony et al. \(2013\)](#) (Figure 2a and 2e), the first year of the abrupt4xCO₂ experiment has been analysed in Figure 5.20, assuming that the thermodynamic response is not too dominant yet. Abrupt4xCO₂ and 1pctCO₂ both start from pi-Control. In the first year of 1pctCO₂, the changes due to 1 % CO₂ increase are negligible and hence the first year of 1pctCO₂ does not differ much from piControl. Therefore, it is possible to compare the first year of both experiments (Figure 5.20) in order to evaluate the direct effect of CO₂ on UTH.

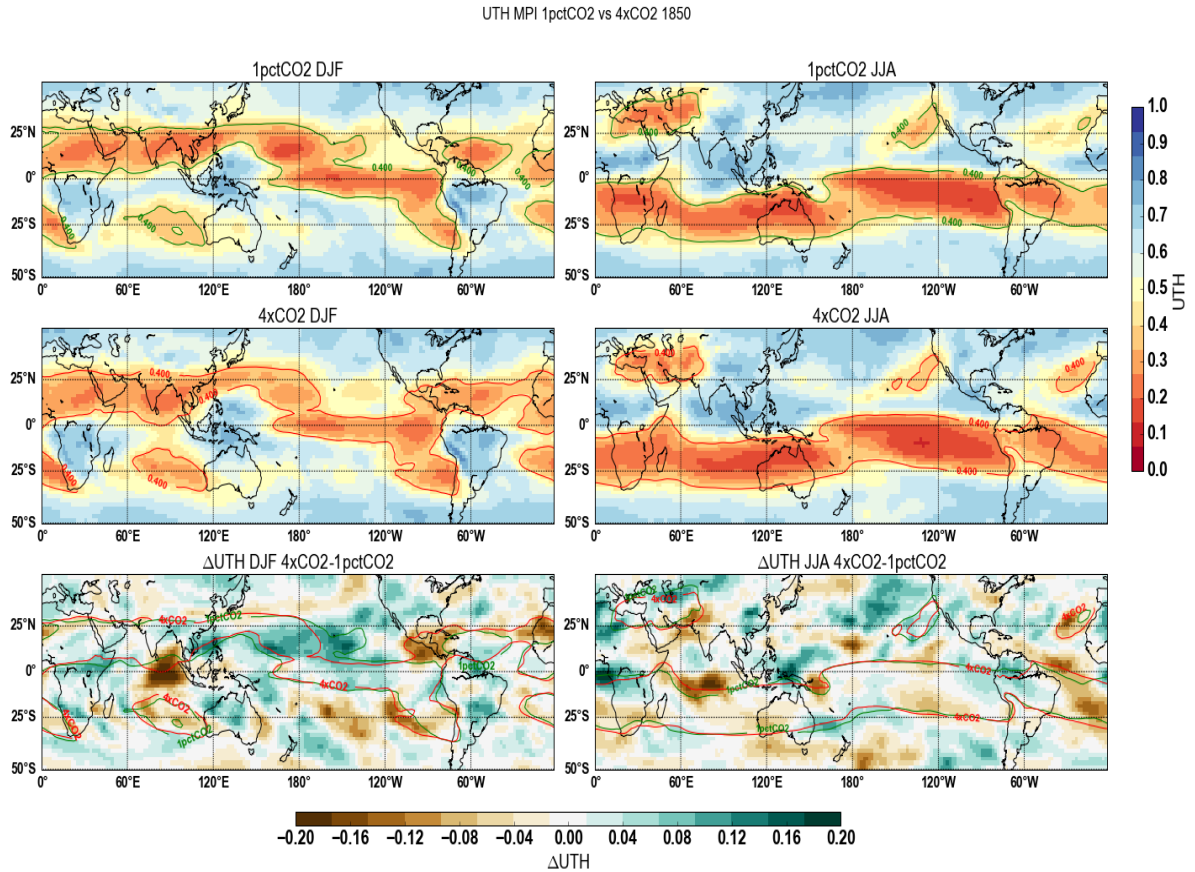


Figure 5.20: Yearly mean of UTH in the 1pctCO₂ run (top) and in the abrupt4xCO₂ (middle) model run for the first year (1850) for January, February and December (left) and June to August (right). The bottom plots show the difference between the two experiments. The contour lines indicate dry zones with UTH smaller than 40 % for the 1pctCO₂ run (green line) and abrupt4xCO₂ (red line).

In the northern-hemispheric winter (DJF), UTH changes strongly in many subtropical regions. Important moisture reductions occur primarily over ocean, while strong UTH increases can be found over parts of the Pacific ocean and over land. This might be an indication that UTH changes due to abrupt CO₂ quadrupling is caused by the land-sea warming contrast.

The amplitude of the fast response is similar to the amplitude of changes at the end of the 1pctCO₂ simulation, but the pattern differs. Only changes in the

regions around Central America, stretching from the tropical East Pacific north of the Equator towards the Caribbean Sea, and the eastern tropical Atlantic Ocean near the North African coast are showing the same drying trend in both simulations. In the other regions, UTH changes differently between the two experiments. In the main parts of subtropical North Pacific Ocean, UTH is increased in DJF in abrupt4xCO₂. UTH decreases in wide areas of the South Pacific and in the Indian Oceans. Both trends are in the opposite direction in the transient simulation.

In the Southern Hemisphere, two observations can be made: first, the subsidence regions of the Subtropical Anticyclones in the South Pacific, South Atlantic and South Indian Oceans described in 5.2.3 are drier in abrupt4xCO₂ than in 1pctCO₂, which would indicate a reaction contrary to the one in the transient model run. The second change is the most prominent one in DJF, with a strong drying trend in the tropical Indian Ocean between India and Indonesia.

Section 5.2.3 explained the possible link between Subtropical Anticyclones and monsoon circulation. Therefore, the drying trend in the subsidence region of the subtropical high west of Australia could be in relation with the UTH increase in central Australia, indicating an enhancement of the Australian monsoon.

In JJA it is even more difficult to distinguish a clear pattern in the changes due to abrupt increase of the CO₂ concentration. The dry belt in the Southern Hemisphere shows no consistent change. The subsidence zone of the Subtropical Anticyclones in the North Pacific Ocean is slightly moister than in the 1pctCO₂ run, but at the same time, UTH is lower in the descent region of the Azores High. The latter could be related to increasing UTH in North West Africa, a possible indication for an enhancement of the African monsoon circulation. The regions with decreasing UTH in the central Indian Ocean as well as over Pakistan and North India are similar to the results found in 1pctCO₂, but it is not clear, if the mechanisms leading to these drying trends are the same.

The abrupt increased CO₂ concentration affects radiative forcing and atmosphere's stability, which in turn change the general atmospheric circulation, but do not influence at the beginning the system's thermodynamic. [Bony et al. \(2013\)](#) analysed the changes in precipitation by separating the dynamical component, directly related to vertical velocity, and the thermodynamical component, related to the Clausius Clapeyron relationship, and found out, that in the very first year after the abrupt greenhouse gas increase, mostly the dynamic component contributed to the change in the precipitation pattern, while the thermodynamic component stayed weak until the temperature change passed one Kelvin. Likewise to UTH, in the first year, the precipitation pattern showed large regional differences, but mainly between land and ocean (see also [He and Soden, 2016](#)). However, [Bony et al. \(2013\)](#) found as well an El-Nino like structure over ocean. This results could not be verified for

UTH in the MPI-ESM-MR model.

Still following the procedure of [Bony et al. \(2013\)](#), the vertical velocity reaction to abrupt CO₂ quadrupling has been analysed in Figure 5.21. But the results of [Bony et al. \(2013\)](#) (weakening of subsidence over land and ocean, weakening of uprise motions over ocean and strengthening of uprise motions over land) could not be confirmed. The pattern of changes in vertical velocity differ also from the pattern of the changes in UTH for the same experiment, especially for the boreal winter season (DJF) (Figure 5.20). The reason for this can be for example, that climate variability is too dominant, when using only one year of model data or that other factors, like lateral mixing, are playing a role. Nevertheless it was not possible to find a concluding explanation for this model behaviour and it can not be excluded that this behaviour is model specific for the MPI model.

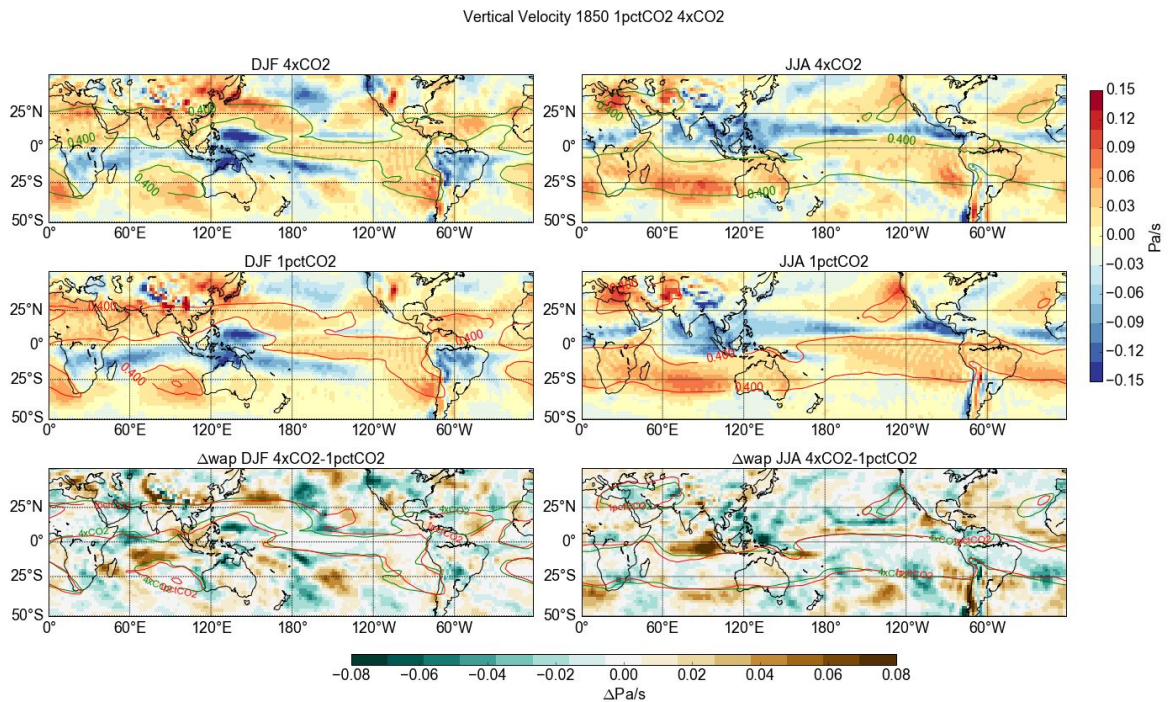


Figure 5.21: Seasonal mean of vertical velocity in MPI-ESM-MR model run with abrupt CO₂ quadrupling abrupt4xCO2 (top) and transient increasing CO₂ concentration 1pctCO2 (middle) for DJF (left) and JJA (right) of the first model year (1850). The bottom plots show the difference of seasonal mean of vertical velocity between the 1pctCO2 and abrupt4xCO2 model run for 1850. The lines show the respective dry zones with UTH smaller than 40 % RH in abrupt4xCO2 (green) and 1pctCO2 (red).

[He and Soden \(2015\)](#) found a strengthening of the Walker circulation caused by the landsea warming contrast as an indirect but also fast effect of CO₂, overpowering the direct CO₂ forcing, which alone would weaken the circulation. In the abrupt4xCO2 experiment, nothing indicates this strengthening of the Walker circ-

lation, neither in Figure 5.20 nor in Figure 5.21. Concerning the Hadley circulation, He and Soden (2015) found a weakening of the northern cell, while the southern cell did show no consistent change in their experiment. In the MPI-ESM-MR experiment abrupt4xCO2 again no consistent change in the Hadley circulation can be found in the first year of the run.

When taking the seasonal mean of the first decade (1850-1859) of abrupt4xCO2 compared to 1pctCO2, the pattern of the changes in UTH and vertical velocity still do not correlate absolutely well, but they show considerably more similarities than in the first model year, most of all in JJA (Appendix D).

In order to focus again on the dry zones, the behaviour of the frequency of occurrence of UTH smaller than 30 % RH (UTHp30) in the first year after the abrupt quadrupling of CO₂ (Figure 5.22) has been analysed. Changes can be found mainly in the tropics between 25° South and 25° North. Most prominent is an increase in UTHp30 at the poleward edge of the dry zones in the South Hemisphere, resembling the pattern of a poleward expansion of the southern subsidence zone of the Hadley Cell. This feature is not visible in the North Hemisphere. One reason for the different behaviour between the hemispheres could be, that the climate system and tropical circulation did not have time to react to the quadrupling of CO₂ in the first months of the model run (January, February), while the reaction is strongest in the first summer (June to August).

In the Indian Ocean UTHp30 increases in the first year of abrupt4xCO2 compared to 1pctCO2. This could be related to a change in the monsoon circulation. An increase in UTHp30 can also be found in the Southern Atlantic Ocean. In the tropical Pacific region, UTHp30 is mostly decreasing with abrupt CO₂ quadrupling, and the pattern resembles the one of a weakening of the Walker circulation, with increasing dryness in the upper troposphere above the western Pacific and decreasing dryness in the Eastern Pacific Ocean. It should be noted however, that no change in UTHp30 can be found above the convection region of the Maritim Continent.

Finally, a change that is interesting because it appeared also in the previous analysed transient experiment, is a drying trend in the upper troposphere above Central America. No satisfying explanation has been found yet for this evolution, but at least, if it is correct that the direct CO₂ forcing mainly influences the dynamics of the circulation, this drying trend in Central America can be imputed to the dynamical factors influencing UTH.

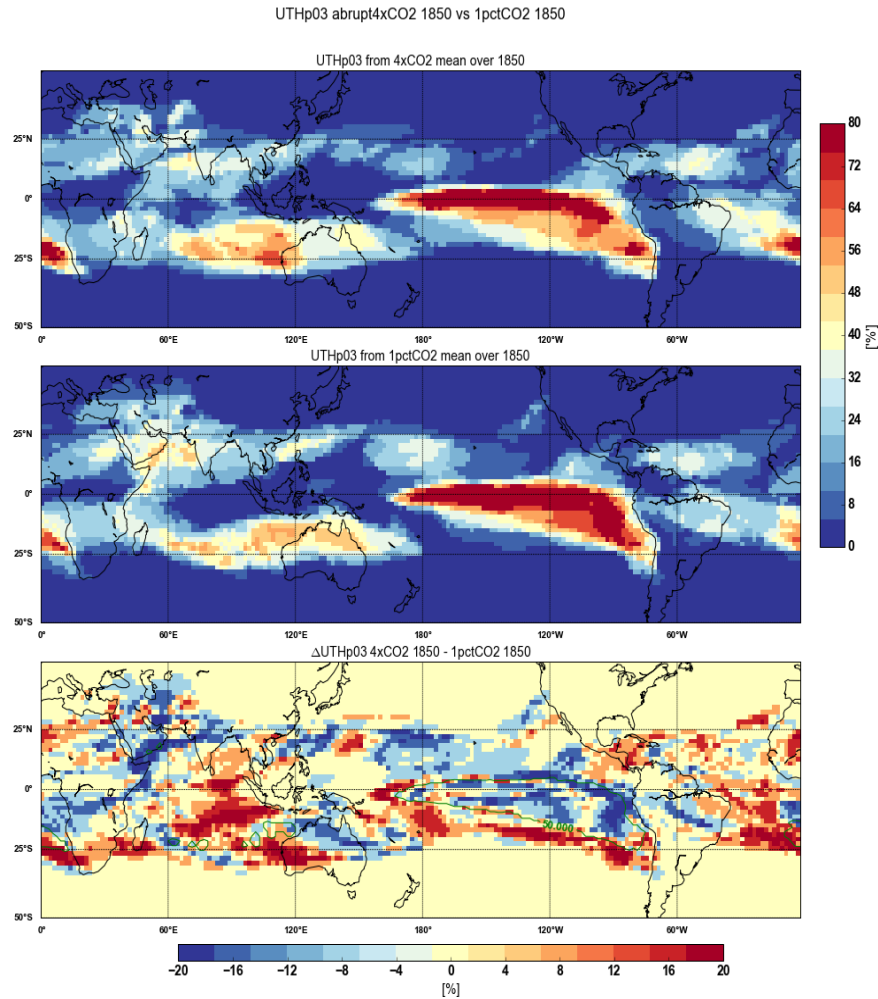


Figure 5.22: Difference of decadal mean of UTHp30 in 1pctCO₂ and abrupt4xCO₂ model run for 1850.

The study of UTH in abrupt4xCO₂ has shown that UTH is strongly reacting to the direct CO₂ forcing, but no clear pattern can be identified. Changes have been found especially in the monsoon regions and above the Pacific Ocean, but can not be attributed to concrete phenomenons. The decrease in UTH in the descent regions of Subtropical Anticyclones in the Atlantic and Indian Ocean could be associated with an enhancement of the summer monsoons, but no similar trend can be seen in the Pacific Ocean. By analysing the frequency of occurrence of UTH smaller than 30 % RH in the yearly mean, it is possible to discern an expansion of the southern subsidence region of the Hadley Cell towards the South Pole as well as a weakening of the Walker circulation.

Until now, only the experiments of the MPI-ESM-MR model have been used for the reasons mentioned before. In the following Section, two further models will be briefly analysed, in order to assess the significance of the previous results.

5.4 Comparison with other CMIP5 Models

More than 20 models are currently participating in the CMIP5 project (Annex A). The aim of this diversity is also to cover a maximum of possible responses to the different forcings tested during the project. By only taking into account one of these models, the results are also only one of the possible realisations, and the risk is not negligible to obtain too extreme responses to a given forcing.

The processing of all the models through the satellite simulation software COSP and the forward operator RTTOV would have been too time consuming in the frame of the present master thesis. Therefore, only one model has been analysed in detail. The main results shall now be compared with two other models of CMIP5.

Figure 5.23 shows the evolution of the global mean of UTH in the 1pctCO2 runs of the three models CNRM-CM5A, BCC-csm1 and MPI-ESM-MR for winter and summer in both hemispheres. The trends are deseasonalised and represent thus the anomalies of UTH. The three models show all decreasing trends in UTH for the winter hemispheres and increasing trends in the summer hemispheres. The only exception is the BCC-csm1 model in the Northern Hemisphere winter (DJF), where the trend is positive, but very small (+0.06 % for the whole period versus -0.8 % for CNRM-CMA and -2.1 % for MPI-ESM-MR). Generally the MPI model has lower UTH values than the two other models. In the winter hemispheres, the decreasing trends are larger for the MPI model but in the summer hemispheres, the MPI model shows the weakest increase in UTH. The MPI model seems to be broadly in the same range as the other CMIP5 models.

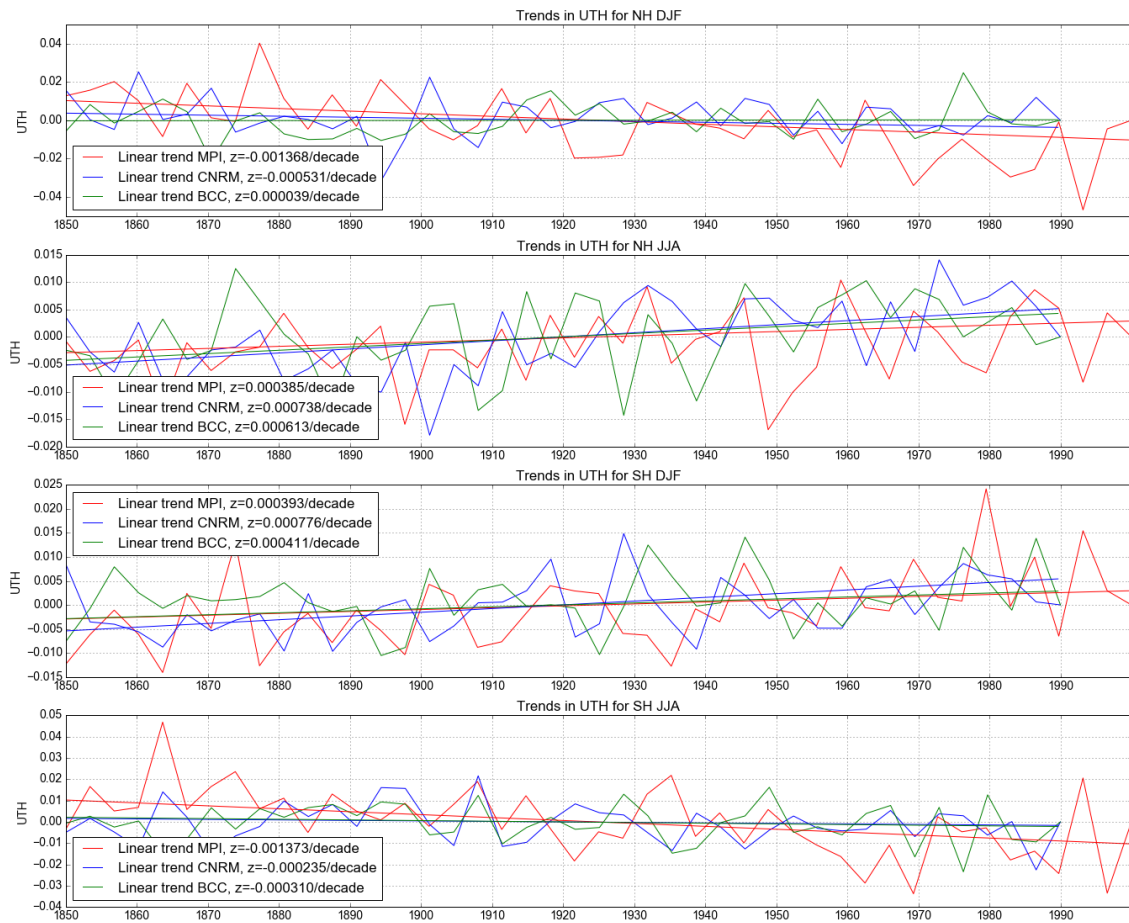


Figure 5.23: Timeseries of UTH from 1pctCO2 runs of models MPI-ESM-MR, CNRM-CM5A and BCC-csm1 for DJF and JJA on Northern and Southern Hemisphere.

To go further in the details of the representation of UTH and the upper tropospheric dry zones by the two comparison models, the global distribution of UTH in the first and the last decade of the 1pctCO2 runs of CNRM-CM5A and BCC-csm1 respectively has been plotted in Figure 5.24 and Figure 5.25.

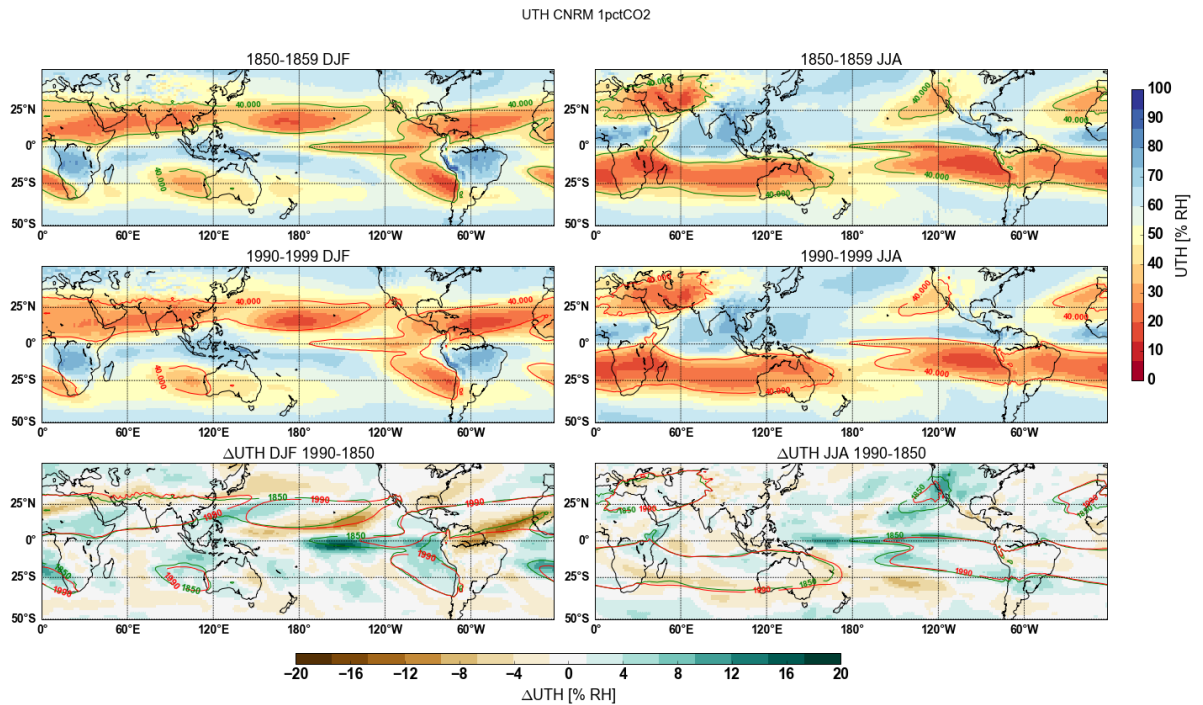


Figure 5.24: Decadal mean of UTH for the first (top) and the last (middle) decade of the CNRM-CM5.1 1pctCO₂ model run for DJF (left) and JJA (right) and the difference between the two decades (bottom). The contour line indicates the limits of the dry zones with UTH smaller than 40 % RH.

In comparison with the MPI model, the dry zones in the upper troposphere calculated from the 1pctCO₂ run of CNRM are smaller in the Pacific Ocean but larger in the Atlantic Ocean in the first decade. In the model of BCC, UTH values are generally less extreme and the dry zones are considerably smaller than in MPI and CNRM. In comparison with the last decade of the 1pctCO₂ runs, the trends are consistent between the MPI and the CNRM with increasing UTH values around the Equator in the Central Pacific in both seasons, drying at the poleward edges of the dry zones in the winter hemispheres and a slight moistening of the descent zones of the Subtropical Anticyclones in the summer hemispheres. But the pattern of the changes in the subtropical Pacific differ between the two models especially in DJF and the magnitude of changes is smaller in CNRM in both seasons. As in the MPI model, the dry zone in the South East Pacific in JJA reduces, but apart from this, nothing indicates a weakening or an eastward shift of the Walker circulation in CNRM.

The comparison with the BCC model run points out more differences with MPI. A part from the difference in magnitude, UTH's evolution in the Pacific and Atlantic Ocean differs between the two models. No change can be found in the Walker circulation and the drying trend found in MPI in the tropical Atlantic is restricted here to the region between Brazil and West-Africa, while in the Caribbean UTH

is even increasing in the course of the BCC model run. Similarities between the model results can be found however in the drying trend at the poleward edges of the subtropical subsidence zones, even though the magnitude is more important for MPI, and at the eastern flanks of the Subtropical Anticyclones, especially the one in the North Pacific in boreal summer.

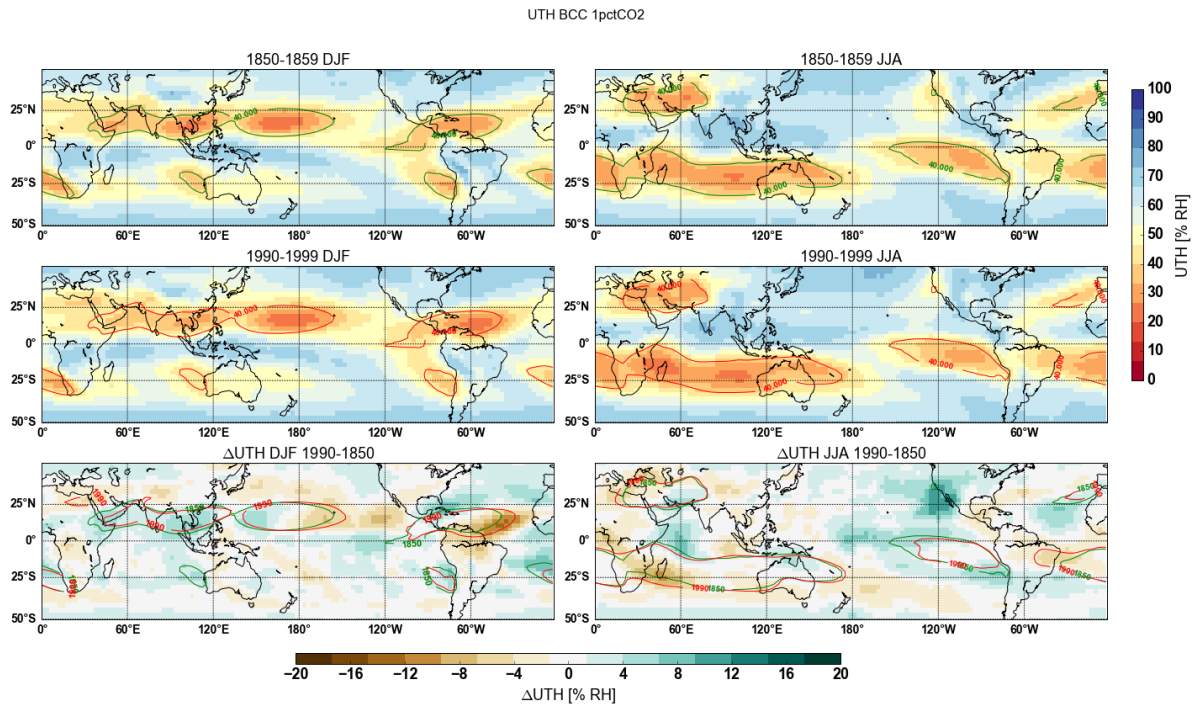


Figure 5.25: Decadal mean of UTH for the first (top) and the last (middle) decade of the BCC-csm1 1pctCO2 model run for DJF (left) and JJA (right) and the difference between the two decades (bottom). The contour lines indicate the limits of the dry zones with UTH smaller than 40 % RH.

The comparison with the two models, CNRM and BCC, shows that the results from MPI-ESM-MR although differing in the magnitude of the signal, are consistent with at least two of the other CMIP5 models concerning the poleward expansion of the dry zones in the winter hemispheres, as well as the weakening of the dry zones related to the Subtropical Anticyclones, especially the one in the North Pacific. To further evaluate the significance of the described trends found in the MPI-ESM-MR model runs and in particular of the trends not confirmed by CNRM and BCC, an investigation of UTH with a complete model ensemble of CMIP5 models would be needed.

5.5 Comparison with Satellite Observations

The final Section will give a brief insight in UTH from real observations. For this, UTH calculated from brightness temperatures measured by satellite based instruments will be presented similarly to the model data, in order to analyse the general structures of the dry zones and detect possible visible trends.

For the comparison with satellite data, AMSU-B microwave measurements of brightness temperature have been used. Because of the non-Gaussian nature of the UTH distribution (Figure 5.4), it is more appropriate to use the median than the mean for UTH (Buehler et al., 2008, and citations herein). For reasons of comparability, the UTH distribution has been represented again separately for DJF and JJA (Figure 5.26). As the time series of UTH from microwave data only comprises 15 years, in Figure 5.26 only the five first and the five last years have been analysed. The difference has been normalized by the mean UTH of the first period (1999-2005) in order to emphasize changes in the dry regions.

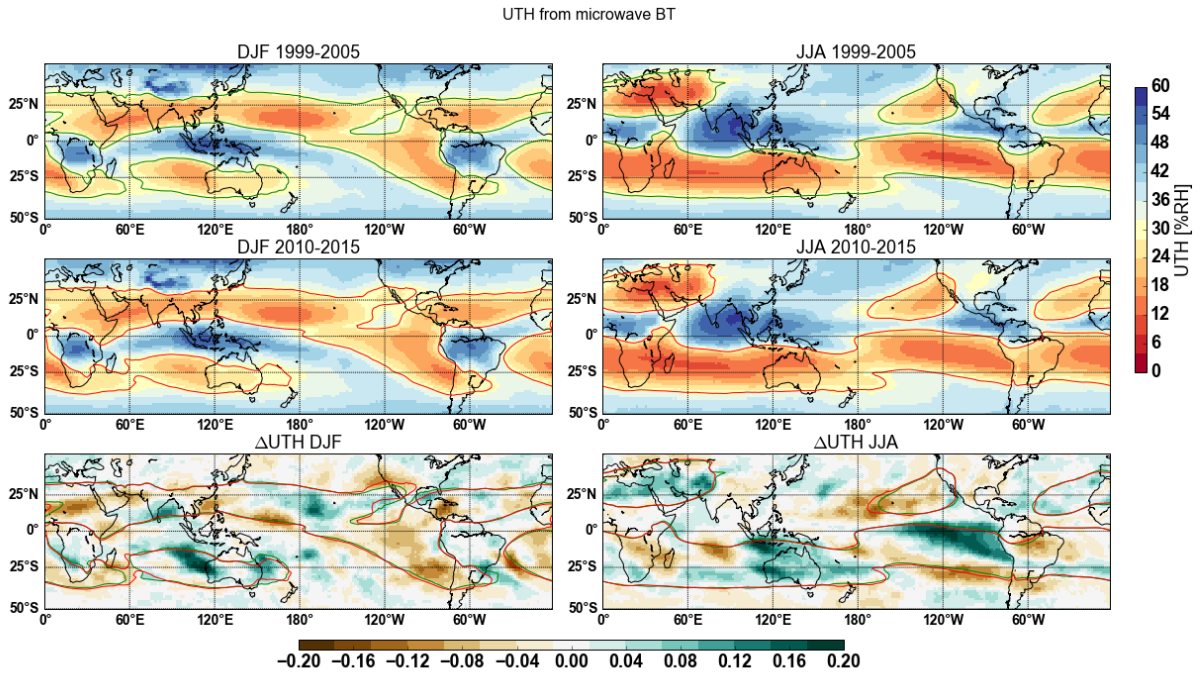


Figure 5.26: Mean of the median of UTH from microwave data for DJF (left) and JJA (right) for the periods 1999-2005 (top) and 2010-2015 (middle). The bottom plots show the difference between the two periods normalized by the mean UTH of 1999-2005. The contour lines indicate UTH of 30 % RH.

The model data is taken from an idealized experiment and do not reflect exactly the real climate. But at least the pattern of UTH should be similar for the UTH distribution in satellite measurement and the last decade of the model run with gradually increasing CO₂ (1pctCO₂).

From December to January the main dry belt can be found in the northern subtropical subsidence zones with main dry regions over the Arabian peninsula, the North-Eastern tropical Pacific and the Caribbean. In the Southern Hemisphere, the Subtropical Anticyclones are clearly visible in terms of low UTH values, with even lower humidity than in the same regions in the model data (< 20 %). Generally values of UTH are lower in the satellite data than in the model data.

This is also the case from June to August, when the southern subtropics are characterised by a band of low humidity. Especially low UTH values are found in the Southern Indian Ocean and in the east Pacific, but also in the southern subtropical Atlantic. This confirms the findings from the model data, that lowest humidities are found in general in the winter hemisphere. In the Northern Hemisphere in JJA, the eastern flanks of the Subtropical Anticyclones are again exhibiting small UTH values, but the region comprising the East Mediterranean, the Arabian Sea and Asia minor have by far the lowest UTH values in the Northern Hemisphere, and the dry zone in this region is far more developed than in the model data from MPI. Unsurprisingly the monsoon regions are characterised by high UTH values.

The bottom plots of Figure 5.26 represent the difference in UTH between the first and the last five years of UTH retrieved from the microwave dataset. In analogy to the results in Chapter 5.2, the poleward edge of the winter dry belt can be analysed in the satellite data (Figure 5.27 and 5.28, but the dry belt has been defined as the region with UTH smaller than 30 % RH rather than 40 % RH like in the model data, because UTH is generally drier in the AMSU-B microwave dataset than in the model data.

In the winter hemisphere, the edge of the winter dry belt has shifted northwards in the 16 years of observations. This shift is visible in the explicit plot of the dry zone edges (Figure 5.28) as well as in the differences between the edges (Figure 5.27). On average the northern dry belt shifts by 1.8° towards the North Pole. This shift is relatively important when considering the short time period which has been analysed with 16 years compared to the 150 years of model data, but it comprises also the peaks which are visible in Figure 5.28 and which are due to the complex structure of the dry zones in the east Pacific, where the dry belt is interrupted in the northern hemisphere and extends into the South Eastern Pacific. Therefore, it is not clear if this shift can be already interpreted as a trend or if it is only due to the way of calculation or to climate variability.

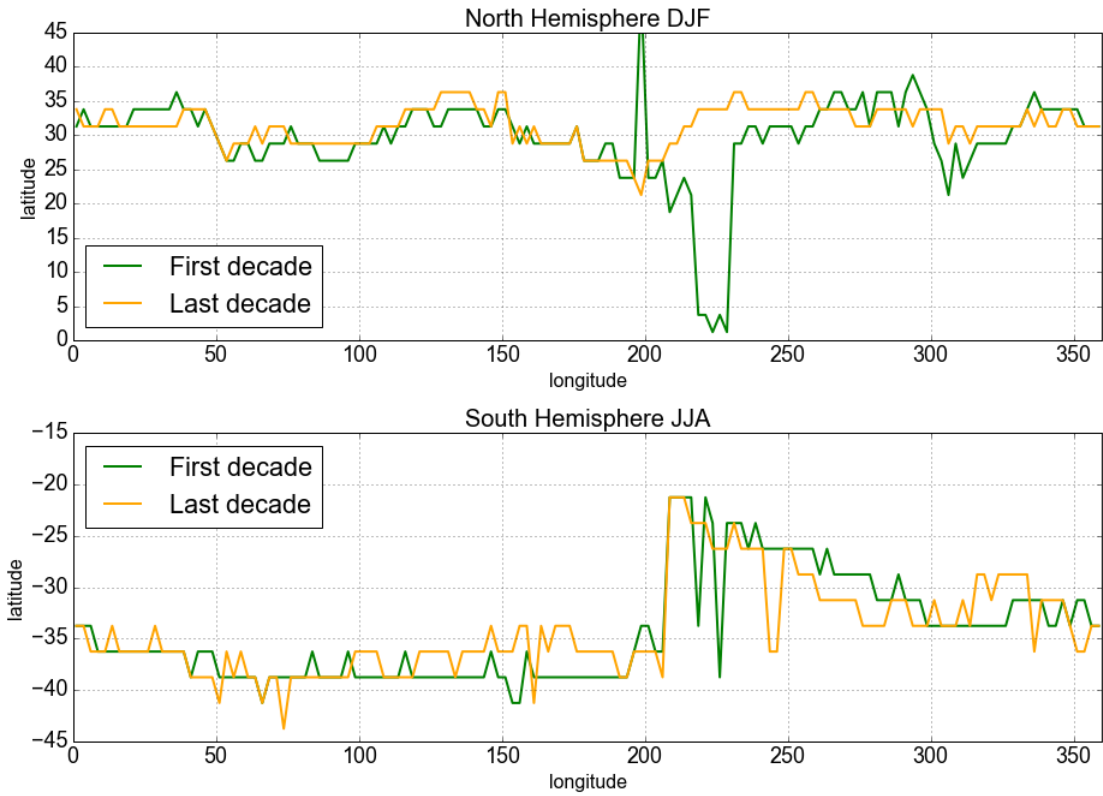


Figure 5.27: Northern (top) (southern (bottom)) edge of drybelt for December, January and February (June, July and August) in UTH calculated from microwave measured brightness temperature for 1999-2005 and 2010-2015.

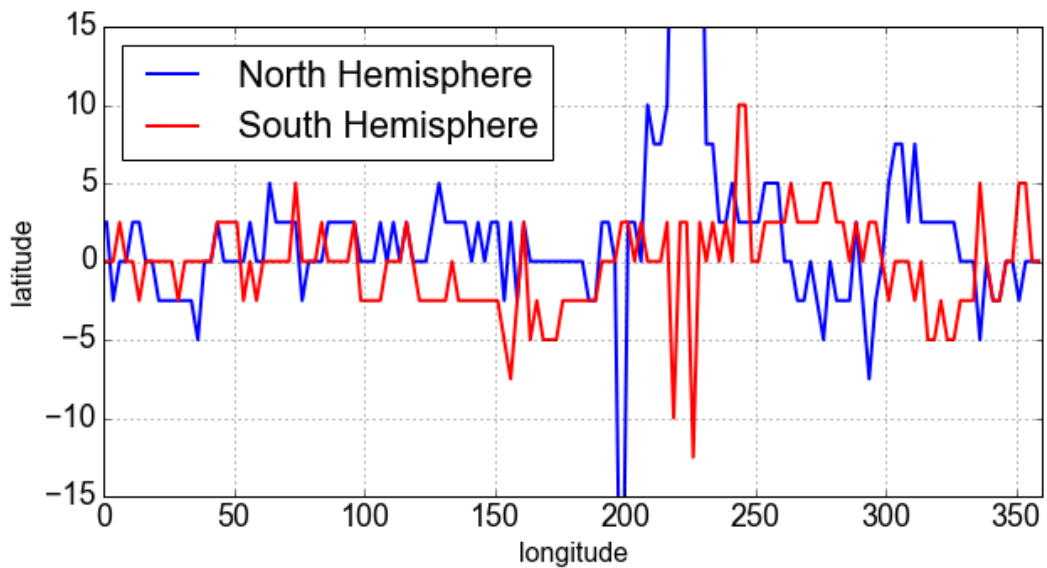


Figure 5.28: Difference of the latitudes of the Northern (DJF) (southern (JJA)) edge of the drybelt between the last and the first five years of the UTH calculated from microwave measured brightness temperature.

In the Southern Hemisphere no such trend can be found in Figures 5.27 and 5.28. The mean of the drybelt shift calculated with satellite data amounts to 0.2° , which means that the southern edge of the winter dry zone has if anything the tendency to shift equatorwards. In the southern hemisphere there has been at least in the 16 years of AMSU-B measurement no signal of poleward expansion of the dry subsidence zones.

These results do not totally confirm the ones reported for example by [Johanson and Fu \(2009\)](#), who found in observations, that the Hadley Cell has widened by about 2° to 5° since 1979. In UTH calculated from microwave data, this widening can only partly be confirmed for the Northern Hemisphere, while in the Southern Hemisphere no poleward shift has been detected. Probably, the time series of microwave based data is not long enough to really draw final conclusions on this matter.

The second structure which has been analysed with the model data has been the descent regions at the eastern flanks of the Subtropical Anticyclones in the summer hemispheres. In the general overview of UTH, these regions of low UTH are clearly discernible in Figure 5.26. But no consistent trend can be found for the Subtropical Anticyclones between the beginning and the end of the satellite time series. While the dry zones in the tropical North Atlantic (JJA) and the South East Indian ocean (DJF) are moistening in the satellite data, the dry zones in the North Pacific (JJA), the South Atlantic (DJF) and the South Eastern Pacific (DJF) are showing drying trends. No clear conclusions can be drawn from these results. The same can be said for the structures in the Pacific oceans in general, where neither the eastward shift of the Walker circulation nor the Central American drying trend can be directly observed.

Finally, to make the data from satellite and model as comparable as possible, UTH from model data has been plotted also for the last years of the model run, for 1970-1979 in comparison with 1990-1999 (Figure 5.29). Without going into too many details, the comparison of the dry zones reveals only few similarities. In DJF, while the model data shows an overall moistening trend in the dry zones of the Pacific ocean, UTH from satellite data shows a moistening only in the Central Pacific ocean and a drying trend in the rest of the dry zones, especially in the south eastern Pacific. Model data reveals a clear moistening of the dry regions over South East Asia, but no clear trend in the Southern Indian ocean, while satellite data shows a clear moistening trend over Australia and the Eastern South Indian ocean. The only similarities in DJF can be found in the drying trends in the Caribbean and above North West Africa.

In JJA the pattern of the changes in the Pacific are at least comparable, with a more (satellite UTH) or less (model UTH) drying in the North, a moistening in the central and east tropical Pacific and a drying trend at the poleward edge

of the southern dry belt. Similarities can also be found in a moistening trend in the dry region in the upper troposphere above the Arabian Peninsula and a drying trend in parts of Southern Africa and Southern America. But the trends in the southern Indian ocean and around Australia are very different between model data and satellite based measurements.

It is difficult to say to what extent these trends can be trusted and are significant, because the time series of satellite measurements especially in the microwave spectrum are still very short compared to the climatological processes and phenomena, like the El-Nino-Southern-Oscillation, have strong influence on the humidity pattern of the upper troposphere.

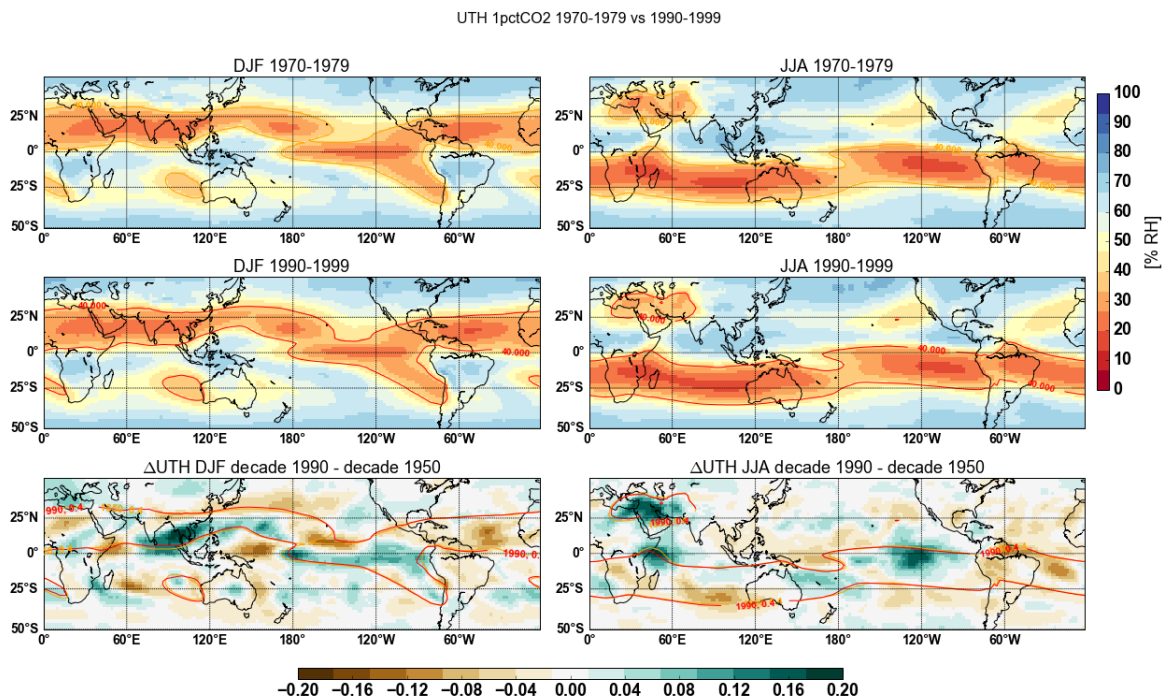


Figure 5.29: UTH in the decade 1970-1979 (top) and the last decade 1990-1999 (middle) of the 1pctCO2 run of MPI-ESM-MR model and the difference between both decades (bottom) for DJF and JJA. The contour lines in the bottom plot indicate the regions with UTH smaller than 0.4 in 1970-1979 (green) and in 1990-1999 (red).

Measurements in the infrared spectrum have been started earlier and so UTH calculated from brightness temperature based on infrared measurements can be analysed on longer timescales than those based on microwave measurements. But as said in 2.3.3., infrared radiation cannot penetrate clouds and UTH measured from infrared brightness temperature has or a wet bias, or if a cloud filter is used, a dry bias, while microwave radiation is less influenced by clouds. Nevertheless the present study shall be finished by an overview over the time series of UTH from both sensors (Figure 5.30 and 5.31).

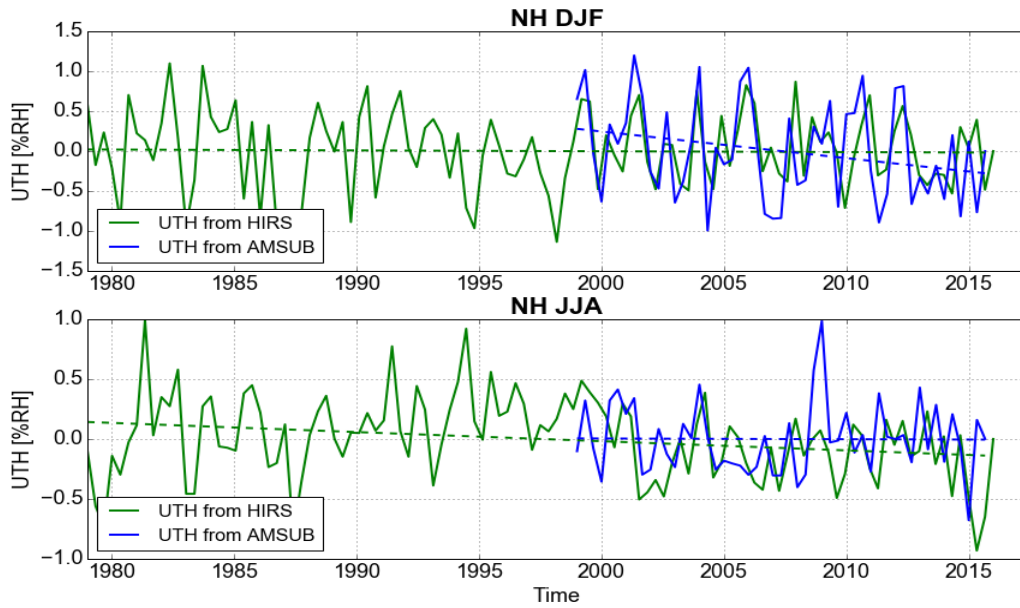


Figure 5.30: Timeseries of UTH from microwave (blue) and infrared data (green) in the Northern Hemisphere for winter (DJF, top) and summer (JJA, bottom). The dotted lines are the respective linear trend lines over the 17 years of observation for microwave and 37 years of observation for infrared data.

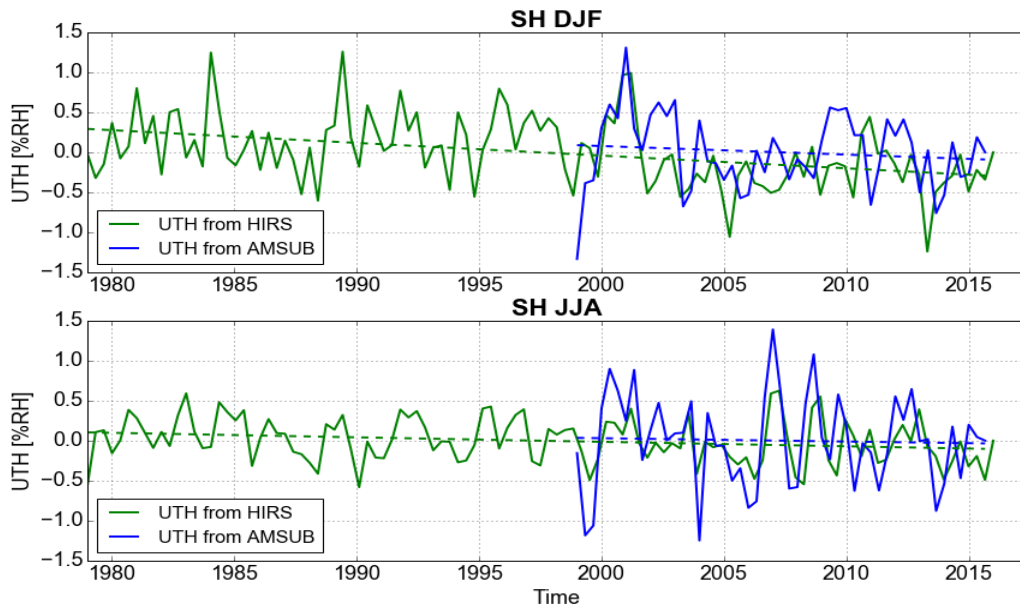


Figure 5.31: Timeseries of UTH from microwave and infrared data in the Southern Hemisphere for summer (DJF) and winter (JJA). The trend lines are like in Figure 5.30.

The time series of UTH are separated for the hemispheres and the seasons, as the present study has shown, that UTH behaves differently dependant on these parameters. The Northern and Southern Hemisphere have been delimited respectively from 0° to 45°N and from 0° to 45°S. To eliminate the mean seasonal variation, the time series are deseasonalised, by subtracting the monthly mean of the first ten years of each dataset at each time-step.

None of the time series reveals a strong trend. But UTH shows in all of the scenarios a tendency to decrease (Table 5.2).

Table 5.2: Trends in UTH calculated from satellite based measurements

Hemisphere (season)	Linear trend [% RH/period]	Significance ¹
Microwave data		
North (DJF)	-0.5665	0.99
North (JJA)	-0.0103	0.04
South (DJF)	-0.1820	0.42
South (JJA)	-0.0705	0.13
Infrared data		
North (DJF)	-0.0396	0.08
North (JJA)	-0.2826	0.83
South (DJF)	-0.5873	1.37
South (JJA)	-0.2075	0.74

¹ Calculated by the signal to noise relation (Hennemuth et al., 2013).

UTH calculated from infrared measurements (HIRS) shows a small negative trend in the Northern Hemisphere (NH) in winter (DJF), and a clearer trend in the Southern Hemisphere in summer (DJF). UTH from microwave measurements has decreasing trends in the 17 years in all hemispheres and seasons, but the trend is near to zero in JJA. The significance has been calculated by the signal to noise relation (Hennemuth et al., 2013), using the standard deviation calculated by:

$$\sigma = \sqrt{\frac{1}{N-1} \sum_{i=1}^N (x_i - \mu)^2}. \quad (5.1)$$

The signal to noise method relates the linear trend to the standard deviation of the time series and gives an indication of the significance of the trend. To be significant the ratio has to be at least higher than 1. But the trends found in the satellite data

are generally not significant, only in the infrared data, the trend of the Southern Hemisphere in summer (DJF) proves to have a significant trend (significance = 1.37). In the microwave data, the trend for the north hemispheric winter (DJF) is close to be significant (significance = 0.99). All the other trends have not been found to be significant and no conclusion can therefore be drawn about the evolution of UTH.

For these time series, UTH has been measured in the tropics and subtropics. In these regions there are not only the most important dry zones but also the region of the ITCZ marked by high humidity throughout the troposphere. To better capture the behaviour of the tropical and subtropical dry zones in the satellite data, these regions have been defined by the mean of UTH smaller than 30 % RH for the microwave data and smaller than 10 % RH for the infrared data. UTH computed from infrared radiation is significantly lower, that is why the threshold has been chosen differently between the two datasets. Nevertheless, the so defined regions are corresponding in the two datasets.

The dry zones analysed in Figures 5.32 and 5.33 have not changed significantly in the last decades. There are positive trends indicating an increase in the frequency of occurrence of dry events, but these trends are not significant compared to the climatic variability (Table 5.3). In the microwave data, the most important trend can be found in the north hemispheric winter (DJF), which is also characterised by the highest significance (0.33) and which corresponds to the results from the model data, where the dry zones in NH and DJF were the ones with the highest increasing trend. In the infrared data though, the highest trend representing also the highest value for the significance, is found in the south hemispheric summer (DJF). The only conclusion that can be drawn from these results is again, that the time series of satellite measurements are probably not long enough yet to really see a consistent trend in the evolution of UTH, regarding the dry zones in the tropical and subtropical regions. Nevertheless, the small trends found in all time series show a decrease of UTH and an increase in the frequency of occurrence of low UTH. It will be interesting to follow this evolution in the coming decades.

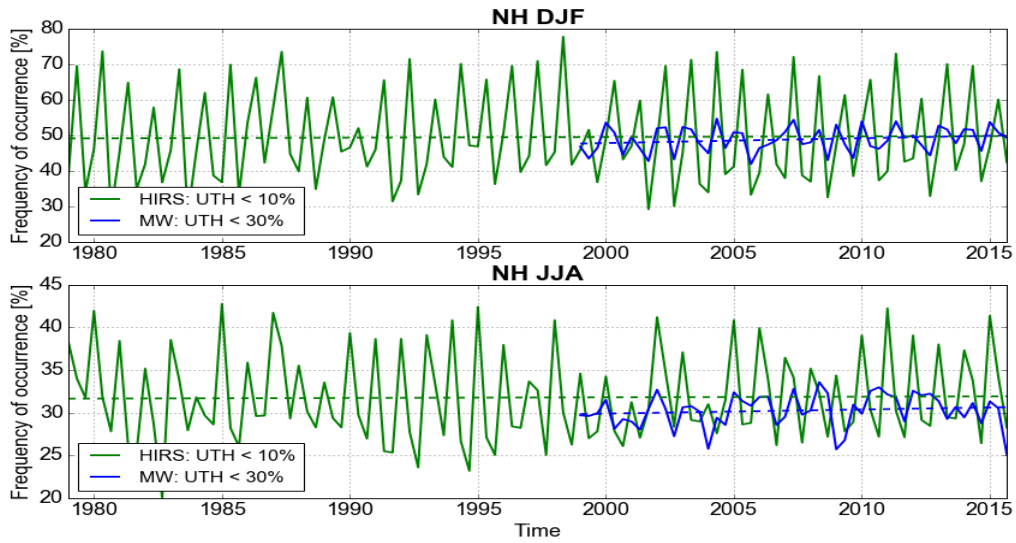


Figure 5.32: Timeseries of UTH smaller than 30 % RH from microwave (blue) and smaller than 10 % RH infrared data (green) in the Northern Hemisphere for winter(DJF, top) and summer(JJA, bottom). The dotted lines are the respective linear trend lines over the 17 years of observation for microwave and 37 years of observation for infrared data.

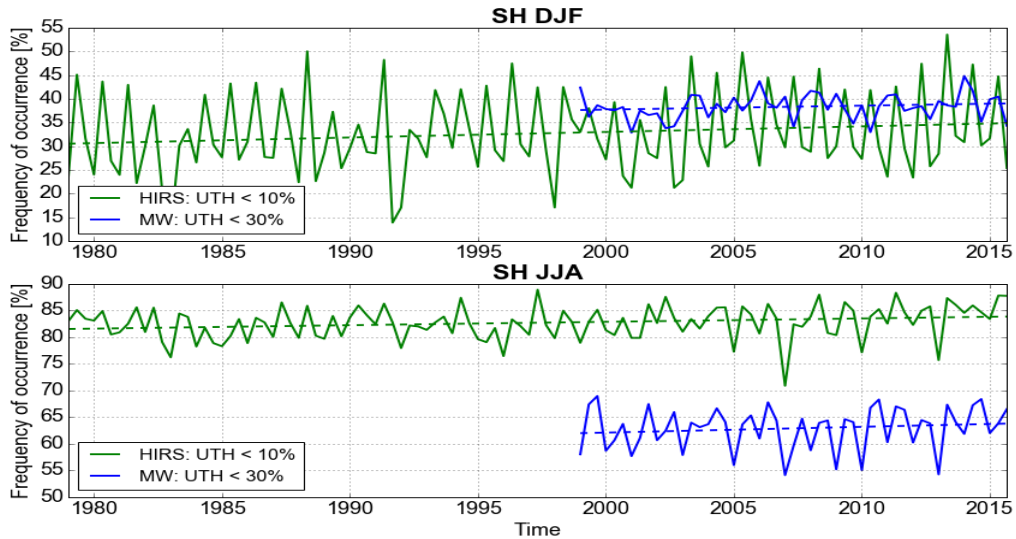


Figure 5.33: Timeseries of dry zones from microwave and infrared data in the Southern Hemisphere for summer (DJF) and winter (JJA). The trend lines are like in Figure 5.30.

Table 5.3: Trends in dry zones calculated from satellite based measurements

Hemisphere (season)	Linear trend [% RH/period]	Significance ¹
Microwave data		
North (DJF)	2.30	0.33
North (JJA)	0.82	0.19
South (DJF)	1.41	0.26
South (JJA)	1.82	0.21
Infrared data		
North (DJF)	0.68	0.05
North (JJA)	0.27	0.05
South (DJF)	4.34	0.50
South (JJA)	2.35	0.28

¹ Calculated by the signal to noise relation ([Hennemuth et al., 2013](#)).

Chapter 6

Conclusion

In this thesis the evolution of dry zones in the upper troposphere has been analysed by means of the radiation variable UTH. UTH has been computed with an algorithm developed by [Soden and Bretherton \(1996\)](#) and enhanced by [Buehler and John \(2005\)](#), using model data from CMIP5 as well as observation data from satellite based microwave and infrared sensors. The model data is coming mainly from the Max Planck Institut Earth System Model (MPI-ESM) and the output of the experiments with gradually increasing CO₂ concentration (1pctCO₂) and abrupt CO₂ quadrupling (abrupt4xCO₂).

The first part of this thesis was consecrated to the physical and meteorological background, explaining the structure of the general atmospheric circulation and the subsidence regions, as well as the role of water vapour in climate sensitivity in general and of upper tropospheric moisture in particular. Although and because water vapour concentration in the upper troposphere is quite low, changes in this concentration can have a considerable impact on the radiative budget. This is due to the logarithmic proportionality between water vapour concentration and outgoing longwave radiation in the upper troposphere.

The upper tropospheric dry zones are therefore crucial in two regards: first their position impacts the precipitation budget underneath, but secondly their extend as well as their intensity plays a major role in regulating outgoing longwave radiation and through this the Earths energy budget. But due to the difficulties in in situ measurements in the higher Troposphere, many uncertainties remain regarding the reaction of UTH and the evolution of dry zones in climate change.

That is why in this study the UTH has been analysed regarding extend and evolution of the dry zones. In this purpose, UTH had to be computed from model data. Temperature and humidity profiles as well as surface parameters like pressure, temperature and winds from the MPI-ESM model run 1pctCO₂, have been used as input to the satellite simulation software COSP coupled to the forward operator RTTOV in order to obtain a dataset of the radiation variable brightness temperature. This

dataset was afterwards processed with the brightness temperature transformation method to retrieve Jacobian weighted UTH.

Previous studies have found, that UTH was largely influenced by the seasonal shift of the Hadley Cell (DelGenio et al., 1994, e.g.) and that water vapour concentrations are larger in the summer hemisphere in all latitudes, while in the winter hemisphere, a dry belt can be found in the subtropical subsidence regions (Gettelman et al., 2006). Recent research with model data and observations found a consistent weakening and widening of the Hadley Cells, associated with a poleward expansion of the dry subtropical subsidence zones (e.g. Lu et al., 2007). Other studies of UTH revealed increasing trends for the dry end of the distribution, but generally these trends were either not significant or not consistent (e.g. Schröder et al., 2014; Shi et al., 2011).

The present study with the MPI model output confirmed the general humidity distribution of UTH as well as the seasonal cycle at the beginning of the model run with gradually increasing CO₂ concentration. Afterwards, the global evolution of the dry zones has been analysed for the 150 years of the model run separately for the boreal winter (January, February and December, DJF) and the boreal summer (June to August, JJA). In both seasons the general trends indicate an increase in the area of the dry zones, which is clearer in DJF than in JJA but in both cases not significant. Separating the seasons and the hemispheres has shown an increase in higher UTH values in the summer hemispheres and an increase in the dry part of UTH in the winter hemispheres, especially in the northern winter. These findings confirm the results of other studies, where upper tropospheric moisture increases in the intertropical convergence zone (ITCZ), which generally lies in the summer hemisphere, while the upper troposphere is drying in the winter hemisphere subsidence zones (Lu et al., 2007; Hu and Fu, 2007; Johanson and Fu, 2009; Su et al., 2014).

But previous studies of UTH have also shown, that trends in UTH are not homogeneous. Even when considering only the tropics and subtropics, there are regions with increasing and regions with decreasing UTH. Therefore, the spatial distribution of the dry zones has been analysed in Chapter 5.2 and two main structures have been found and studied separately: the winter hemispheric subsidence zones of the Hadley Cell and the dry zones in the east ocean basins in the summer hemispheres, corresponding to the descent regions of the Subtropical Anticyclones. As expected from previous studies, the dry belt in winter has been found to expand poleward by 2 to 3° North and up to 2° South, but the trends are smaller than those found in observations since 1979 (Lu et al., 2007; Hu and Fu, 2007; Johanson and Fu, 2009; Su et al., 2014). The region of the Caribbean and Central America can be seen as part of the northward shift and showed a particular drying trend in the MPI-ESM

1pctCO2 run, partly due to increase in subsidence.

The descent regions in the eastern ocean basins are recognizable as dry zones in the respective summer months. Most of these regions show tendencies to moisten in the 150 years of the model run, but only the dry zone in the North Pacific has a nearly significant moistening trend. These dry zones are part of the Subtropical Anticyclones, which have been analysed by previous studies (Rodwell and Hoskins, 2001; Shaffrey et al., 2002) and linked to the sea-surface temperature, the orography and the monsoons in the east of each Subtropical Anticyclones. In the MPI model run, UTH is mostly increasing in these regions, while the vertical velocity is decreasing. All the trends are very small, except for the North Pacific. But the mechanisms behind these trends are not completely clear. Some scientist found an intensification of the subtropical highs in reanalysis data (Li et al., 2012, 2013), which would in consequence lead to an increase in subsidence and in dryness in the descent regions. At the same time, other studies (e.g. Cook and Seager, 2013) predict a weakening of the monsoons with climate change, which would explain the moistening of the descent regions of the Subtropical Anticyclones. But these dry zones have hardly been analysed before and the study on the mechanisms behind the Subtropical Anticyclones is still ongoing. More research would be needed to have a concluding explanation for the evolution of UTH in those areas.

In the region of the Pacific Ocean, the UTH distribution reflects the pattern of atmospheric circulations and besides the trend of poleward expansion of the subtropical subsidence zones, the predicted eastward shift of the Walker circulation is visible through a drying over Indonesia and a moistening in the central equatorial Pacific. In the following Section, UTH computed from the abrupt4xCO2 run of MPI-ESM has been analysed for the first model year, in order to evaluate the direct effect of CO2 on the upper troposphere. The results show no clear pattern of change for the dry zones even though UTH is strongly reacting to the quadrupling of CO2. Only above the Indian Ocean UTH is clearly decreasing in summer and winter. The southern edge of the subtropical subsidence zone shows poleward expanding trends when analysing the frequency of occurrence of UTH smaller than 30 % RH (UTHp30) in the first model year. The direct effect of CO2 could accordingly lead to changes in UTH through changing the Hadley Circulation and the monsoons. Bony et al. (2013) analysed tropical precipitation reaction to abrupt CO₂ quadrupling and found resulting large regional anomalies with precipitation increase over land, over equatorial eastern Pacific and over subtropical dry regions and precipitation decrease in regions of high present day precipitation. Parts of these results have been found in the present study in UTH, where UTH is increasing in the first year of abrupt4xCO2 in the eastern equatorial Pacific as well as in parts of the winter dry belt in the Northern Hemisphere. Parts of the change in UTH can therefore be

attributed to the direct effect of the greenhouse gas, but the comparison between Figure 5.6 and 5.20 shows also, that the thermodynamic effect largely influences the UTH distribution after 150 years of the model run.

The model data analysis of UTH was completed by looking at two other CMIP5 model datasets, which have been used to compute the brightness temperature with COSP and RTTOV and to calculate UTH with the brightness temperature transformation method. This comparison has shown, that the trends for UTH from MPI-ESM lie within the same range as from CNRM or BCC and have generally the same sign. But while the extension and intensity of the dry zones in the upper troposphere are considerably smaller in BCC, UTH from CNRM presents some common structures with MPI-ESM notably the poleward expansion of the subtropical subsidence zones and the weakening of the dry zone located at the eastern flank of the North Pacific Subtropical Anticyclone. This last trend can also be found to a smaller extent in BCC. Nevertheless, the main results of the present study are coming from one model only (MPI-ESM). Therefore, the results should not be overvalued and a next step could be to analyse UTH from a model ensemble, in order to increase the significance of the results.

The trends found in the model data have been finally compared to those found in observation data. The observation data originates from the microwave humidity dataset from the Advanced Microwave Sounding Unit-B (AMSU-B) instruments, on board the NOAA15 and NOAA16 satellites. AMSU-B is a five channel microwave radiometer which is designed for measurements of tropospheric humidity. For the last part of the study infrared humidity data has also been used, originating from the High-resolution Infrared Radiation Sounder (HIRS). The general structures of the dry zones found in the observation data of AMSU-B are similar to the one visualized in the model data. Although the time series of AMSU-B data is too short for real climate trend studies, the evolution of UTH in the 17 years has been analysed in comparison with the found trends in the model data. In Northern Hemisphere, a poleward expansion of the subsidence zones in winter has been found in the observation data. In Southern Hemisphere, nearly no shift in the edge of the dry zones could be identified. The second category of dry zones found in the model data, the dry descent regions of the Subtropical Anticyclones, are well discernible in UTH from microwave data, but reveal no clear or common trend in the 17 measurement years. Where the North Pacific descent region is moistening in the model data, the observation data reveals a drying trend in upper troposphere.

The general trends calculated from microwave and infrared satellite data show decreasing trends in UTH for all hemispheres and all seasons, but with low significances. Consistent with these results, the trends in frequency of occurrence of UTH smaller than 30 % (Microwave) and 10 % (Infrared) are positive, even though none

of these trends has been found to be significant. Only more years of measurements will help to increase the significance of trends and reveal how UTH and the dry zones will change due to the increase in greenhouse gases.

The results presented in this thesis are only a glimpse of what could or what is happening in upper troposphere with increasing greenhouse gases. Many open questions subsist and it is not clear by now, to what extent water vapour feedback in the changing dry zones will impact climate change. To further investigate this question, it would be interesting to analyse UTH and the dry zones with the help of a whole ensemble mean, in order to eliminate the residuals due to the caprices of one model. In the context of this master thesis, processing the model data with the satellite simulation software was too time-consuming to extend it over the whole ensemble mean of CMIP5. But the present analysis can therefore only be seen as a first step in the study of UTH with model data. Only with the whole ensemble mean, the results and trends can possibly be significant.

Observations with satellite data will also in future be a valuable source of information about upper tropospheric moisture and dry zones. The time series of infrared sensor measurements are already long enough to speak of climate trends. Unfortunately measurements with infrared sounders are more influenced by clouds than microwave sounders. Therefore, it is worth to wait for longer measurement times series of microwave sounders, in order to perform a more significant trend analysis of UTH and upper tropospheric dry zones.

Appendices

Appendix A

CMIP5 Models

Modeling Groups and their Terms of Use

The “official” model and group names given in the table below should be used in all presentations and publications (e.g., in tables and figure legends).

Output from yellow highlighted models is available for unrestricted use. Output from the others may only be used for non-commercial research and educational purposes. [See complete “Terms of Use”: <http://cmip-pcmdi.llnl.gov/cmip5/terms.html>]

Modeling Center (or Group)	Institute ID	Model Name
Commonwealth Scientific and Industrial Research Organization (CSIRO) and Bureau of Meteorology (BOM), Australia	CSIRO-BOM	ACCESS1.0 ACCESS1.3
Beijing Climate Center, China Meteorological Administration	BCC	BCC-CSM1.1 BCC-CSM1.1(m)
Instituto Nacional de Pesquisas Espaciais (National Institute for Space Research)	INPE	BESM OA 2.3*
College of Global Change and Earth System Science, Beijing Normal University	GCESS	BNU-ESM
Canadian Centre for Climate Modelling and Analysis	CCCMA	CanESM2 CanCM4 CanAM4
University of Miami - RSMAS	RSMAS	CCSM4(RSMAS)*
National Center for Atmospheric Research	NCAR	CCSM4
Community Earth System Model Contributors	NSF-DOE-NCAR	CESM1(BGC) CESM1(CAM5) CESM1(CAM5.1,FV2) CESM1(FASTCHEM) CESM1(WACCM)
Center for Ocean-Land-Atmosphere Studies and National Centers for Environmental Prediction	COLA and NCEP	CFSv2-2011
Centro Euro-Mediterraneo per I Cambiamenti Climatici	CMCC	CMCC-CESM CMCC-CM CMCC-CMS
Centre National de Recherches Météorologiques / Centre Européen de Recherche et Formation Avancée en Calcul Scientifique	CNRM-CERFACS	CNRM-CM5
		CNRM-CM5-2
Commonwealth Scientific and Industrial Research Organization in collaboration with Queensland Climate Change Centre of Excellence	CSIRO-QCCCE	CSIRO-Mk3.6.0
EC-EARTH consortium	EC-EARTH	EC-EARTH
LASG, Institute of Atmospheric Physics, Chinese Academy of Sciences and CESS, Tsinghua University	LASG-CESS	FGOALS-g2

* Model output not yet available.

LASG, Institute of Atmospheric Physics, Chinese Academy of Sciences	LASG-IAP	FGOALS-g1 FGOALS-s2
The First Institute of Oceanography, SOA, China	FIO	FIO-ESM
NASA Global Modeling and Assimilation Office	NASA GMAO	GEOS-5
NOAA Geophysical Fluid Dynamics Laboratory	NOAA GFDL	GFDL-CM2.1 GFDL-CM3 GFDL-ESM2G GFDL-ESM2M GFDL-HIRAM-C180 GFDL-HIRAM-C360
NASA Goddard Institute for Space Studies	NASA GISS	GISS-E2-H GISS-E2-H-CC GISS-E2-R GISS-E2-R-CC
National Institute of Meteorological Research/Korea Meteorological Administration	NIMR/KMA	HadGEM2-AO
Met Office Hadley Centre (additional HadGEM2-ES realizations contributed by Instituto Nacional de Pesquisas Espaciais)	MOHC (additional realizations by INPE)	HadCM3 HadGEM2-CC HadGEM2-ES HadGEM2-A
Institute for Numerical Mathematics	INM	INM-CM4
Institut Pierre-Simon Laplace	IPSL	IPSL-CM5A-LR IPSL-CM5A-MR IPSL-CM5B-LR
Japan Agency for Marine-Earth Science and Technology, Atmosphere and Ocean Research Institute (The University of Tokyo), and National Institute for Environmental Studies	MIROC	MIROC-ESM MIROC-ESM-CHEM
Atmosphere and Ocean Research Institute (The University of Tokyo), National Institute for Environmental Studies, and Japan Agency for Marine-Earth Science and Technology	MIROC	MIROC4h MIROC5
Max-Planck-Institut für Meteorologie (Max Planck Institute for Meteorology)	MPI-M	MPI-ESM-MR MPI-ESM-LR MPI-ESM-P
Meteorological Research Institute	MRI	MRI-AGCM3.2H MRI-AGCM3.2S MRI-CGCM3 MRI-ESM1
Nonhydrostatic Icosahedral Atmospheric Model Group	NICAM	NICAM.09
Norwegian Climate Centre	NCC	NorESM1-M NorESM1-ME

Appendix B

COSP Namelists

B.1 COSP Input Namelist

```
! (c) British Crown Copyright 2008, the Met Office.
! All rights reserved.
!
! Redistribution and use in source and binary forms, with or without
! modification, are permitted provided that the following conditions
! are met:
!     * Redistributions of source code must retain the above
!     copyright notice, this list of conditions and the following disclaimer.
!     * Redistributions in binary form must reproduce the above
!     copyright notice, this list conditions and the following disclaimer in
!     the documentation and/or other materials provided with the distribution.
!     * Neither the name of the Met Office nor the names of its
!     contributors may be used to endorse or promote products derived from
!     this software without specific prior written permission.
!
! THIS SOFTWARE IS PROVIDED BY THE COPYRIGHT HOLDERS AND
! CONTRIBUTORS "AS IS" AND ANY EXPRESS OR IMPLIED WARRANTIES, INCLUDING,
! BUT NOT LIMITED TO, THE IMPLIED WARRANTIES OF MERCHANTABILITY AND
! FITNESS FOR A PARTICULAR PURPOSE ARE DISCLAIMED. IN NO EVENT SHALL THE
! COPYRIGHT OWNER OR CONTRIBUTORS BE LIABLE FOR ANY DIRECT, INDIRECT,
! INCIDENTAL, SPECIAL, EXEMPLARY, OR CONSEQUENTIAL DAMAGES (INCLUDING,
! BUT NOT LIMITED TO, PROCUREMENT OF SUBSTITUTE GOODS OR SERVICES; LOSS
! OF USE, DATA, OR PROFITS; OR BUSINESS INTERRUPTION) HOWEVER CAUSED AND
! ON ANY THEORY OF LIABILITY, WHETHER IN CONTRACT, STRICT LIABILITY, OR
! TORT (INCLUDING NEGLIGENCE OR OTHERWISE) ARISING IN ANY WAY OUT
! OF THE USE OF THIS SOFTWARE, EVEN IF ADVISED OF THE POSSIBILITY OF
! SUCH DAMAGE.
!
! Namelist that sets up the main COSP options
! Parameters that define the model grid need to be defined appropriately by
! the modellers (NPOINTS,NLEVELS).
! NCOLUMNS is recommended to be ~ model resolution (in degrees) x 100
! (e.g 1x1 deg model => NCOLUMN=100)
```

```

&COSP_INPUT
CMOR_NL='./TBMiTi/cosp_cmor_rttov_01.txt', ! CMOR rttov namelist
NPOINTS=32768,! Number of gridpoints 153,27840,7081,6912
NPOINTS_IT=50,! Max number of gridpoints to be processed in one iteration
NCOLUMNS=10, ! Number of subcolumns
NLEVELS=17, ! Number of model levels
USE_VGRID=.true., ! Use fixed vertical grid for outputs?
! (if .true. then you need to define number of levels with Nlr)
NLR=19, ! Number of levels in statistical outputs (only used if
USE_VGRID=.true.)
CSAT_VGRID=.true., ! CloudSat vertical grid? (if .true. then the CloudSat
standard grid is used for the outputs.
! USE_VGRID needs also be .true.)
DINPUT='/scratch/uni/u237/user_data/mtivig/INPUT/CNRM-CM5_1pctCO2/',
! Directory where the input files are located. Useful when processing
multiple files.
! Leave blank (') if you are using the full path in FINPUT.
FINPUT='CNRM-CM5-2_COSP_INPUT195001.nc',
'CNRM-CM5-2_COSP_INPUT195002.nc',
'CNRM-CM5-2_COSP_INPUT195003.nc',
'CNRM-CM5-2_COSP_INPUT195004.nc',
'CNRM-CM5-2_COSP_INPUT195005.nc',
'CNRM-CM5-2_COSP_INPUT195006.nc',
'CNRM-CM5-2_COSP_INPUT195007.nc',
!List input NetCDF files

!-----
!----- Inputs related to radar simulations
!-----

RADAR_FREQ=94.0, ! CloudSat radar frequency (GHz)
SURFACE_RADAR=0, ! surface=1, spaceborne=0
use_mie_tables=0,! use a precomputed lookup table? yes=1,no=0
use_gas_abs=0, ! include gaseous absorption? yes=1,no=0
do_ray=0, ! calculate/output Rayleigh refl=1, not=0
melt_lay=0, ! melting layer model off=0, on=1
k2=-1, ! |K|^2, -1=use frequency dependent default
use_reff=.true., ! True if you want effective radius to be used by
! radar simulator (always used by lidar)
use_precipitation_fluxes=.false., ! True if precipitation fluxes are
! input to the algorithm

!-----
!----- Inputs related to lidar simulations
!-----

Nprmts_max_hydro=12, ! Max number of parameters for hydrometeor size
! distributions
Naero=1, ! Number of aerosol species (Not used)
Nprmts_max_aero=1, ! Max number of parameters for aerosol size
! distributions (Not used)

```

```

lidar_ice_type=0,    ! Ice particle shape in lidar calculations
(0=ice-spheres ; 1=ice-non-spherical)
OVERLAP=3,    ! overlap type: 1=max, 2=rand, 3=max/rand
!-----
!----- Inputs related to ISCCP simulator
!-----
ISCCP_TOPHEIGHT=1, ! 1 = adjust top height using both a computed
! infrared brightness temperature and the visible
! optical depth to adjust cloud top pressure. Note
! that this calculation is most appropriate to compare
! to ISCCP data during sunlit hours.
! 2 = do not adjust top height, that is cloud top
! pressure is the actual cloud top pressure
! in the model
! 3 = adjust top height using only the computed
! infrared brightness temperature. Note that this
! calculation is most appropriate to compare to ISCCP
! IR only algorithm (i.e. you can compare to nighttime
! ISCCP data with this option)
ISCCP_TOPHEIGHT_DIRECTION=1,
! direction for finding atmosphere pressure level
! with interpolated temperature equal to the radiance
! determined cloud-top temperature
! 1 = find the *lowest* altitude (highest pressure) level
! with interpolated temperature equal to the radiance
! determined cloud-top temperature
! 2 = find the *highest* altitude (lowest pressure) level
! with interpolated temperature equal to the radiance
! determined cloud-top temperature. This is the
! default value since V4.0 of the ISCCP simulator.
! ONLY APPLICABLE IF top_height EQUALS 1 or 3
!-----
!----- RTTOV inputs
!-----
Platform=1,    ! satellite platform
Satellite=15, ! satellite
Instrument=4,  ! instrument
Nchannels=5,  ! Number of channels to be computed
Channels=1,2,3,4,5 ! Channel numbers (please be sure that you
! supply Nchannels)
Surfem=0.0,0.0,0.0,0.0,0.0 ! Surface emissivity (please be sure that
! you supply Nchannels)
ZenAng=0.55, ! Satellite Zenith Angle
CO2=5.241e-04, ! Mixing ratios of trace gases
CH4=9.139e-07,
N2O=4.665e-07,
CO=2.098e-07
/

```

B.2 COSP Output Namelist

```
! (c) British Crown Copyright 2008, the Met Office.
! All rights reserved.
!
! Redistribution and use in source and binary forms, with or without
! modification, are permitted provided that the following conditions
! are met:
!     * Redistributions of source code must retain the above copyright
! notice, this list of conditions and the following disclaimer.
!     * Redistributions in binary form must reproduce the above copyright
! notice, this list of conditions and the following disclaimer in the
! documentation and/or other materials provided with the distribution.
!     * Neither the name of the Met Office nor the names of its
! contributors may be used to endorse or promote products derived from
! this software without specific prior written permission.
!
! THIS SOFTWARE IS PROVIDED BY THE COPYRIGHT HOLDERS AND CONTRIBUTORS
! "AS IS" AND ANY EXPRESS OR IMPLIED WARRANTIES, INCLUDING, BUT NOT
! LIMITED TO, THE IMPLIED WARRANTIES OF MERCHANTABILITY AND FITNESS FOR
! A PARTICULAR PURPOSE ARE DISCLAIMED. IN NO EVENT SHALL THE COPYRIGHT
! OWNER OR CONTRIBUTORS BE LIABLE FOR ANY DIRECT, INDIRECT, INCIDENTAL,
! SPECIAL, EXEMPLARY, OR CONSEQUENTIAL DAMAGES (INCLUDING, BUT NOT LIMITED
! TO, PROCUREMENT OF SUBSTITUTE GOODS OR SERVICES; LOSS OF USE, DATA, OR
! PROFITS; OR BUSINESS INTERRUPTION) HOWEVER CAUSED AND ON ANY THEORY
! OF LIABILITY, WHETHER IN CONTRACT, STRICT LIABILITY, OR TORT (INCLUDING
! NEGLIGENCE OR OTHERWISE) ARISING IN ANY WAY OUT OF THE USE OF THIS
! SOFTWARE, EVEN IF ADVISED OF THE POSSIBILITY OF SUCH DAMAGE.
!
! History:
! May 2009 - A. Bodas-Salcedo - Initial version
! Dec 2009 - A. Bodas-Salcedo - v1.2
! Dec 2010 - A. Bodas-Salcedo - v1.3.1
!
! Namelist that sets up output-related variables.
! These are variables requested for CFMIP-2.
! ISCCP and CALIPSO/PARASOL simulators ON, to be run inline.
! Gridded outputs on daily/monthly timescales from model gridded data.
&COSP_OUTPUT
! Simulator flags
Lradar_sim=.false.,
Llidar_sim=.false.,
Lisccp_sim=.false.,
Lmisr_sim=.false.,
Lmodis_sim=.false.,
Lrttov_sim=.true.,
! Output variables
!- Variables unique in 1D (curtain) mode
```

```

Ltoffset=.false.,
!- CloudSat
Lcfaddbze94=.false.,
Ldbze94=.false.,
!- CALIPSO
Latb532=.false.,
LcfadLidarsr532=.false.,
Llcalipso=.false.,
Llhalipso=.false.,
Lllcalipso=.false.,
Llmcipso=.false.,
Llcalipso=.false.,
LparasolRefl=.false.,
!- ISCCP
Lalbiscpp=.false.,
Lboxtopisccp=.false.,
Lboxtauisccp=.false.,
Lpctisccp=.false.,
Lclisccp=.false.,
Ltauisccp=.false.,
Llcalisccp=.false.,
Lmeantbiscpp=.false.,
Lmeantbclrisccp=.false.,
!- MISR
LlMISR=.false.,
!- Use lidar and radar
Llcalipso2=.false.,
Llclidarradar=.false.,
!- These are provided for debugging or special purposes
Lfracout=.false.,
LlidarBetaMol532=.false.,
!- MODIS
Llcalmodis=.false.,
Llclmodis=.false.,
Lllmodis=.false.,
Llclhmodis=.false.,
Llclmmodis=.false.,
Llclllmodis=.false.,
Llclautmodis=.false.,
Llclawmodis=.false.,
Llclauimodis=.false.,
Llclautlogmodis=.false.,
Llclawlogmodis=.false.,
Llclaulogmodis=.false.,
Llclreffclwmodis=.false.,
Llclreffclimodis=.false.,
Llclpctmodis=.false.,
Llclwpmmodis=.false.,

```

```

Liwpmadis=.false.,
Lclmodis=.false.,
!- RTTOV
Ltbrrttov=.true.,
/

```

B.3 COSP cmor Namelist

```

! (c) British Crown Copyright 2008, the Met Office.
! All rights reserved.
!
! Redistribution and use in source and binary forms, with or without
! modification, are permitted provided that the following conditions
! are met:
!   * Redistributions of source code must retain the above copyright
!   notice, this list of conditions and the following disclaimer.
!   * Redistributions in binary form must reproduce the above copyright
!   notice, this list of conditions and the following disclaimer in the
!   documentation and/or other materials provided with the distribution.
!   * Neither the name of the Met Office nor the names of its
!   contributors may be used to endorse or promote products derived from
!   this software without specific prior written permission.
!
! THIS SOFTWARE IS PROVIDED BY THE COPYRIGHT HOLDERS AND CONTRIBUTORS
! "AS IS" AND ANY EXPRESS OR IMPLIED WARRANTIES, INCLUDING, BUT NOT
! LIMITED TO, THE IMPLIED WARRANTIES OF MERCHANTABILITY AND FITNESS FOR
! A PARTICULAR PURPOSE ARE DISCLAIMED. IN NO EVENT SHALL THE COPYRIGHT
! OWNER OR CONTRIBUTORS BE LIABLE FOR ANY DIRECT, INDIRECT, INCIDENTAL,
! SPECIAL, EXEMPLARY, OR CONSEQUENTIAL DAMAGES (INCLUDING, BUT NOT LIMITED
! TO, PROCUREMENT OF SUBSTITUTE GOODS OR SERVICES; LOSS OF USE, DATA, OR
! PROFITS; OR BUSINESS INTERRUPTION) HOWEVER CAUSED AND ON ANY THEORY
! OF LIABILITY, WHETHER IN CONTRACT, STRICT LIABILITY, OR TORT (INCLUDING
! NEGLIGENCE OR OTHERWISE) ARISING IN ANY WAY OUT OF THE USE OF THIS
! SOFTWARE, EVEN IF ADVISED OF THE POSSIBILITY OF SUCH DAMAGE.
!
! History:
! May 2009 - A. Bodas-Salcedo - Initial version
! Dec 2009 - A. Bodas-Salcedo - v1.2
! Dec 2010 - A. Bodas-Salcedo - v1.3.1
!
!!!!!! Namelist that sets up CMOR-related variables.
! Configuration for CFMIP-2.
! ISCCP and CALIPSO/PARASOL simulators ON, to be run inline.
! Gridded outputs on daily/monthly timescales from model gridded data.
! Please fill the fields To Be Filled (TBF)
&CMOR
INPATH = './TBMiTi',
OUTPATH = './outputs',

```

```
START_DATE = '16.01.1950',
MODEL_ID = 'CNRM-CM5',
EXPERIMENT_ID = '1pctCO2',
BRANCH_TIME=0.,
PARENT_EXPERIMENT_ID='N/A',
PARENT_EXPERIMENT_RIP='N/A',
FORCING='GHG',
INSTITUTION = 'CNRM',
INSTITUTE_ID='CNRM',
SOURCE = 'CNRM-CM5-2',
CALENDAR = 'gregorian',
REALIZATION = 1,
INITIALIZATION_METHOD = 1,
PHYSICS_VERSION = 1,
CONTACT = 'MTivig',
HISTORY = '04 Oct 2016',
COMMENT = '/',
REFERENCES = '/',
TABLE = 'COSP_table_2D', !CMIP5_cfDay/CMIP5_cfMon
MAXTSTEPS = 10000
/
```

Appendix C

First Decade of abrupt4xCO2 and 1pctCO2

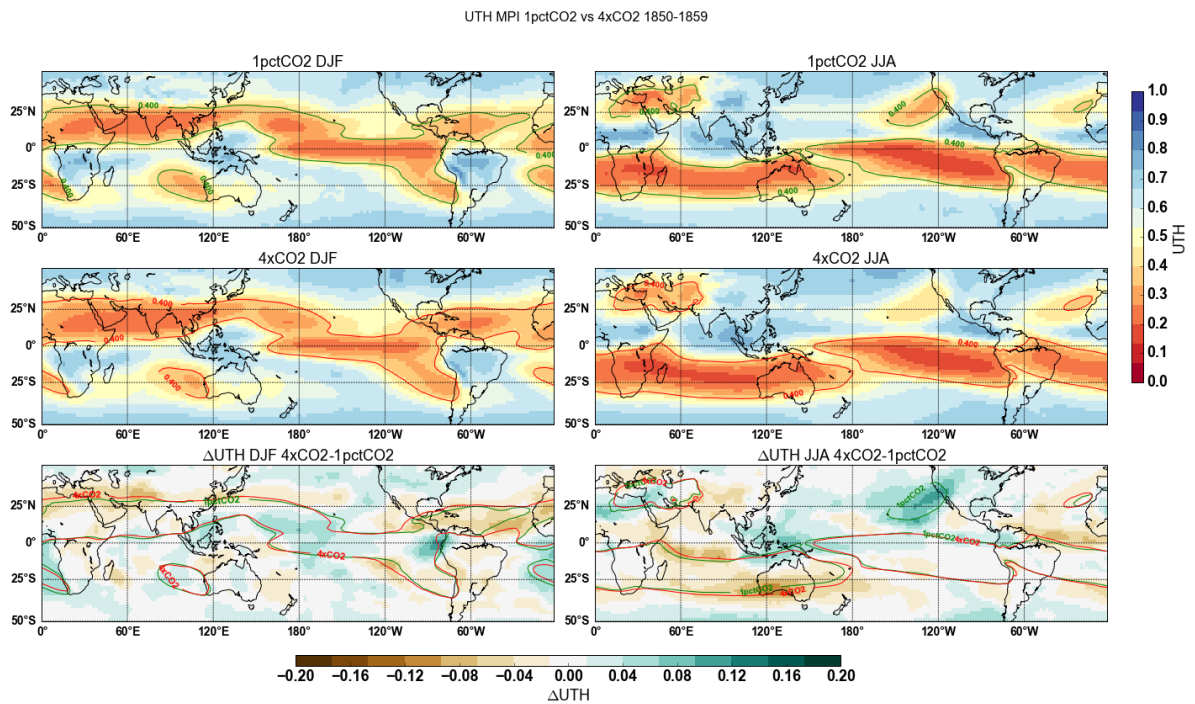


Figure C.1: Decadal mean of UTH in the 1pctCO2 run (top) and in the abrupt4xCO2 (middle) model run for the first decade (1850-1859) for January, February and December (left) and June to August (right). The bottom plots show the difference between the two experiments.

Bibliography

- Ban, K.-M. (2008): Secretary-General Ban Ki-Moon's Opening Statement to the High Level Segment of the United Nations Climate Change Conference (COP 14) in Poznan, Poland, December 11th, 2008.
https://unfccc.int/files/meetings/cop_14/statements/application/pdf/cop_14_statement_ban_ki_moon.pdf, Last viewed on January the 26th, 2017.
- Bates J.J. and Jackson D. L. (2001): Trends in upper tropospheric humidity. *Geophysical Research Letters*, Vol. 28, No. 9, 1695-1698.
- Bates J. J., Jackson D. L., Breon F.-M. and Bergen Z. D. (2001): Variability of tropical upper tropospheric humidity 1979-1998. *Journal of Geophysical Research*, Vol. 106, No. D23, 32271-32281.
- Birner T., Davis S. M. and Seidel D. J. (2014): The changing width of Earth's tropical belt. *Physics Today*, No. 67, 12.
- Bjerknes J. (1969): Atmospheric teleconnections from the equatorial Pacific. *Monthly Weather Review* 97, 163-172.
- Bodas-Salcedo A., (2010): COSP user's manual, Version 1.3. Met Office Hadley Centre.
- Bodas-Salcedo A., Webb M. J., Bony S., Chepfer H., Dufresne J.-L., Klein S.A., Zhang Y., Marchand R., Haynes J.M., Pincus R. and John V.O. (2011): COSP - Satellite simulation software for model assessment. *American Meteorological Society*, 1023-1043.
- Bony S., Colman R., Kattsov V. M., Allan R. P., Bretherton C. S., Dufresne J.-L., Hall A., Hallegatte S., Holland M. M., Ingram W., Randall D. A., Soden B. J. and Tselioudis G. (2006): How Well Do We Understand and Evaluate Climate Change Feedback Processes? *Journal of Climate*, Vol. 19, 3445-3482.
- Bony S., Bellon G., Klocke D., Sherwood S., Fermepin S. and Devil S. (2013): Robust Direct Effect of Carbon Dioxide on Tropical Circulation and Regional Precipitation. *Nature Geoscience*, Vol. 6, 447-451.

- Brogniez H., Roca R. and Picon L. (2005): Evaluation of the distribution of subtropical free tropospheric humidity in AMIP-2 simulations using METEOSAT water vapor channel data. *Geophysical Research Letters*, Vol. 32.
- Brogniez H., Clain G. and Roca R. (2015): Validation of Upper-Tropospheric Humidity from SAPHIR on board Megha-Tropiques Using Tropical Soundings. *Journal of Applied Meteorology and Climatology*, Vol. 54, 896-908.
- Brönnimann S., Fischer A. M., Rozanov E., Poli P., Compo G. P. and Sardeshmukh P. D. (2015): Southward Shift of the Northern Tropical Belt from 1945 to 1980. *Nature Geosciences* Vol. 8.
- Buehler S. A., Kuvatov M., Sreerekha T. R., John V. O., Rydberg B., Eriksson P. and Notholt J. (2007): A Cloud Filtering method for microwave upper tropospheric humidity measurements. *Atmospheric Chemistry and Physics*, Vol. 7, No. 21, 5531-5542.
- Buehler S. A., Kuvatov M., John V. O., Milz M., Soden B. J., Jackson D. L. and Notholt J. (2008): An upper tropospheric humidity data set from operational satellite microwave data. *Journal of Geophysical Research*, Vol. 113.
- Buehler S. A. and John V. O. (2005): A simple method to relate microwave radiances to upper troposphere humidity. *Journal of Geophysical Research*, Vol. 110.
- Cai W., Cowan T. and Thatcher M. (2012): Rainfall reductions over Southern Hemisphere semi-arid regions: the role of subtropical dry zone expansion. *Scientific Reports*, 2:702.
- Chung E.-S., Soden B. J., Sohn B.-J. and Schmetz J. (2011): Model-simulated humidity bias in the upper troposphere and its relation to the large-scale circulation. *Journal of Geophysical Research*, Vol. 116.
- Chung E.-S., Soden B. J. and John V. O. (2013): Intercalibrating Microwave Satellite Observations for Monitoring Long-Term Variations in Upper-Tropospheric Water Vapor. *Journal of Atmospheric and Oceanic Technology*, Vol. 30, 2303-2319.
- Colman R.A. (2001): On the Vertical Extent of Atmospheric Feedbacks. *Climate Dynamics*, Vol. 17, 391-405.
- The Comet Program, Laing Dr. A. , Evans Dr. J.-L. (2011): Introduction to Tropical Meteorology. [http : //www.goes - r.gov/users/comet/tropical/textbook2ndedition/print1.htm](http://www.goes-r.gov/users/comet/tropical/textbook2ndedition/print1.htm), Last viewed on May, 2nd 2016, at 11:00 AM.

- Cook B. I. and Seager R. (2013): The response of the North American Monsoon to increased greenhouse gas forcing. *Journal of Geophysical Research: Atmospheres*, Vol. 118, 16901699.
- Davis R. E., Hayden B. P., Gay D. A., Philips W. L. and Jones G. V. (1996): The North Atlantic Subtropical Anticyclone. *Journal of Climate*, Vol. 10, 728-744.
- Del Genio A. D., Kovari W. and Yao M.-S. (1994): Climatic implications of the seasonal variation of upper troposphere water vapor. *Geophysical Research Letters*, Vol. 21, No. 24, 2701-2704.
- Dessler A. E. and Sherwood S. C. (2000): Simulations of tropical upper tropospheric humidity. *Journal of Geophysical Research*, Vol. 105, No. D15, 20155-20163.
- Deutscher Wetterdienst Wetterlexikon.
<https://www.dwd.de/DE/service/lexikon/Functions/glossar.html>,
 Last viewed on November the 17th, 2016, at 21:00.
- Dima I. M. and Wallace J. M. (2003) On the Seasonality of the Hadley cell. *Journal of the Atmospheric Sciences*, Vol. 60, 1522-1527.
- Elliot W. P. and Gaffen D. J. (1991): On the Utility of Radiosonde Humidity Archives for Climate Studies. *Bulletin American Meteorological Society*, Vol. 72, No. 10, 1507-1520.
- Emori S., Taylor K., Hewitson B., Zermoglio F., Jukes M., Lautenschlager M. and Stockhause M. (2016): CMIP5 data provided at the IPCC Data Distribution Centre. Fact Sheet of the Task Group on Data and Scenario Support for Impact and Climate Analysis (TGICA) of the Intergovernmental Panel on Climate Change (IPCC), 8 pp.
- English S. J. and Hewison T. J. (1998): A fast generic millimetre-wave emissivity model. SPIE Proceedings, Microwave Remote Sensing of the Atmosphere and Environment, Vol. 3503.
- Gottelman A., Collins W. D., Fetzer E. J., Eldering A., Irion F. W., Duffy P. F. and Bala G. (2006): Climatology of Upper-Tropospheric Relative Humidity from the Atmospheric Infrared Sounder and Implications for Climate. *Journal of Climate*, Vol. 19(23), 6104-6121.
- Gottelman A., Hegglin M. I., Son S.-W., Fujiwara M., Tilmes S., Pan L., Hoor P., Lee H., Manney G. L., Birner T., Stiller G., Rex M., Kremser S., Wuebbles D., Walker K. A. and Anel J. A. (2010): Chapter 7: Upper Troposphere and Lower

- Stratosphere. In: *WMO/ICSU/IOC World Climate Research Programme: Stratospheric Processes and their Role in Climate. SPARC Report on the Evaluation of Chemistry-Climate Models*. WCRP 132, WMO/TD No. 1526, SPARC Report No. 5.
- Gettelman A. and Fu Q. (2008): Observed and Simulated Upper-Tropospheric Water Vapor Feedback. *Journal of Climate*, Vol. 21, 3282-3289.
- Gierens K., Eleftheratos K. and Shi L. (2014): Technical Note: 30 years of HIRS data of upper tropospheric humidity. *Atmospheric Chemistry and Physics*, Vol. 14, 7533-7541.
- Gierens K. and Eleftheratos K. (2015): Upper-tropospheric humidity changes under constant relative humidity. *Atmospheric Chemistry and Physics*, Vol. 15, 29497-29521.
- Giorgetta M. A., Jungclaus J., Reick C. H., Legutke S., Bader J., Böttinger M., Brovkin V., Cruieger T., Esch M., Fieg K., Glushak K., Gayler V., Haak H., Hollweg H.-D., Ilyina T., Kinne S., Kornblueh L., Matei D., Mauritsen T., Mikolajewicz U., Mueller W., Notz D., Pithan F., Raddatz T., Rast S., Redler R., Roeckner E., Schmidt H., Schnur R., Segschneider J., Six K. D., Stockhause M., Timmreck C., Wegner J., Widmann H., Wieners K.-H., Claussen M., Marotzke J. and Stevens B. (2013): Climate and carbon cycle changes from 1850 to 2100 in MPI-ESM simulations for the Coupled Model Intercomparison Project phase 5. *Journal of advances in modeling earth systems*, Vol. 5, 572-597.
- He J. and Soden B. (2015): Anthropogenic Weakening of the Tropical Circulation: The Relative Roles of Direct CO₂ Forcing and Sea Surface Temperature Change. *Journal of climate*, Vol. 28, 8728-8742.
- He J. and Soden B. J. (2016): A re-examination of the projected subtropical precipitation decline. *Nature Climate Change*, Vol. 7, 53-57.
- Held I. M., Hemler R. S. and Ramaswamy V. (1993): Radiative convective equilibrium with explicit two-dimensional moist convection. *Journal of the Atmospheric Sciences*, Vol. 50, No. 23, 3909-3927.
- Held I. M. and Soden B. J. (2000): Water vapor feedback and global warming. *Annual Review of Energy and the Environment*, Vol. 25, 441-475.
- Held I. M. and Soden B. J. (2006): Robust Responses of the Hydrological Cycle to Global Warming. *Journal of Climate*, Vol. 19, 5686-1560.

- Hennemuth B., Bender S., Blow K., Dreier N., Keup-Thiel E., Krger O., Mudersbach C., Radermacher C., Schoetter R. (2013): Statistische Verfahren zur Auswertung von Klimadaten aus Modell und Beobachtung, eingesetzt in Projekten und Institutionen, die sich mit Klimafolgen und Anpassung befassen. CSC Report 13, Climate Service Center, Germany.
- Hu Y., Zhou C. and Liu J. (2011): Observational Evidence for Poleward Expansion of the Hadley Circulation. *Advances in Atmospheric Sciences* Vol. 28, 33-44.
- Hu Y. and Fu Q. (2007): Observed poleward expansion of the Hadley circulation since 1979. *Atmospheric Chemistry and Physics*, Vol. 7, 52295236.
- Ilyina T., Six K. D., Segschneider J., Maier-Reimer E., Li H., and Núñez-Riboni I. (2013): Global ocean biogeochemistry model HAMOCC: Model architecture and performance as component of the MPI-Earth System Model in different CMIP5 experimental realizations. *Journal of Advances in Modeling Earth Systems*, Vol. 5, 287315.
- Intergovernmental Panel on Climate change (IPCC) (2007): Climate Change 2007: The Physical Science Basis. Contribution of Working Group I to the Fourth Assessment Report of the Intergovernmental Panel on Climate Change. ed. S. Solomon, D. Qin, M. Manning, Z. Chen, M. Marquis, K. Averyt, M.M.B Tignor, H.L. Miller Jr, and Z. Chen. 996 pp. Cambridge University Press.
- IPCC (2013): Climate Change 2013: The Physical Science Basis. Contribution of Working Group I to the Fifth Assessment Report of the Intergovernmental Panel on Climate Change. Stocker, T.F., D. Qin, G.-K. Plattner, M. Tignor, S.K. Allen, J. Boschung, A. Nauels, Y. Xia, V. Bex and P.M. Midgley (eds.), *Cambridge University Press*, Cambridge, United Kingdom and New York, NY, USA, 1535 pp.
- Johanson C. M. and Fu Q. (2009): Hadley Cell Widening: Model Simulations versus Observations. *American Meteorological Society*, Vol. 22, 2713-2725.
- John V. O., Holl G., Allan R. P., Buehler S. A., Parker D. E. and Soden B. (2011): Clear-sky biases in satellite infrared estimates of upper tropospheric humidity and its trends. *Journal of Geophysical Research: Atmospheres*, Vol. 116, Issue D14.
- John V. O., Allan R. P., Bell W., Buehler S. A. and Kottayil A. (2013): Assessment of intercalibration methods for satellite microwave humidity sounders. *Journal of Geophysical Research: Atmospheres*, Vol. 118, No. 10, 4906.

- Junglclaus H., Fischer N., Haak H., Lohmann K., Marotzke J., Matei D., Mikolajewicz U., Notz D. and von Storch J. S. (2013): Characteristics of the ocean simulations in the Max Planck Institute Ocean Model (MPIOM) the ocean component of the MPI-Earthsystem model. *Journal of advances in modeling earth systems*, Vol. 5, 422446.
- Jury M. R. and Winter A. (2009): Warming of an elevated layer over the Caribbean. *Climatic Change*.
- Kraus H. (2004): Die Atmosphäre: eine Einführung in die Meteorologie. Springer Verlag, 3d edition.
- Lau W. K. M. and Kim K.-M. (2015): Robust Hadley Circulation changes and increasing global dryness due to CO₂ warming from CMIP5 model projections. PNAS vol. 112, No. 12, 3630-3635.
- Lau K. M. and Yang S. (2002): Walker Circulation. Elsevier Science Ltd.
- Li W., Li L., Ting M. and Liu Y. (2012): Intensification of Northern Hemisphere subtropical highs in a warming climate. *Nature Geoscience* Vol. 5, 830-834.
- Li W., Li L., Ting M., Deng J., Kushnir Y., Liu Y., Lu Y., Wang C. and Zhang P. (2013): Intensification of the Southern Hemisphere summertime Subtropical Anticyclones in a warming climate. *Geophysical Research Letters*, Vol. 40, 5959-5964.
- Lindzen R.S. (1990): Some Coolness Concerning Global Warming. *Bulletin American Meteorological Society*, Vol. 71, No. 3, 288-299.
- Lindzen R. S., Chou M.-D. and Hou A. Y. (2001): Does the Earth Have an Adaptive Infrared Iris? *Bulletin of the American Meteorological Society*, Vol. 82, No. 3, 417-432.
- Lu J., Vecchi G. A., Reichler T. (2007): Expansion of the Hadley cell under global warming. *Geophysical Research Letters*, Vol. 34.
- Lu J., Deser C. and Reichler T. (2009): Cause of the widening of the tropical belt since 1958. *Geophysical Research Letters*, Vol. 36, L03803.
- Malberg H. (2007): Meteorologie und Klimatologie. Eine Einführung. 5th edition, Springer Verlag, 2007.
- Manabe S. and Strickler R. F. (1964): Thermal Equilibrium of the Atmosphere with Convective Adjustment. *Journal of Atmospheric Sciences*, Vol. 21, 361-385.

- Manabe S. and Wetherald R. T. (1967): Thermal Equilibrium of the Atmosphere with a Given Distribution of Relative Humidity. *Journal of the Atmospheric Sciences*, Vol. 24, No. 3, 241-259.
- Milz M, Buehler S. A. and John V.O. (2009): Comparison of AIRS and AMSU-B monthly mean estimates of upper tropospheric humidity. *Geophysical Research Letters*, Vol. 36, L10804.
- Minschwaner K. and Dessler A. F. (2004): Water Vapor Feedback in the Tropical Upper Troposphere. Model Results and Observations. *Journal of Climate*, Vol. 17, 1272-1282.
- Möller F. (1963): On the influence of changes in the CO₂ concentration in air on the radiation balance of the Earth's surface and on the climate. *Journal of Geophysical Research*, Vol. 68, Issue 13, 3877-3886.
- Moradi I., Buehler S. A., John V. O. and Elisasson S. (2010): Comparing upper tropospheric humidity data from microwave satellite instruments and tropical radiosondes. *Journal of Geophysical Research*, Vol. 115.
- Nigam S. and Chan S. C. (2008): On the Summertime Strengthening of the Northern Hemisphere Pacific Sea Level Pressure Anticyclone. *Journal of Climate*, Vol. 22, 1174-1192.
- Peixoto J. P. and Oort A. H. (1992): *Physics of Climate*. American Institute of Physics.
- Pierrehumbert R. T. (1995): Thermostats, Radiator Fins, and the Local Runaway Greenhouse. *Journal of the Atmospheric Sciences*, Vol. 52, No. 10, 1784-1806.
- Pierrehumbert R. T., Brogniez H. and Roca R. (2007): Chapter 6: On the Relative Humidity of the Atmosphere. in: T. Schneider, A. Sobel (Eds.), *The Global Circulation of the Atmosphere*, University Press: Princeton, NJ, USA.
- Pierrehumbert R. T. and Roca R. (1998): Evidence for control of Atlantic subtropical humidity by large scale advection. *Journal of Geophysical Research*, Vol.25, 4537-4540.
- Reick C. H., Raddatz T., Brovkin V. and Gayler V. (2013): Representation of natural and anthropogenic land cover change in MPI-ESM. *Journal of Advances in Modelling Earth Systems*, Vol. 5, 459-482.
- Rind D., Chiou E.-W., Chu W., Larsen J., Oltmans S., Lerner J, McCormick M. P. and McMaster L. (1991): Positive Water Vapor Feedback in Climate Models Confirmed by Satellite Data. *Nature* Vol. 349, 500-503.

- Roca R., Guzman R., Lemond J., Meijers J., Picon L. and Brogniez H. (2012): Tropical and extra-tropical influences on the distribution of free tropospheric humidity over the intertropical belt. *Surveys in Geophysics Journal* Vol. 33, 565-583.
- Rodwell M. J. and Hoskins B. J. (1996): Monsoons and the dynamics of deserts. *Quarterly Journal of the Royal Meteorological Society*, Vol. 122, 1385-1404.
- Rodwell M. J. and Hoskins B. J. (2001): Subtropical Anticyclones and Summer Monsoons. *Journal of Climate*, Vol. 14, 3192-3211.
- Saunders R. W., Hewison T. J., Stringer S. J. and Atkinson N. C. (1995): The Radiometric Characterization of AMSU-B. *IEEE Transactions on Microwave Theory and Techniques*, Vol. 43, 760-771.
- Saunders R. W., Matricardi M. and Geer A. (2010): RTTOV-9 Users guide. EU-METSAT Satellite Application Facility on Numerical Weather Prediction (NWP SAF), Doc ID : NWPSAF-MO-UD-016, Version 1.7.
- Scheff J. and Frierson M. W. (2012): Robust futures precipitation declines in CMIP5 largely reflect the poleward expansion of model subtropical dry zones. *Geophysical Research Letters*, Vol. 39, L18704.
- Schröder M., Roca R., Kniffka A. and Brogniez, H. (2014): Climatology of free-tropospheric humidity: extension into the SEVIRI era, evaluation and exemplary analysis. *Atmospheric Chemistry and Physics*, Vol. 14, 1112911148.
- Schulzweida U. (2014): CDO User's guide. Climate Data Operators, MPI for Meteorology, Version 1.6.3.
- Seager R., Murtugudde R., Naik N., Clement A., Gordon N. and Miller J. (2003): Air-Sea Interaction and the Seasonal Cycle of the Subtropical Anticyclones. *Journal of Climate*, Vol. 16, 1948-1966.
- Seidel D. J., Fu Q., Randel W. J. and Reichler T. J. (2008): Widening of the tropical belt in a changing climate. *Nature Geoscience*, Vol. 1.
- Shaffrey L. C., Hoskins B. J. and Lu R. (2002): The relationship between the North American summer monsoon, the Rocky Mountains and the North Pacific subtropical anticyclone in HadAM3. *Quarterly Journal of the Royal Meteorological Society*, 128, 2607-2622
- Sherwood S. C., Ingram W., Tsushima Y., Satoh M., Roberts M., Vidale P. L. and O'Gorman P. (2010): Relative humidity changes in a warmer climate. *Journal of Geophysical Research*, Vol. 115.

- Shi L., Bates J. and Cao C. (2008): Scene Radiance dependent intersatellite biases of HIRS longwave channels. *Journal of Atmospheric and Oceanic Technology*, Vol. 25, 2219-2229.
- Shi L. and Bates J. (2011): Three decades of intersatellite-calibrated High-Resolution Infrared Radiation Sounder upper tropospheric water vapor. *Journal of Geophysical Research*, Vol. 116, D04108.
- Smit H. G. J., Rohs S., Neis P., Boulanger D., Krmer M., Wahner A., and Petzold A. (2014): Technical Note: Reanalysis of upper troposphere humidity data from the MOZAIC programme for the period 1994 to 2009. *Atmospheric Chemistry and Physics*, Vol. 14, 13241-13255.
- Soden B. J. (2005): The Radiative Signature of Upper Tropospheric Moistening. *Science*, vol. 310, 841-844.
- Soden B. J. and Bretherton F. P. (1993): Upper tropospheric Relative Humidity From the GEOS 6.7 micro-m Channel: Method and Climatology for July 1987. *Journal of Geophysical Research*, Vol. 98, No. D9, 16.669-16.688.
- Soden B. J. and Bretherton F. P. (1996): Interpretation of TOVS water vapor radiances in terms of layer-average relative humidities: Method and climatology for the upper, middle, and lower troposphere. *Journal of Geophysical Research*, Vol. 101, 9333-9344.
- Soden B. J. and Fu R. (1995): A Satellite Analysis of Deep Convection, Upper-Tropospheric Humidity, and the Greenhouse Effect. *Journal of Climate*, Vol. 8, 2333-2351.
- Soden B. J. and Lanzante J. R. (1996): An Assessment of Satellite and Radiosonde Climatologies of Upper-Tropospheric Water Vapor. *Journal of Climate*, Vol. 9, 1235-1249.
- Spencer R. W. and Braswell D. (1997): How dry is the tropical free troposphere? Implication for global warming theory. *Bulletin of American Meteorological Society*, Vol. 78, No. 6, 1097-1105.
- Stevens B., Giorgetta M., Esch M., Mauritsen T., Crueger T., Rast S., Salzmann M., Schmidt H., Bader J., Block K., Brokopf R., Fast I., Kinne S., Kornbluh L., Lohmann U., Pincus R., Reichler T. and Roeckner E. (2013): The Atmospheric Component of the MPI-M Earth System Model: ECHAM6. *Journal of Advances in Modeling Earth Systems*, Vol. 5, 127.

- Su H., Jiang J. H., Zhai C., Shen T. J., Neelin J. D., Stephens G. L. and Yung Y. L. (2014): Weakening and strengthening structures in the Hadley Circulation change under global warming and implications for cloud response and climate sensitivity. *Journal of Geophysical Research: Atmospheres*, Vol. 119, 5787-5805.
- Sun D.-Z. and Held I. M. (1996): A Comparison of Modelled and Observed Relationships between Interannual Variations of Water Vapour and Temperature. *Journal of Climate*, Vol. 9, 665-675.
- Sun D.-Z. and Oort A. H. (1995): Humidity-Temperature Relationships in the Tropical Troposphere. *Journal of Climate*, Vol. 8, 1974-1987.
- Taylor M. A. and Alfaro E. J. (2005): Climate of Central America and the Caribbean. In: Oliver J.E., ed., *Encyclopaedia of World Climatology*, 183-89, Springer.
- Taylor K. E., Stouffer R. J. and Meehl G. A. (2012): An Overview of CMIP5 and the Experiment Design. *American Meteorological Society*, 485-498.
- Tilmes S., Pan L. L., Hoor P., Atlas E., Avery M. A., Campos T., Christensen L. E., Diskin G. S., Gao R.-S., Herman R. L., Hintsa E. J., Loewenstein M., Lopez J., Paige M. E., Pittman J. V., Podolske J. R., Proffitt M. R., Sachse G. W., Schiller C., Schlager H., Smith J., Spelten N. Webster C., Weinheimer A. and Zondlo M. A. (2010): An aircraftbased upper troposphere lower stratosphere O₃, CO, and H₂O climatology for the Northern Hemisphere. *Journal of Geophysical Research*, Vol. 115.
- Udelhofen P.M. and Hartmann D.L. (1995): Influence of tropical cloud systems on the relative humidity in the upper troposphere. *Journal of Geophysical Research* Vol. 100.
- Van Malderen R. and De Backer H, (2010): A drop in upper tropospheric humidity in autumn 2001, as derived from radiosonde measurements at Uccle, Belgium. *Journal of Geophysical Research*, Vol. 115.
- von Storch et al. (1999): *Das Klimasystem und seine Modellierung. Eine Einführung.* Springer Verlag.
- Vecchi G. A. and Soden B. J. (2007): Global Warming and the Weakening of the Tropical Circulation. *Journal of Climate*, Vol. 20, 4316-4340.
- Voldoire A., Sanchez-Gomez E., Salas y Méliá D., Cassou C., Sénési S., Valcke S., Beau I., Alias A., Chevalier M., Déqué M., Deshayes J., Douville H., Fernandez E., Madec G., Maisonnave E., Moine M.-P., Planton S., Saint-Martin D., Szopa

- S., Tyteca S., Alkama R., Belamari S., Braun A., Coquart L. and Chauvin F. The CNRM-CM5.1 global climate model: description and basic evaluation. *Climate Dynamics*, Springer.
- Wallace J. M. and Hobbs P. V. (2006): Atmospheric Science. An Introductory Survey. Academic Press, 2nd edition.
- World Climate Research Program (2011): CMIP5 Coupled Model Intercomparison Project. [http : //cmip – pcmdi.llnl.gov/cmip5/index.html](http://cmip-pcmdi.llnl.gov/cmip5/index.html), Last viewed on January, 12th 2017, at 13:30.
- World Meteorological Organization (2016): Observing Systems Capability Analysis and Review Tool (OSCAR). <https://www.wmo-sat.info/oscar/satellites/view/337>, Last viewed on November the 11th, 2013, at 16:20.
- Wu T., Song L., Li W., Wang Z., Zhang H., Xin X., Zhang Y., Zhang L., Li J., Wu F., Liu Y., Zhang F., Shi X., Chu M., Zhang J., Fang Y., Wang F., Lu Y., Liu X., Wei M., Liu Q., Zhou W., Dong M., Zhao Q., Ji J., Li L. and Zhou M. (2014): An Overview of BCC Climate System Model Development and Application for Climate Change Studies. *Journal of Meteorological Research*, Vol. 28(1), 34-56.
- Xin X., Wu T. and Zhang J. (2013): Introduction of CMIP5 experiments carried out with the climate system models of Beijing Climate Center. *Advanced Climate Change Research*, Vol. 4(1), 41-49.
- Zender C. (2017): NCO User Guide. A suite of netCDF operators. Edition 4.6.4-alpha03, for NCO Version 4.6.4-alpha03, Departments of Earth System Science and of Computer Science University of California, Irvine.

Copyright Notices

- Copyright for Figure 2.1: The source of this material is the COMET@Website at <http://meted.ucar.edu/> of the University Corporation for Atmospheric Research (UCAR), sponsored in part through cooperative agreement(s) with the National Oceanic and Atmospheric Administration (NOAA), U.S. Department of Commerce (DOC). ©1997-2016 University Corporation for Atmospheric Research. All Rights Reserved.
- Copyright for Figure 2.4: ©Copyright 1997 American Meteorological Society (AMS). Permission to use figures, tables, and brief excerpts from this work in scientific and educational works is hereby granted provided that the source is acknowledged. Any use of material in this work that is determined to be “fair use” under Section 107 of the U.S. Copyright Act September 2010 Page 2 or that satisfies the conditions specified in Section 108 of the U.S. Copyright Act (17 USC §108, as revised by P.L. 94-553) does not require the AMS’s permission. Republication, systematic reproduction, posting in electronic form, such as on a website or in a searchable database, or other uses of this material, except as exempted by the above statement, requires written permission or a license from the AMS. All AMS journals and monograph publications are registered with the Copyright Clearance Center (<http://www.copyright.com>). Questions about permission to use materials for which AMS holds the copyright can also be directed to the AMS Permissions Officer at permissions@ametsoc.org. Additional details are provided in the AMS Copyright Policy statement, available on the AMS website (<http://www.ametsoc.org/CopyrightInformation>).
Permission given per E-Mail, on January the 24th 2017, at 18:20.
- Figure 3.1 was used with the courtesy of Viju O. John, permission granted per E-Mail on November the 11th, 2016 at 11:44.
- Copyright for Figure 3.2: MSU/AMSU data and corresponding products are produced by Remote Sensing Systems. Data is available at www.remss.com/missions/amsu. Permission is granted to use images from this website in research and publications when accompanied by acknowledgement (E-Mail from Marty Brewer, November the 21th, 2016, 22:00).

Acknowledgements

First, I wish to thank my supervisors and advisors Prof. Dr. Stefan Bühler and Dr. Verena Grützun for this very interesting Masterthesis subject and their precious advice and inspirations. I am especially grateful for their understanding and flexibility, accepting the constraints I had by conciliating working on this thesis with my family life. I especially wish to thank Verena for the inspiring and enjoyable discussions, often early in the morning, and her heartening cheerfulness which helped in starting the working days.

My own technical skills would never have been sufficient to conduct this study with model data and the satellite simulation software. Therefore I am very grateful to have had the precious support of Oliver Lemke and Lukas Kluft, who more than once helped me to overcome apparently insurmountable technical obstacles in the twinkling of an eye. This is also the place to thank Elina, for her help with the model data and for always answering my questions related to tropical circulation, and Akio, for his helpful advice to get COSP started.

My special thanks goes to Nicole and Laura, with whom I shared not only the office, but also parts of the research subjects. Thank you for the helpful and cheerful discussions, thank you for your patience and encouragements, when I had my moments of doubts and desperation, and thank you for an excellent time together.

I want to thank my family, for allowing me to accomplish this master programme! Thank you Sebastian, for proofreading this thesis, for all the times you just listened to me and gave me precious ideas from an external point of view. I wouldn't have been able to study again without the valuable support of my parents and parents-in-law, who helped out many times by taking care of the children: many thanks!

Finally, I thank the World Climate Research Programme's Working Group on Coupled Modelling, which is responsible for CMIP, and the climate modeling groups (listed in Table Annex A of this paper) for producing and making available their model output. For CMIP the U.S. Department of Energy's Program for Climate Model Diagnosis and Intercomparison provides coordinating support and led development of software infrastructure in partnership with the Global Organization for Earth System Science Portals.

Eidesstattliche Erklärung

Hiermit versichere ich an Eides statt, dass ich die vorliegende Arbeit im Studiengang Master of Science Meteorologie selbstständig verfasst und keine anderen als die angegebenen Hilfsmittel, insbesondere keine im Quellenverzeichnis nicht benannten Internet-Quellen, benutzt habe. Alle Stellen, die wörtlich oder sinngemäß aus Veröffentlichungen entnommen wurden, sind als solche kenntlich gemacht. Ich versichere weiterhin, dass ich die Arbeit vorher nicht in einem anderen Prüfungsverfahren eingereicht habe und die eingereichte schriftliche Fassung der auf dem elektronischen Speichermedium entspricht.

Hamburg, den 31.01.2017

(Miriam Tivig)